Reduction of Friction in Polymeric Composites for Artificial Joint Prostheses

by

Jorge Francisco Arinez

B.A.Sc., Mechanical Engineering
University of Toronto, 1993

Submitted to the Department of Mechanical Engineering
in partial fulfillment of the requirements for the degree of

Master of Science in Mechanical Engineering

at the

MASSACHUSETTS INSTITUTE OF TECHNOLOGY

May 1995

Signature of Author .....
Department of Mechanical Engineering
May 1995

Certified by .....
Professor Nam P. Suh
Ralph E. and Eloise F. Cross Professor of Mechanical Engineering
Head of the Department
Thesis Supervisor

Accepted by .....
Professor Ain A. Sonin
Chairman, Committee on Graduate Studies

Reduction of Friction in Polymeric Composites for Artificial Joint Prostheses

by

Jorge Francisco Arinez

B.A.Sc., Mechanical Engineering

University of Toronto, 1993

Submitted to the Department of Mechanical Engineering
on May 1995, in partial fulfillment of the
requirements for the degree of
Master of Science in Mechanical Engineering

Abstract

Ultra-high molecular weight polyethylene has been used as a bearing material in artificial joints for more than thirty years. Despite this long period of use and the success which artificial implants have had, material failure and ultimately prosthetic failure still occurs as the result of mechanical wear of the bearing surface. Several wear mechanisms have been proposed as the main causes for failure; however, none is as dominant as the delamination wear of artificial knee prostheses. Delamination wear occurs mainly as the result of cyclic plastic deformation of the surface and subsurface layer which causes cracks to nucleate and propagate in the subsurface leading to the production of wear sheets. This research seeks a new alternative material to prevent the occurrence of delamination wear by the use of a fiber reinforced composite. The use of a fiber-reinforced composite having fibers oriented normal to the sliding direction is known to offer reduced plastic deformation resulting from the high stiffness of fibers and furthermore can inhibit crack nucleation and more importantly propagation since fibers are able to arrest the growth of cracks normal to the fiber axis. This new material has been called homocomposite based on the fact that fiber and matrix are made from the same material, namely UHMWPE. This material has shown promising results in friction tests yielding coefficients of 0.05 in bovine lubricated sliding conditions. The optimization of material processing parameters with respect to friction and wear of the homocomposite is also presented.

Thesis Supervisor: Professor Nam P. Suh
Title: Ralph E. and Eloise F. Cross Professor of Mechanical Engineering Head of the Department

Acknowledgments

No thesis could ever be successfully completed without the advice, support, encouragement of a wide variety of people.

The most important person who I would like to thank is Professor Suh. He was the one who gave me the opportunity to come to M.I.T. in the first place. His work ethic is truly a source of inspiration. A valuable lesson which Professor Suh has taught me is the need to confidently attack problems. I am also grateful to Professor Suh for his sage advice and wisdom during all of our meetings and for having him as a leadership role model.

I wish to thank Dr. Mohsen Mosleh whose company I have the honor to join as a tribologist. Working alongside him I have become a better researcher by experiencing his zeal and creativity for finding solutions to problems. I have learned a great deal working alongside him during this time and am truly grateful for all his help and guidance. I also would like to mention the help and wisdom of Dr. Saka. His depth of knowledge in many areas was a great asset for me, thank you.

I would also like to thank the faculty and staff of the Laboratory for Manufacturing and Productivity. Exposure to so many first rate industrial projects has been a great learning experience. I would like to specifically thank Fred Cote for his tireless patience in the machine shop. He never got bored whenever I approached him with any difficulty. I have become the machinist that I am thanks to his help. Kevin Baron and Gerry Wentworth are also to be commended for their machining wisdom and support.

To my collegaues in Professor Suh's two other groups, Dr. Toshimasa Ota, Joddhojit Sanyal, Ravi Patil, Chin Yee Ng, and Derrick Tate, it has been enjoyable discussing research. Also, I'd like to express my appreciation to all of the UROPs who I had the enjoyable experience of introducing to the world research.

A special note of thanks to Leslie Regan for making the administrative workings of M.I.T. and the Department a little more humane.

I wish to acknowledge and thank the M.I.T./B.W.H. Consortium for the Wear

of Polyethylene. They provided the support to carry out this work and just as importantly, the Consortium gave this work relevance because the need to improve the performance of artificial prostheses is a very real problem whose solution can mean a higher quality of life for many people. I'd like to thank Dr. Spector from whom I have learned a great deal about orthopedics during the course of my research in the Consortium.

All the friends that I have made in the LMP as well as at M.I.T, I thank you all for your encouragement. Special thanks to my housemates Mauricio Barahona and Robert Grotzfeld whom I could always count on for help and support.

I'd like to thank all my of friends back in Toronto who supported me in coming to Boston. Professor Benhabib at the University of Toronto who gave me his support especially at the beginning and all throughout my time here deserves special mention.

Finally, I thank my parents and brother and sister who always supported me, thank you.

Contents

List of Figures

List of Tables

Nomenclature

A_i	cross-sectional area of wear track
A_{ij}	extensional stiffness for a laminate
B_{ij}	coupling stiffness
b	half contact width for cylinder on flat
D_{ij}	bending stiffness for a laminate
d_i	initial fiber diameter
E	Young's modulus
E'	reduced stiffness
F	force
F_f	force of friction
G_M	torsion modulus of matrix
K_a	change in interatomic distance, force parameter
K_θ	change in interatomic angular separation, force parameter
$L_{weartrack}$	overall length of wear track
l_o	interatomic distance in organic molecule
M	bending moment
$\overline{M_w}$	average molecular weight
N	normal load
P	normal load
p_o	loading normal to sliding direction
q_o	loading tangential to sliding direction
R'	reduced radius
R_a	average surface roughness
$2r$	diameter of wear particle
r_f	fiber radius
T_{bath}	temperature of fiber drawing water bath
T_d	draw temperature
T_{mold}	compression mold cavity temperature

U_m	strain energy in matrix
u_x, u_z	displacements
ΔV	wear volume
V_f	fiber volume fraction
V_m	matrix volume fraction
w	width of wear particle
α	internal damping energy loss fraction
γ_{xz}	shear strain
Δ	equivalent radius and stiffness
δ	deformation
ϵ_x, ϵ_z	normal strains
θ	surface roughness in Friction Space concept
	interatomic angular separation
θ_d	angular deformation of a single fiber
λ	draw ratio
μ	coefficient of friction
μ_a	friction due to adhesion
μ_d	friction due to asperity deformation
μ_f	coefficient of friction of fibers
μ_m	coefficient of friction of matrix
μ_p	friction due to plowing
ν	Poisson's ratio
ρ	density
$\sigma_{1,2}$	principal normal stresses
σ_x, σ_z	normal stresses
τ_1	principal shear stress
τ_{max}	maximum shear stress due to Hertzian contact
τ_{xz}	shear stress
ϕ	stress function

Chapter 1

Introduction

1.1 Tribology

The importance of tribology to mankind cannot be emphasized enough. Since early civilizations, the unavoidable fact of life has always existed that people and objects must move, and when they do, they undoubtedly move at less than full efficiency. In the majority of cases this inefficient movement can be traced back to friction and wear. Indeed, some estimates have stated that as much as one third of the world's energy resources in present use is needed to overcome friction.

Tribology is the study of friction, wear and lubrication of surfaces in relative motion. Wear is often the object of most study because it causes many undesirable effects. In general, wear due to sliding or rolling is the net loss of material in a component. This loss of material causes many events to occur. If material is removed from a sliding interface, subsurface material becomes exposed to the environment and consequently the surface is open to chemical attack by the operating environment. Furthermore, once a surface develops defects arising from the wear process, the process is self perpetuating; wear leads to more wear. Wear in different sliding systems causes different consequences. In engineering systems for example, wear leads to the loss of tolerance of the system components. In biomedical applications such as wear in artificial joints, wear produces particles which cause adverse biological effects. The human body with all of its moving parts is a place where much wear can take place.

In such a biological system, wear is also not desirable. Before the advent of modern medicine, people whose 'moving parts' wore out were forced to live in pain because at the time no solution existed to their personal 'wear problem'. The key moving parts in the human body where wear can have painful and even devastating effects are in all the joints. With this in mind, the tribological system which will be the focus of this thesis is the human articulating joint.

1.2 Artificial Joint Prostheses

The natural human articulating joint is a miracle of bearing design. It is capable of withstanding high loads as well as large impact loads. It accomplishes this while yielding a coefficient of friction in the range of 0.005 to 0.025. However, it is a very complex biomechanical system whose function is still not completely understood by both the medical and engineering community alike. Even without such a complete understanding, total joint replacement is one of the most important advances which has been made in the history of orthopedic surgery. This is a very beneficial form of surgery because not only is pain almost completely eliminated but in addition a significant amount of function is restored. Worldwide estimates are that half a million joint prostheses are implanted in humans each year. Figure 1-1 shows the components of an artificial knee prosthesis. However, despite the success enjoyed by artificial joint implants in society today, there are still failures which occur and must be solved.

The more critical joints in the human body are the ones that bear the weight of the person namely the hip and knee joints. There are different reasons which may lead to a person suffering pain in these joints. The most common reason is caused by degenerative disease (osteoarthritis). For people with this disease, joint arthroplasty is not performed until a person reaches a stage where pain becomes intolerable and prevents normal daily activities such as walking. Once a person receives an artificial joint they can normally expect it to be free of problems. However, failure can and does occur.

Artificial joints can fail for a number of reasons. The goodness of fit between

metallic components inserted into bone often affects whether loosening of the implant will occur. In many cases, this loosening of the bone/implant interface is the chief cause of long term failure[1]. However, more importantly loosening is caused by wear.

The effect of wear is twofold. First, dimensional changes in the components as a result of wear leads to improper mating of surfaces which in turns leads to non-uniform load distribution throughout the implant during its operating life. Secondly, perhaps more importantly is the generation of large wear particles through the process of delamination wear. In addition to these large particles is the generation of small micron to submicron wear by "plowing". These wear particles illicit a human biological response. This biological response more commonly referred to as osteolysis can have several negative effects. These include local tissue inflammation and bone resorption which can eventually lead to fracture of the bone which supports the metallic stem in the case of the hip and knee joint.

1.3 Problem Definition

Given the above background into artificial joint prostheses, the problem which this thesis sets out to solve is therefore the wear problem - specifically the delamination wear problem, which can lead to the eventual failure of the artificial joint. A clear understanding of the mechanics of the sliding interface is critical to the solution of any tribological problem. The approach then taken, is to understand and identify the factors leading to delamination wear and then based on this knowledge, develop and test a material capable of eliminating or minimizing the destructive effects of this form of wear. The solution of this problem is subject to the constraints imposed by the function of biomaterials in the human body. A potential material must be biocompatible meaning it must be non-toxic and must possess the necessary mechanical properties to meet the daily demands of the human subject. Also, the biomaterial must be able to withstand and endure over a long period of time (greater than ten

[1]Incompatibility in stiffness between the bone and implant otherwise known as stress shielding is known to cause bone remodeling and potentially bone fracture.

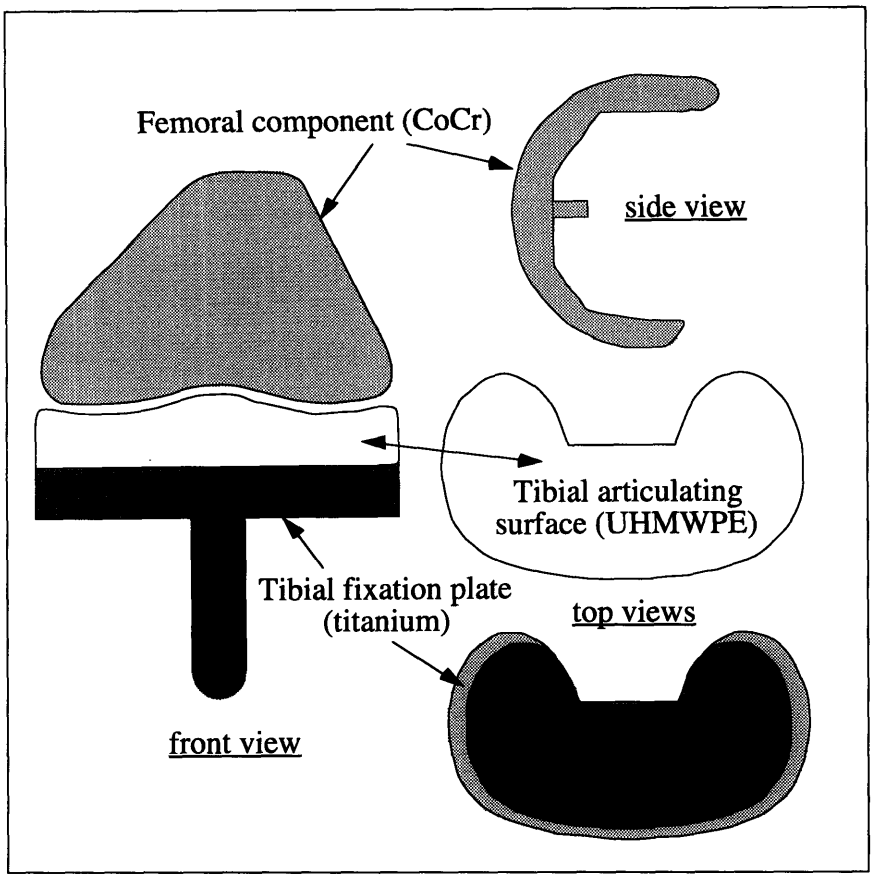

Figure 1-1: Artificial knee prosthesis

years) the corrosive effects of body fluids while fulfilling the mechanical function of the load bearing joint without mechanical failure.

1.4 Overview of Thesis

This thesis details the development of an alternative bearing material for artificial joints with potential implications in other bearing applications. Chapter 2 covers Delamination Wear theory and the role which it plays in the wear of UHMWPE. Also covered is the idea of using fiber-reinforced polymeric composites to prevent crack nucleation and propagation leading to delamination failure. First, attempts to develop this material are based on work by Suh [75] who had previously developed a fiber reinforced ultra-tough high density polyethylene. Preliminary friction and wear data pointed to potential benefits by using a UHMWPE fibers along with an

UHMWPE matrix. This led to the development of the 'homocomposite'. Its processing and fabrication methods are detailed in the third chapter. The development of the homocomposite was immediately followed by friction and wear testing and further structural characterization using techniques such as scanning electron microscopy and differential scanning calorimetry. These results are detailed in the fourth chapter. In the fifth chapter, to help explain friction and wear results, the mechanical behavior of the bearing material is studied with respect to the applied loading and the resulting contact stresses. In addition, a model based on classical lamination theory is presented for homocomposites consisting textile laminates. In the closing chapter, conclusions along with recommendations for future research are given.

Chapter 2

Reduction of Friction and Wear in Artificial Prostheses

2.1 Introduction

This chapter deals with the wear problem existing today in artificial articulating components, and then based on an understanding of delamination wear theory proposes the means to reduce the effects of this problem. It is known that the contact stresses in artificial knee prostheses are much greater than those existing in artificial hip prostheses. As a result, the failure modes of wear in each case tend to be different. Abrasive wear tends to occur in the hip leading to the production of micron and submicron-sized wear particles. On the other hand, though abrasive wear occurs in artificial knees as well, the wear mechanism which dominates and which can lead to catastrophic failure is delamination wear.

Retrieval studies of knee prostheses conducted by Landy and Walker [40] found that delamination initiated by intergranular defects led to complete breakup of the material into flakes and particles. Furthermore, this study found that delamination wear can produce wear debris several millimeters in diameter having a thickness of 1-2 mm. Clearly to increase the life of an artificial joint, the goal is to reduce and ultimately prevent the factors which lead up to delamination wear.

First, the background on the Friction Space Concept [74] will be reviewed as it

pertains to the friction mechanisms responsible for delamination wear. The events leading up to and causing the generation of delaminated wear sheets will be reviewed. The role of plastic deformation of the subsurface and the critical importance which this plays leading to the onset of delamination wear will be described. The introduction of fiber-reinforced composites will be presented as the means to prevent the crack propagation occurring during delamination wear.

2.2 Friction Space Concept

The Friction Space Concept [74] is presented here to give background into the two important components of friction that participate in the delamination wear process, namely friction due to asperity deformation and friction due to plowing by hard asperities or by wear particles. Three fundamental aspects which govern tribology [74]: environmental effects on surface characteristics through physiochemical interactions, force generation and transmission between surfaces in contact, and material behavior near the surface in response to external forces at the contact points of the surface. Figure 2-1 shows the contribution of these three main mechanisms of friction: μ_a friction due to adhesion, μ_d friction due to asperity deformation, and μ_p friction due to plowing.

μ_a Friction due to adhesion: The adhesion component of friction occurs due to the asperities which come in contact with asperities on the opposite surface forming welded junctions and must be sheared to permit sliding. μ_a is not significant early in sliding due to the existence of surface contaminants. In cases were surface contamination is high (as with human body fluids) the role of μ_a may not be significant.

μ_d Friction due to asperity deformation: This friction mechanism plays an early role in the wear process since at the onset of sliding, asperities are deformed and then removed; once deformation has occurred this mechanism is no longer significant. However, if wear is occurring at a high rate and new surfaces with new undeformed asperities are being exposed the μ_d will contribute to the steady state friction coefficient. In general, the relative contribution of μ_d is small.

μ_p **Friction due to plowing:** This is due to one of two possibilities: the friction force is generated by the penetration of hard asperities or by the penetration of wear particles. In the wear of cobalt chrome articulating on UHMWPE the former is the larger contributor to friction.

With these components now defined, we turn to Figure 2-1 depicting friction as a function of the three above mechanisms μ_a, μ_d, and μ_p. In the friction space concept μ_a is given by the axis labelled f, the interfacial shear strength, μ_p is given by the axis labelled $w/2r$ (ratio of width of wear particle generation to the diameter of the particle). The third component discussed, μ_d is given by the friction surface θ. When $\theta = 0$ this corresponds to values of friction μ for a surface with no asperities. θ_i represents the case of initial roughness prior to sliding, and θ^* is for the steady state case. It is important to note that θ^* also represents the roughness of delaminated surfaces. The importance of the Friction Space Concept is that it depicts the effect of increasing surface roughness due to for example the onset of the delamination wear process. A typical sliding event begins with a μ_i for a given surface roughness θ_i and increases along a path that follows the dark heavy line in Figure 2-1 until θ^* for which $\mu = \mu_{ss}$.

Having established the fundamental friction processes at work between the surfaces of interacting materials, we can deduce that for articulating joints the dominant component will be plowing. This reasoning is based on the fact that the counterface is much harder than the bearing surface and therefore counterface asperities will be responsible for the bulk of surface damage. Thus, in the friction space the curve will be projected onto the μ and $w/2r$ plane since adhesion does not play an appreciable role.

2.3 Delamination Wear

As was stated in the introduction to this chapter, the delamination wear process has been found to occur in artificial knee prostheses. The Delamination Theory of Wear was first proposed by Suh [73] to explain the wear of metals. However, the series of

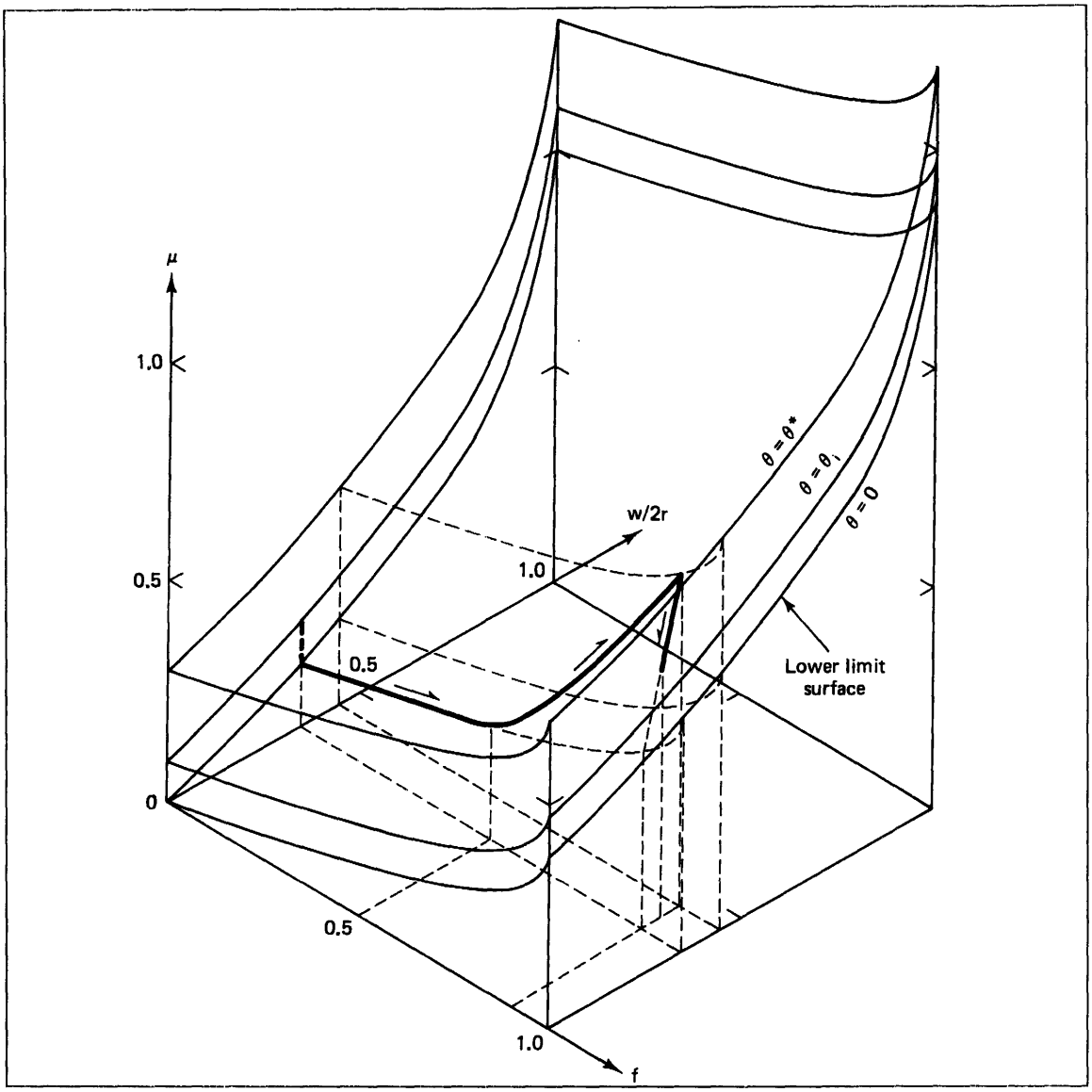

Figure 2-1: Concept of Friction Space [74]

events leading to the production of delaminated sheets of UHMWPE can be explained based on this theory of wear. The sequence of events leading to formation of a wear sheet has been adapted from the delamination wear process for metals [74] and will be explained in terms of a hard slider (cobalt chrome) sliding against a softer material (UHMWPE):

1. The surfaces of these two materials come into contact and initially asperities on the softer UHMWPE are easily deformed and fractured by the hard asperities of the cobalt chrome (recall μ_d from friction space concept). This leads to the generation of a smoother surface on the UHMWPE (assuming the counterface is smoother than the UHMWPE; this is usually the case since high surface finishes are attainable more for the metal than for the UHMWPE)

2. The hard asperities on the CoCr slider exert a surface traction thus inducing incremental plastic deformation per cycle of loading. This effect is cumulative as it fatigues the surface layer of the UHMWPE.

3. As sliding progresses deformation of the UHMWPE subsurface continues. Note that as a result of the hydrostatic state of stress directly beneath the contact region cracks cannot nucleate very near the surface until the slider has passed by.

4. Cracks may exist as a result of two conditions. There may be pre-existing voids and defects in the material. With UHMWPE, the presence of fusion defects (intergranular defects) have been known to be crack nucleation sites. Alternatively, repeated loading and deformation cycles can cause cracks to nucleate in the subsurface. Once cracks exist, they extend, propagate and eventually join nearby cracks.

5. Eventually enough cracks join together and shear to the surface allowing for a long thin wear sheet to delaminate. This exposes a fresh, rough surface and the process begins once again with Step 1.

Once this process has begun, there is nothing which can be done to halt the destructive wear which takes place. The development of a potential wear resistant material must address this issue. The hypothesis for stopping or minimizing this effect with the use of a composite material is discussed in the next section.

2.4 Polymeric Fiber-Reinforced Composites

According to the delamination wear theory, the growth of cracks parallel to the sliding surface occurs at a depth favorable for crack propagation. Given this fact, the development of an alternative bearing material must prevent or at least significantly reduce such crack propagation. This hypothesis had led to the development of fibre-reinforced UHMWPE. The use of fibre reinforcement in the field of composites has long been established as a means to tailor the mechanical properties of a material. The same principle may be applied to reinforcing a material with fibers for tribological applications, Suh [76]. In Figure 2-2 a fiber is shown perpendicular to a crack propagating in the subsurface illustrating how a fiber can effectively block the path of a crack and in so doing reduce one of the main causes of delamination wear.

2.5 Effect of fiber orientation on friction and wear

Suh [76] showed that in tests with Kevlar fiber-epoxy composites the lowest wear was obtained with a normal fiber orientation; however, it was also observed that in this case the friction coefficient was the highest relative to the other two possible orientations. Suh [76] attributed this lack of correlation to the competing effects of friction being controlled by surface properties and wear being controlled by bulk mechanical properties. Polytetrafluoroethylene (PTFE) is a good example of a material which exhibits contradictory behavior.

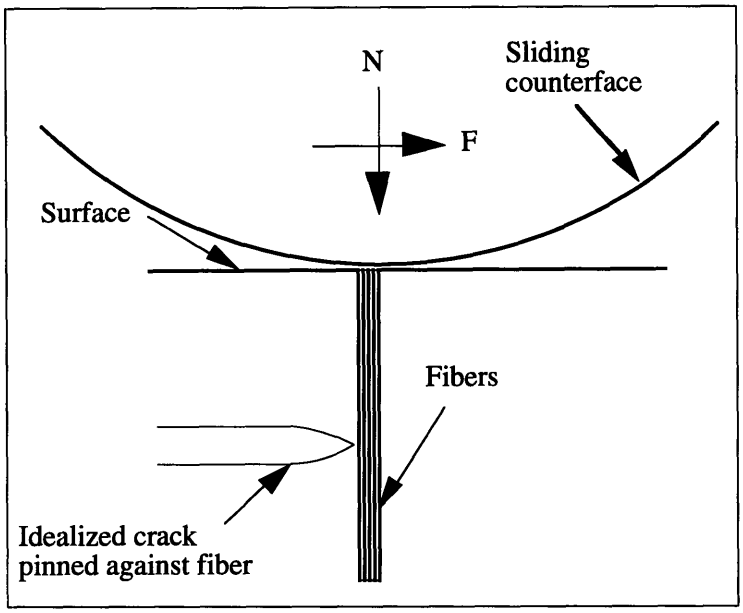

Figure 2-2: Use of fibre reinforcement to impede crack growth

PTFE yields low friction; however, it has a very high wear coefficient. The low coefficient of friction can be attributed to its surface properties. PTFE has a surface layer which is easily sheared, this layer behaves similar to a solid lubricant in that it has a very low shear strength. Unfortunately, this low shear strength of the surface is also present in the bulk causing wear to occur at a high rate despite a low friction coefficient.

For composites with brittle fibers and a brittle matrix (i.e., graphite fibers and epoxy resin matrix), debonding of fibers from the matrix can occur when cracks nucleate at the fiber-matrix interface. To understand the nucleation of cracks at the fiber-matrix interface, the state of stress under sliding conditions must be known. Knowledge of the mechanical behavior of the sliding interface is required to understand the wear behavior of composites as it is affected by fiber-matrix interactions.

Under a sliding asperity contact which exerts both a normal and tangential load on the surface of a material, specific stress fields are developed in the immediate region below the surface. Directly underneath the slider the material is in a state of hydrostatic compressive stress. As the slider moves, the

region of hydrostatic stress follows the slider and always remains underneath it. As a consequence of the movement of the slider, areas which were once under compressive stresses become loaded in tension. In particular, there is a region directly behind the contact location where the tensile stress parallel to the surface is at a maximum at the surface. This tensile stress decreases both as the distance down into the material and the distance horizontally away from the slider increases. From the knowledge of these resulting stress fields, the location of potential fiber-matrix debonding sites can be anticipated. Since the horizontal tensile stress is greatest at the surface (in locations not directly underneath the moving slider), it would be expected that fiber-matrix debonding would occur at the surface as cracks nucleate here and propagate down into the bulk along the fibers (for composites with normal orientations) if the applied stress at the fiber/matrix interface exceeds the bond strength. The debonding will occur only down to a finite distance because the tensile stresses decreases with increasing depth.

For cases of longitudinal or transverse orientations, crack nucleation may take place at a specific depth where the tensile stress component is maximum (the component perpendicular to the sliding direction) or at the surface, right at the fiber-matrix interface. For all three fiber-sliding direction orientations, once cracks are nucleated the wear rate will increase as cracks propagate along the fiber-matrix interface and through the matrix itself.

Chapter 3

Development of Homocomposites

3.1 Introduction

This chapter introduces the development of homocomposites. The development of the homocomposite began with work on the manufacture of Ultra-Tough Polyethylene developed by Suh [75, 2]. This ultra-tough polyethylene when it was originally developed was never friction tested as a potentially wear resistant material. This missing piece of experimental work became the starting point for the development of homocomposites. Production of ultra-tough high density polyethylene (UTHDPE) enabled wear testing to be carried out for the first time and provided data to begin development of the homocomposite.

Early data demonstrated the feasibility of using high strength HDPE fibers to increase the wear resistance of HDPE. However, since the performance of UTHDPE was limited by the performance of the properties of HDPE, a new material, preferably a polyolefin was required which could yield improved friction and wear. This led to investigation of the possibility of UHMWPE as the basis for a new wear resistant material since UHMWPE is known for its superior

friction and wear properties compared to HDPE. This in turn led to the combination of ultra-drawn UHMWPE fibers Spectra with UHMWPE resin yielding the first homocomposite. However, the concept of reinforcing the polyethylene with high strength fibers remained unchanged. This chapter traces this development and provides details of its manufacture.

3.2 Polyethylene

One of the most common industrially produced polymer, polyethylene was first produced on a commercial scale in 1939. Some of its features which have made it so popular in industry are its relatively low cost, good electrical insulative properties, good chemical resistance, ease of processing, toughness, flexibility, and transparency. As will be discussed in Section 3.3.2 the high strength which can be obtained from polyethylene molecules can be traced to the very strong covalent carbon-carbon bonds which are the backbone of the molecular chains in the -$(CH_2)_n$- structure of polyethylene.

Polyethylene is a long chain aliphatic hydrocarbon and as such has no strong intermolecular forces. It also has a low cohesive energy density and is non-polar. However, the overall bulk strength of polyethylene is limited by the weaker Van der Waals forces caused by hydrogen bonding between the molecular chains. The ability of polyethylene to resist deformation and fracture is a function of the relative configuration of the individual molecular chains. Polyethylene begins to soften at temperatures of about 110°C and as the temperature increases becomes molten (eg., 137°C for HDPE) and is therefore considered a thermoplastic.

Molecular weight is another property which strongly determines how melt-processable polyethylene is. For example, HDPE with a melt-index of 2.8 dg/min (ASTM D-1238) and with an average molecular weight of 50,000 can be injection molded. However, UHMWPE with an intrinsic viscosity of 27.0 (ASTM D-4020) and with an average molecular weight of 3,000,000 cannot be

extruded in a conventional-type screw extruder. Conversely, at low temperatures, polyethylene chains assume a higher degree of order and closer packing and can be considered partially crystalline. The bulk polyethylene is in fact considered polycrystalline.

3.3 Ultra-Drawn Polyethylene

3.3.1 Introduction

The early basis for homocomposites began with adaptation of earlier work done by Suh and Alei [75, 2] to improve the mechanical properties of polymers by molecular orientation. Suh and Alei [75, 2] showed the benefits that could be obtained by using highly oriented fibers. However, the intention here is to produce a polyethylene-based material with not only improved mechanical properties, but also improved wear properties. Many different methods can be used to achieve molecular orientation in polymers. Some of these include solid state drawing, solid state extrusion, push-pull extrusion, biaxial stretching, and more recently with ultra-high molecular weight polyethylene, solution gel-spinning.

In general, the mechanics of solid state drawing of fibers involves the following components. As with ductile metals, polymers exhibit similar necking and drawing phenomena that can be observed in tensile experiments. In addition, due to the ease by which molecular chains can move in polymers, polymers are capable of undergoing large strains in comparison to metals. Andrews and Ward [3] demonstrated that the Young's modulus is to a good approximation, dependent only on the draw ratio. This is shown in Figure 3-1. It has been shown [18] that the solid state drawing of polymers is affected mainly by average molecular weight $\overline{M_w}$, and most importantly the drawing conditions, specifically the strain rate and the temperature. The strain rate in a spool driven drawing

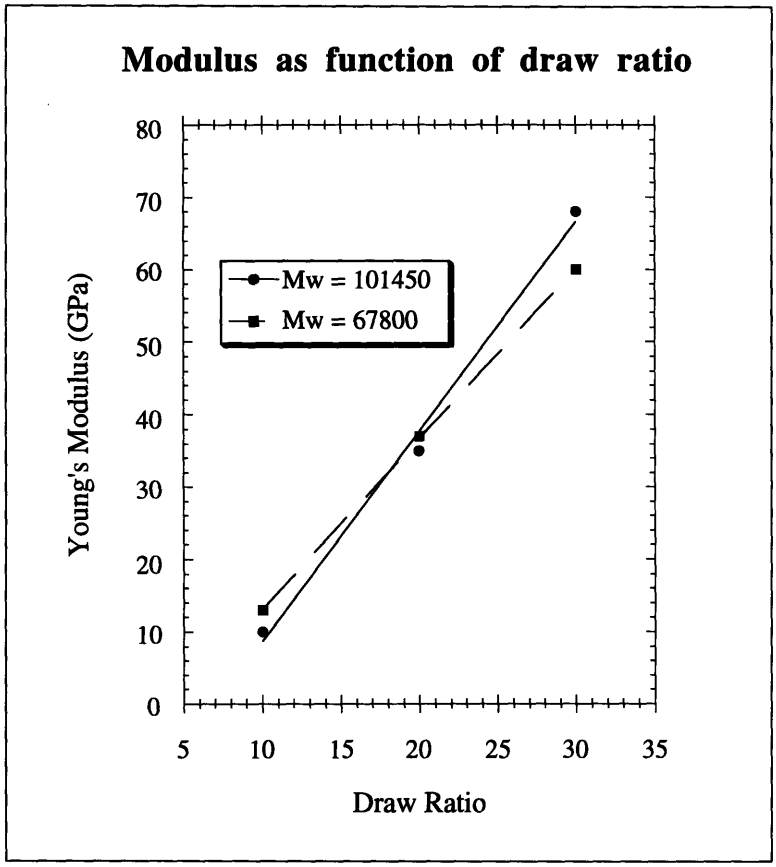

Figure 3-1: Modulus as function of draw ratio [3]

system is governed by motor rotational speeds. The temperature is regulated by controlling the temperature of the ambient medium where the drawing takes place. The temperature plays an important role in the magnitude of the draw ratio achieved. Capaccio and Ward [18] have examined this effect in detail. They found that the maximum draw ratio attainable increased monotonically with draw temperature T_d until the specimen failed as the melting point was approached. Figure 3-2 shows experimental results of measuring draw ratio and modulus as a function of draw temperature T_d.

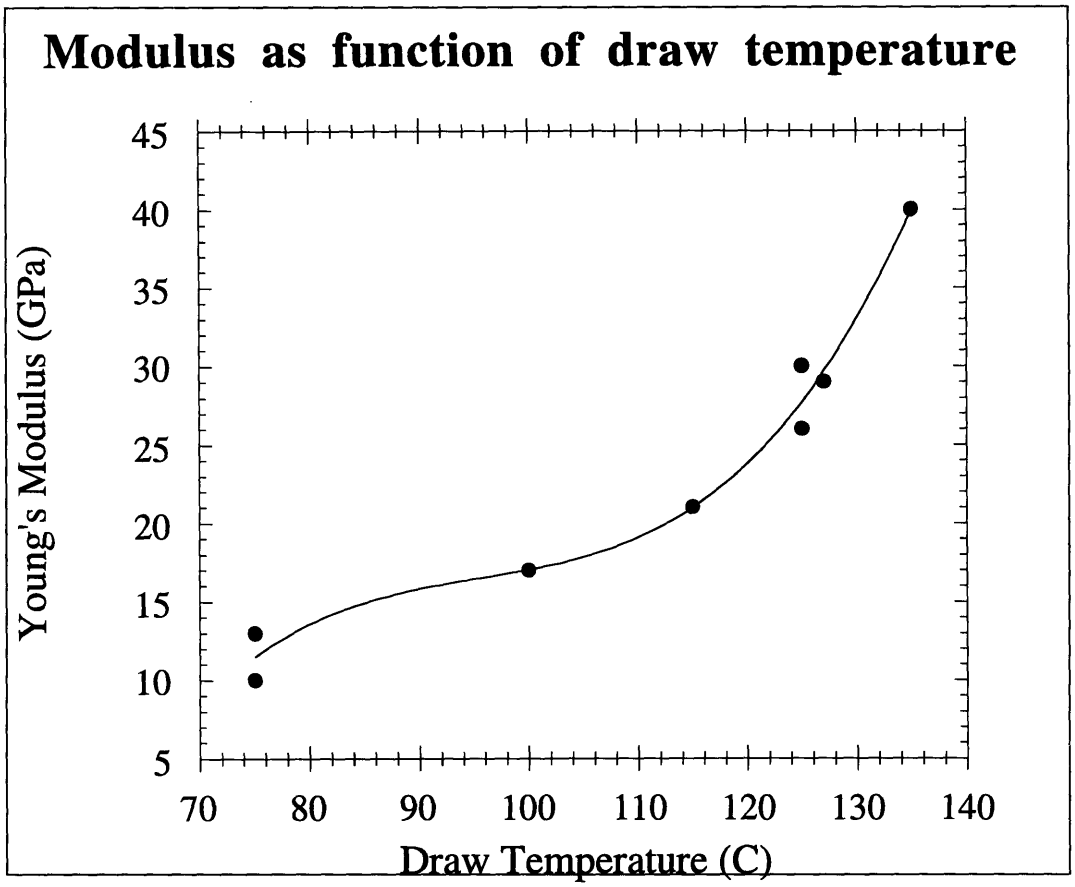

Figure 3-2: Draw ratio as a function draw temperature [18]

3.3.2 Theoretical Ultimate Young's Modulus for organic fibers

It is important to consider how strong a fiber can be made from polyethylene. Bunsell [16] derives and calculates the theoretical maximum Young's Modulus for an organic polymer such as polyethylene. The assumption that is made is that the tensile force is applied exactly in the direction of alignment for a molecule with a C-C backbone. Figure 3-3 shows just such a molecular idealization. A force F is applied in the direction shown causing the valence angles C_1-C_2 and C_2-C_3 to increase. Bunsell derives two parameters K_a, and K_θ based on the applied force F and the deformation which results because the valence angles are increased:

$$K_a = \frac{F}{\Delta a}\sin(\theta/2) \quad and \quad K_\theta = \frac{Fh}{\Delta\theta} \tag{3.1}$$

Direct measurements with Raman or infrared spectrotrometry show that for an olefine molecule:

$$K_a \simeq 460\,N/m \quad and \quad K_\theta \simeq 82 \times 10^{-20}\,Nm \tag{3.2}$$

Using geometry, the length l_o is:

$$l_o = 2a\sin(\theta/2) \tag{3.3}$$

the applied force F causes a differential change in length:

$$dl = 2(\frac{a}{2}\cos(\theta/2)d\theta + \sin(\theta/2)da) \tag{3.4}$$

Dividing equation 3.4 by equation 3.3 yields the strain:

$$\frac{dl}{l_o} = \frac{\frac{a}{2}\cos(\theta/2)d\theta + \sin(\theta/2)da}{a\sin(\theta/2)} \tag{3.5}$$

The moment Fh causes a $d\theta$, and combining with 3.3:

$$\frac{d\theta}{F} = \frac{\frac{a}{2}\cos(\theta/2)}{K_\theta} \tag{3.6}$$

similarly:

$$\frac{da}{F} = \frac{\sin(\theta/2)}{2K_a} \tag{3.7}$$

Combining equations 3.4, 3.5, 3.6, and 3.7

$$\frac{dl}{F} = \frac{a^2(\cos(\theta/2))^2}{2K_\theta} + \frac{(\sin(\theta/2))^2}{K_a} \tag{3.8}$$

$$E = \frac{F}{A}\frac{l_o}{dl} \tag{3.9}$$

Using Equation 3.3 and inverting Equation 3.8 and using experimentally available constants: $A = 18\text{x}10^{-20}\ m^2$, $a = 1.53\text{x}10^{-10}\ m$, and $\theta = 112^o$, the theoretical value of the Young's modulus for polyethylene is $E = 236.6\ GPa$.

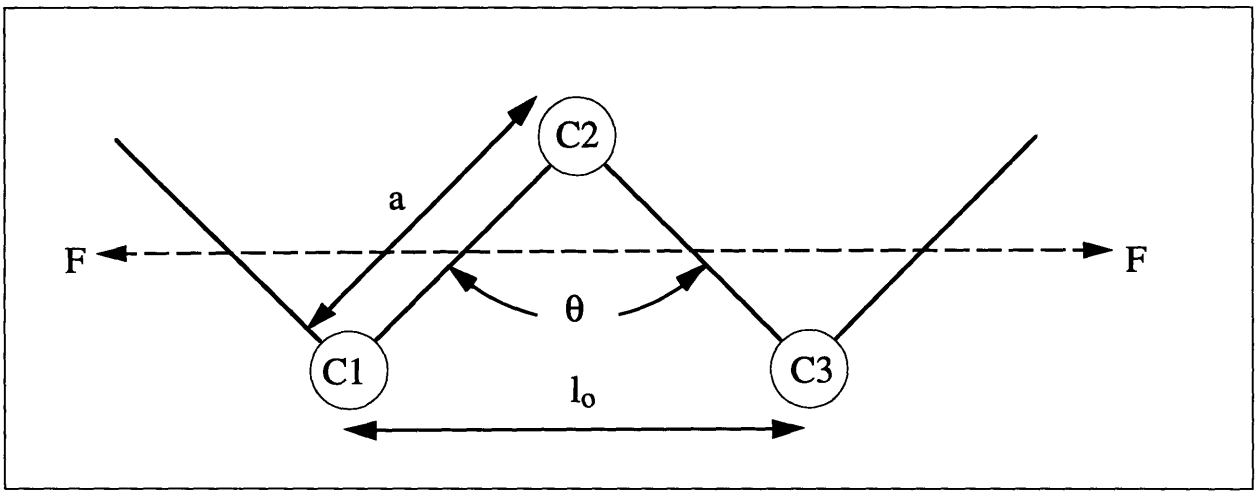

Figure 3-3: Organic macromolecule with carbon backbone [16]

3.3.3 Ultra-Tough High Density Polyethylene

The invention of ultra-tough high density polyethylene by Suh and Alei [75, 2] is based upon taking advantage of the improved mechanical strength which high molecular orientation imparts to the bulk structure of polymers. Tensile tests performed on HDPE Alathon 7030 which had been stretched to a draw ratio of $\lambda = 8.2$ show a dramatic improvement in strength by a factor of 10 as well as toughness as shown in Figure 3-4.

However, since this orientation has only involved a physical reorganization of molecular chains, heat processing of the oriented fibers will immediately eradicate all gains made in strength and toughness. In the background given on polyethylene in Section 3.2, polyethylene was described as having primary bonds at the carbon backbone of its molecular chains and with only weaker secondary Van der Waals forces linking neighboring chains together. Clearly a stronger link is required to retain the highly oriented state of the polyethylene molecular chains once the desired draw ratio has been achieved. In other words, permanent crosslinks are needed between these molecular chains.

Suh and Alei [75, 2] found that by exposing oriented polyethylene fibers to electron beam radiation, crosslinking could be promoted and hence retain the stronger polyethylene structure for later melt processing. Electron beam irradiation provides energy to break the C-H bonds thereby permitting carbon atoms on neighboring chains to form primary covalent bonds with one another. The application of this method to produce solid samples from drawn polyethylene fibers is discussed in the next section.

3.3.4 Processing of Ultra-Tough HDPE

The following process was used to produce ultra-tough high density polyethylene following the work by Suh and Alei [75, 2] in order to manufacture samples for wear testing. First, Alathon 7030 HDPE pellets were extruded using a

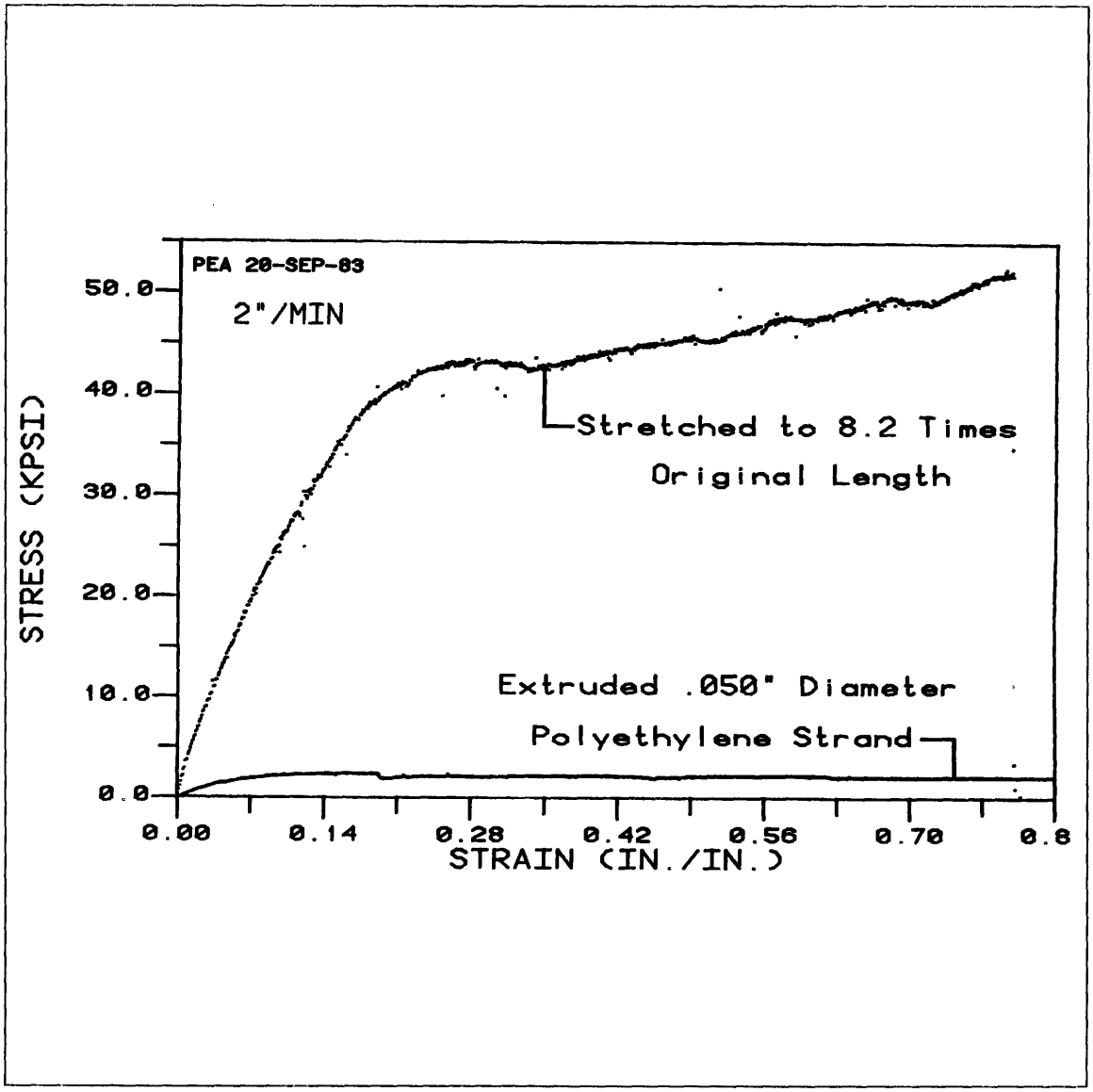

Figure 3-4: Strength of drawn Alathon 7030 HDPE [2]

small benchtop laboratory extruder through a conical die to produce fibers having an initial diameter prior to drawing of approximately $d_i = 350\,\mu m$. The rotational velocity of the motor with the takeup spool had to be varied continuously to ensure minimal variation in the fiber diameter as the linear fiber velocity increased. This task was performed manually and introduced some variation in the diameter of the final drawn fiber.

Once enough fiber had been collected on the spool, the next step was to orient the fibers to increase the strength of the fibers. To perform this orientation, a special bath was constructed and is schematically shown in Figure 3-5. The bath is watertight and a 750 W immersion heater with a PID controller maintains the water at a constant temperature of $T_{bath} = 50°C$. A spool containing the fiber produced in the extrusion step is mounted on bearing blocks in the container with the shaft belt driven by Motor A. Similarly, a take up spool is also supported on bearings and is connected by a drive belt to Motor B. A difference in the speed of the two motors causes the fiber to neck at the point indicated in the figure. Once the speed of Motor A has been set, the operator need only vary the speed of Motor B to ensure a constant linear speed as oriented fiber accumulates on the takeup spool. The speed of the motors was approximately 50 rpm for motor A and 5 rpm for motor B.

Varying the speed of Motor B also has the effect of moving the fiber necking point to the left or right as shown in Figure 3-5 (forward and back). If the fiber necking point is not kept relatively stationary in space, the likelihood of fiber fracture increases. Fracture of the fiber decreases the production rate because the take-up spool and the feed spool must be restarted in unison.

Once a full spool of oriented fiber has been collected, it must be unwound onto a flat plate for irradiation. The oriented fibers on a flat plate are then exposed to electron beam irradiation as shown in Figure 3-6. Different samples of oriented HDPE received different dosages ranging from 2.5 MRad to 30 MRad. The implications of irradiation in addition to the function of crosslinking are

discussed in Section 3.5.3.

Once the plates of oriented fibers have received the required dosage of radiation, the test sample must be produced. Samples were produced using compression molding. This six-step process is shown in Figure 3-7. First, fibers are cut to the length of the cavity of the mold (approx. 3") and filled inside the cavity[1]. The mold is then assembled and taken to a hydraulic press. The press used was a 30 ton Wabash hydraulic press with temperature controlled upper and lower heating platens. The mold is pressurized (to 1500 psi, 10.34 MPa) and heat applied for approximately 60 minutes until the desired steady state temperature of the mold is reached. After 15 minutes at steady state to ensure full diffusion, the platens and mold walls are rapidly cooled with water. However, during this cooling process, pressure is continually maintained. This is done to maintain molecular orientation of the fibers, as the mold cools and the sample solidifies. Once the temperature drops below 30°C, the pressure is released and the sample removed from the mold.

3.3.5 UTHDPE Wear Results

The compression molding process which was described above permits the production of specimens for wear testing. Friction and wear testing will be discussed in much greater detail in Section 4.3. The wear data shown in Figure 3-8 is of tests conducted on samples of HDPE, ultra-tough HDPE, and UHMWPE. The sample size used to determine the standard deviation was three. The sliding counterfaces were made from SS304 and the lubricant was saline solution. The sliding duration of the test was 4260 m with a load of 760 N.

The column on the far left of the HDPE is the wear test result of samples which had been produced simply by compression molding of virgin Alathon 7030 HDPE pellets. Clearly, these samples exhibited much higher wear than

[1]The compression mold used was made from steel and had a rectangular cavity 2" x 3" x 1"

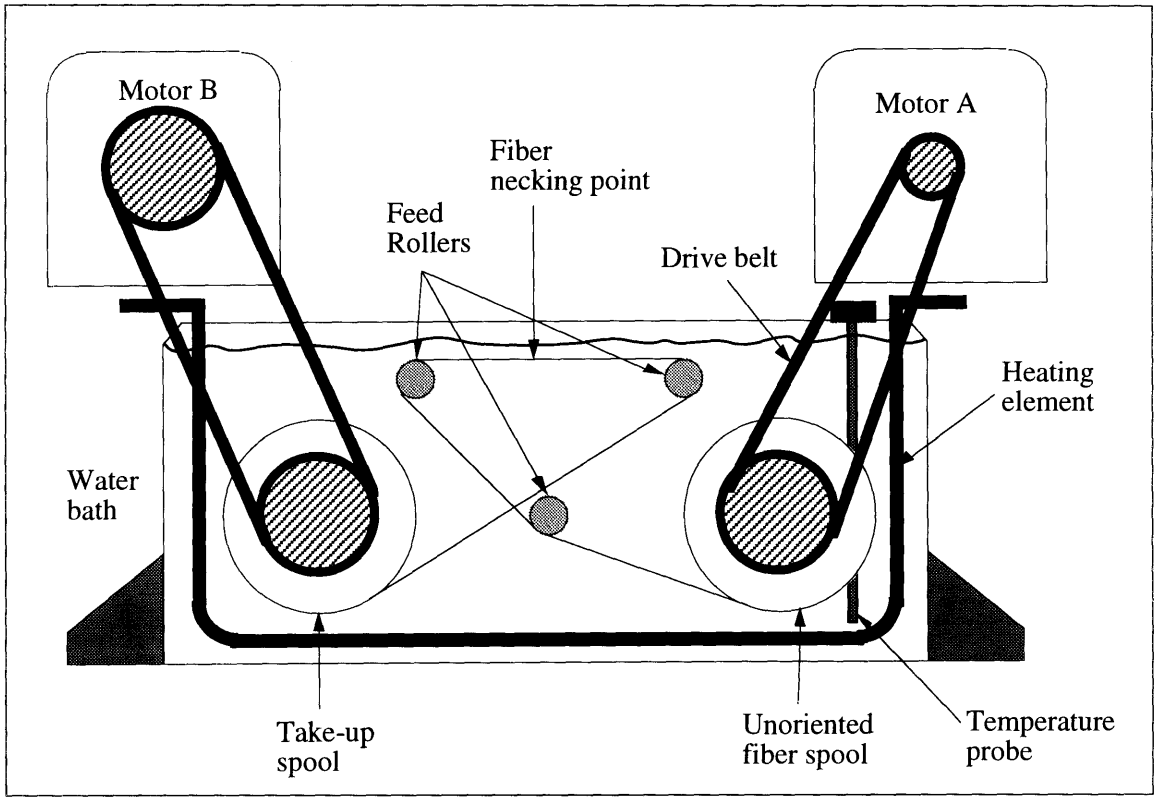

Figure 3-5: Water bath used to orient HDPE fibers.

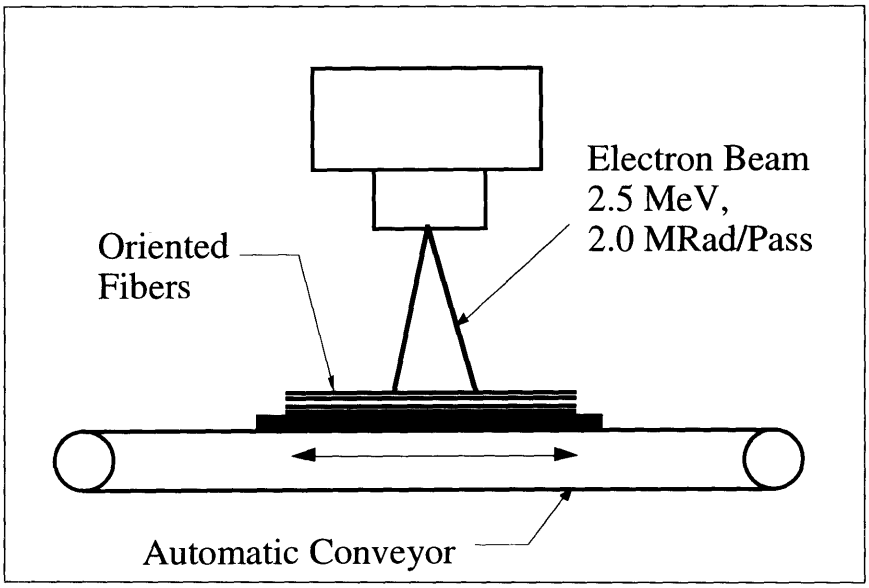

Figure 3-6: Irradiation of oriented fibers by electron beam irradiation [2].

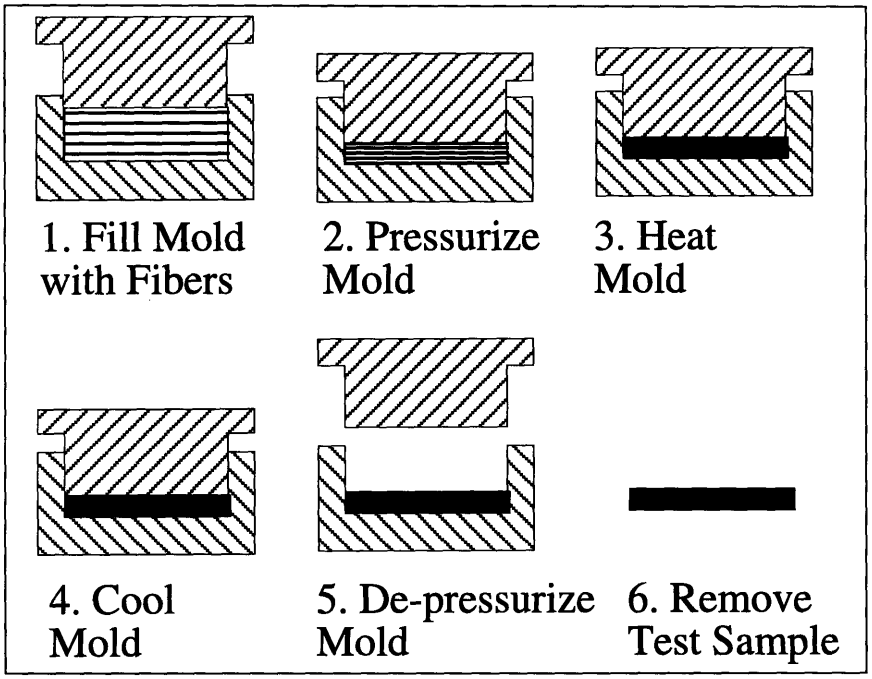

Figure 3-7: Compression molding of crosslinked, oriented HDPE [2].

did the other two cases. Though ultra-tough high density polyethylene offered much improvement over HDPE pellets, it still had higher wear than the UHMWPE samples. These results led to the reasoning that if fibers which had been strengthened offered improvement over unprocessed HDPE, then possibly the same strengthening process could also improve UHMWPE over untreated UHMWPE. This improvement in UHMWPE forms the basis for the development of the Homocomposite material.

3.4 Homocomposites

3.4.1 Introduction

The idea and actual development of homocomposites arose on the basis of the work done with ultra-tough HDPE. There are various aspects of the homocomposite material which make it unique.

First, the homocomposite as the name implies consists of a composite in

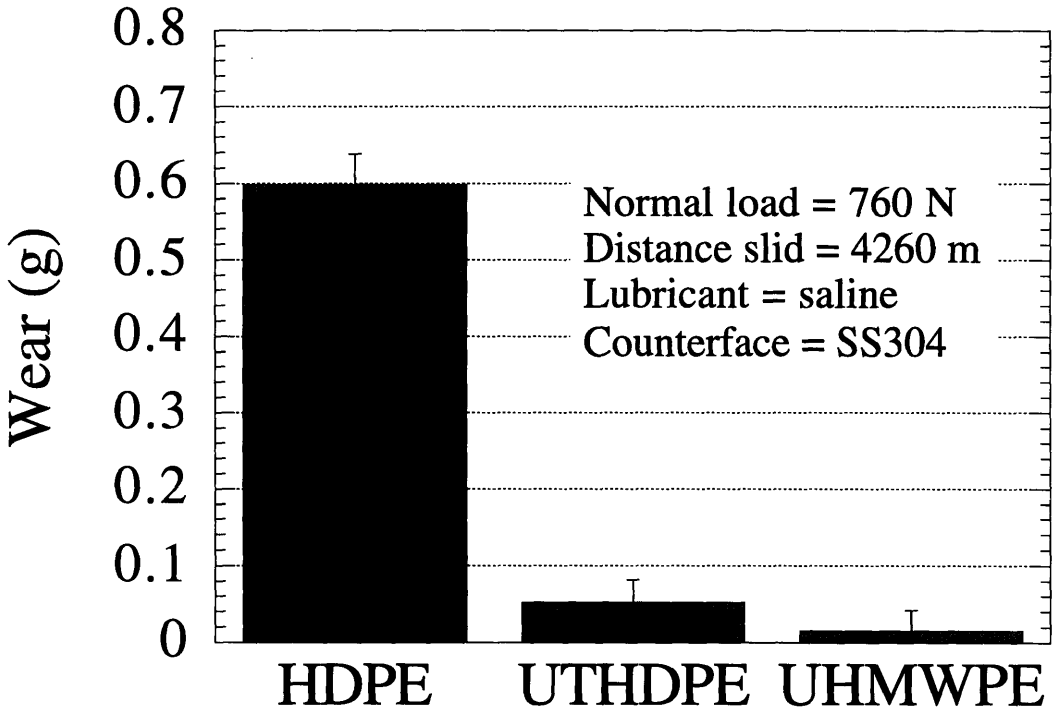

Figure 3-8: Wear of ultra-tough high density polyethylene (UTHDPE) versus HDPE and UHMWPE

which the matrix and fiber are made from the same material. The immediate advantage of this is that since UHMWPE is already in clinical use in artificial joints, reinforcing fibers also made from UHMWPE do not pose any additional risk to the patient than is already present in existing UHMWPE bearing joints.

Secondly, crosslinking of the UHMWPE fibers serves a dual purpose. Crosslinking by γ radiation retains molecular orientation during processing without the use of chemical crosslinking agents. Also, crosslinking creates a processing window through a difference in melting point developed between fibers and matrix. This is discussed in greater detail in Section 4.6 which concerns differential scanning calorimetry. Also, the homocomposite fibers have a normal orientation relative to sliding direction. As was discussed in Section 2.4 such an orientation yields optimum friction and wear performance. The next two sections give the background on the specific properties of the fiber and matrix components of homocomposites.

3.4.2 UHMWPE Matrix

Polyethylene has been in existence since the 1930's, however UHMWPE is a more recent development. UHMWPE was first used in the early 1960's as the bearing material for artificial joints. UHMWPE is produced by stereospecific polymerization with Ziegler-Natta catalysts (a low pressure process)[15, 13, 14]. Also it is a semi-crystalline, linear homopolymer of ethylene.

The medical grade of UHMWPE has smaller quantities of trace elements and impurities than industrial grades. EDA analysis has shown the presence of traces of silicon, calcium, iron, chlorine, aluminum, titanium, molybdenum and of nickel, potassium and sulfur. Furthermore, no antioxidants or stabilizers are added. UHMWPE resin exists in what is generally termed 'flake'. This is essentially a fine powder with a mean particle size of approximately 30 μm. UHMWPE used in the fabrication of the homocomposite was obtained from Hoeschst Celanese with the resin number GUR4150. Table 3.1 shows the trace

Trace Element	Requirements	Tested Value
Aluminum	100 ppm max.	2
Titanium	300 ppm max.	23
Calcium	100 ppm max.	35
Chlorine	120 ppm max.	46

Table 3.1: Trace elements in a sample of UHMWPE, from Westlake Plastics

Property	Method	Specification Requirement	Tested Value
Density	ASTM D1505	0.93-0.94 g/cm^3	0.932
UTS	ASTM D638	4000 psi	6540
Yield Strength	ASTM D638	2800 psi	3050
Elongation	ASTM D638	200 % min	350
Impact Strength	ASTM D256	20 $ft - lbs$	no break
Hardness	ASTM D2240	60	67
Viscosity	ASTM D4020		27

Table 3.2: Mechanical Properties of UHMWPE, from Westlake Plastics

elements from a sample of medical grade UHMWPE obtained from the medical division of Westlake plastics.

In general, UHMWPE has much better tribological properties than does HDPE, this is in great part a direct result of its higher molecular weight (M_w^{HDPE} = 50,000 versus M_w^{UHMWPE} = 3-5 million) which gives it its higher toughness and strength. Shown in Table 3.2 are various other mechanical properties of UHMWPE supplied by the manufacturer Westlake Plastics.

3.4.3 UHMWPE Spectra Fibers

High strength fibers require high to ultra high molecular weights along with high degrees of molecular orientation. Various methods have been used to obtain the necessarily high degree of molecular orientation in polymers such as polyethylene. These include solid state extrusion, solid state fiber drawing, gel/solution spinning, and liquid crystal spinning. According to Tam [77] , no other high strength fiber responds as favorably to molecular orientation as polyethylene.

In general three requirements are specified for high strength fibers [77]: (a) high degree of polymer chain orientation (b) very high to ultra-high molecular weight, and (c) moderate to high degree of crystallinity.

The reasons for using polyethylene fibers have been clearly outlined in Sections 2.4 and 3.3 in describing the initial work with the use of ultra-drawn high density polyethylene. However, these attempts yielded fibers with draw ratios of approximately ten. The need for greater orientation of fibers than could be achieved with the experimental setup in Figure 3-5 led to the use of commercially available fibers.

Spectra fibers were developed and introduced by Allied-Signal Corporation in 1985. Spectra fibers are known as extended chain polyethylene fibers and are made from ultra-high molecular weight polyethylene. These fibers have a crystallinity of about 60% - 85% and also a high degree of crystalline orientation. It is this high degree of molecular orientation that provides the Spectra fibers with their high strength. The Spectra fibers are manufactured using a process known as solution spinning with the added claim that solution spinning can be modified to produce a higher strength and more thermally stable fiber [23]. The process involves dissolving ultra-high molecular weight polyethylene (1-5 million molecular weight) in an appropriate solvent. The purpose of the solvent is to ensure that the polyethylene chains disentangle before spinning. This dilute solution of UHMWPE is then melt spun and the cooling extrudate forms the fiber which is dried to remove solvent. Finally, the fibers are drawn before packaging. Properties of various types of Spectra fibers are listed in Table 3.4.3. Also a comparison of Spectra 900 series fibers to other common composite fibers is shown in Table 3.4.

3.4.4 UHMWPE Spectra Fabrics

Homocomposites were produced in two different ways. The first method consisted of hand layup of fibers, whereas the second method made use of commer-

PROPERTY	Spectra 900 Fibers			Spectra 1000 Fibers			Units
Weight/Unit Length	1600	1200	650	650	375	215	*denier*
	177.8	133.3	72.2	72.2	41.7	23.9	*tex*
Ultimate Tensile	27	28	28	33	33	35	g/den
Strength	2.31	2.40	2.40	2.83	2.83	3.00	GPa
(min)	335	348	348	410	410	435	$10^6\ psi$
	236	244	244	288	288	306	$10^3\ kgf/mm^2$
Modulus	718	850	920	1175	1200	1320	g/den
(nominal)	61	73	79	101	103	113	GPa
	8.9	10.6	11.4	14.6	14.9	16.4	$10^6\ psi$
	6.3	7.4	8.0	10.3	10.5	11.5	$10^3\ kgf/mm^2$
Elongation	4.4	3.9	3.6	3.3	3.1	2.9	%
Density	0.97	0.97	0.97	0.97	0.97	0.97	g/ml
	0.035	0.035	0.035	0.035	0.035	0.035	lb/in^3
Filament	39	38	38	28	30	23	μm
Diameter	1.54	1.50	1.50	1.10	1.18	0.91	lb/in^3
Filaments/Tow	150	120	60	120	60	60	
Denier/Fil	10.7	10.0	10.8	5.4	6.3	3.6	
Yield	5.62	7.50	13.84	13.84	23.98	41.84	mg
	2788	3720	6869	6869	11905	20765	yd/lb
	2551	3402	6281	6281	10886	18988	m/lb

Table 3.3: Properties of Allied-Signal Spectra Fibers

Property	Fiber			
	Spectra 900	Aramid	S-Glass	E-glass
density $\rho\ g/cc$	0.97	1.44	2.49	1.86
Filament Diameter (μm)	38	12	9	7
Elongation	3.5	2.5	5.4	0.6
Tensile Strength 10^3, psi	375	400	665	340
Specific Strength 10^6, in	10.7	7.7	7.4	5.0
Tensile Modulus 10^6, psi	17	19	13	50
Specific Modulus 10^6, in	495	365	140	750

Table 3.4: Comparison of Mechanical Properties of Spectra fibers to other fibers

Fiber	Total Energy Absorbed ($ft-lb.$)	Specific Energy Absorbed ($ft-lb/lb/ft^2$)
Spectra 900	33.4	58.6
E-glass	34.5	31.9
Aramid	16.1	22.4
Graphite	16.0	19.3

Table 3.5: Comparison of Spectra fibers energy absorption to other fibers

Property	Value
Style	955
Weave	Plain
Count Ends/in.	56x56
Yarn Denier	
Warp	215
Fill	215
Weight oz/yd^2	3.2
Thickness, μm	175
Breaking Strength	
lbs/in	580x560

Table 3.6: Material properties of Spectra 1000 fabric, from Clark-Schwebel

cially available woven fabric. Though there are potentially other more sophisticated weaves and knits available, the plain weave was selected for its simple structure which could be subjected to analysis. The fabric selected was obtained from Clark-Schwebel and has the properties listed in Table 3.6

Figures 3-9 and 3-10 are scanning electron microscope micrographs of a sample of Spectra 1000 fabric prior to any processing.

3.5 Production of Homocomposites

3.5.1 Manufacturing Process

This section describes the process required to produce a sample of homocomposite for wear testing. The main steps are virtually identical whether the homocomposite is made from fibers or fabric. The first step in the process begins with gamma irradiation of fibers and/or fabrics (the effect of irradiation will be discussed in greater detail in Section 3.5.3). Once fibers have been irradiated they must be cut to length. In the case of fiber-based homocomposites, the fibers were grouped into bundles approximately 0.5 inches in diameter and cut to a length equal to the width of the opening of the mold (0.630"). See Figure 3-11 for a drawing of the mold used. The fiber bundles were then

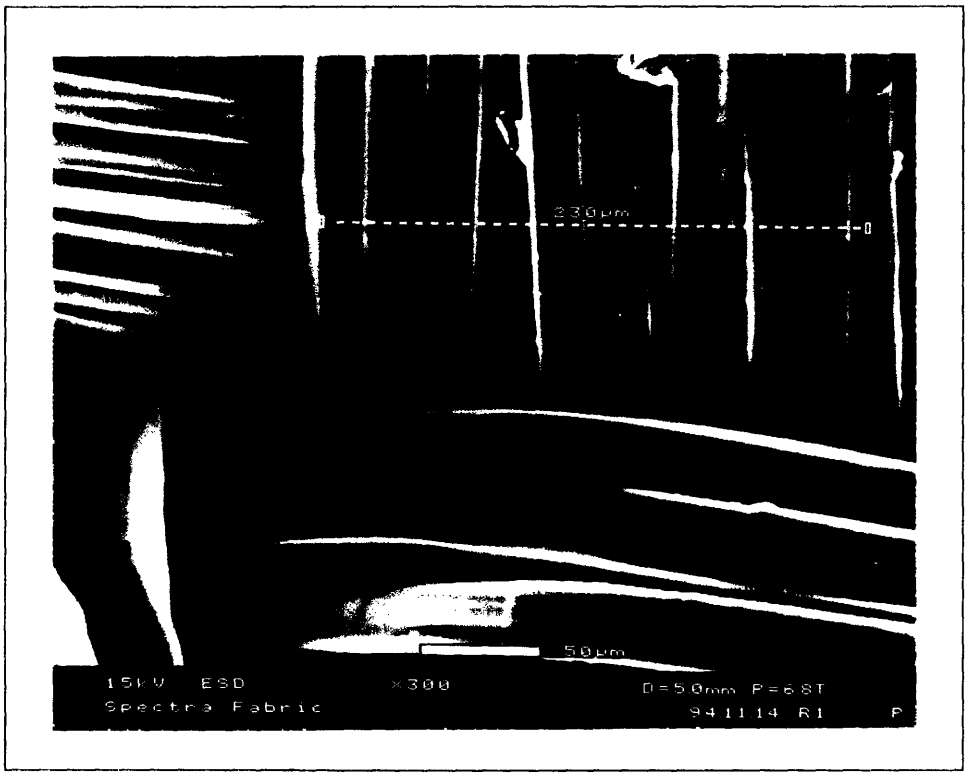

Figure 3-9: Plain woven Spectra 1000 fabric, style 955, magnification 125X

deposited inside the mold cavity and resin (powder form) was mixed into the bundles manually. The desired V_f was achieved by mixing enough resin to give the correct weight proportion of fiber to resin. Mixing of the two phases was performed manually.

One important issue in the manufacture of homocomoposites is the need to obtain a uniform fiber network within the matrix. The hand layup of Spectra fibers discussed above is both labor and time intensive. For this reason another means to achieve consistent uniform fiber orientation was sought. This need led to the use of commercially woven Spectra fabric. Instead of cutting individual bundles of fibers and manually spreading them into a thin layer; one sheet of plain woven fibers could readily be inserted into a mold cavity to instantly give a uniform layer of fibers. This increase in uniformity comes at the expense of a reduction in the density of normally oriented fibers, since with a plain weave, half of the available fibers are vertically oriented and the other half is

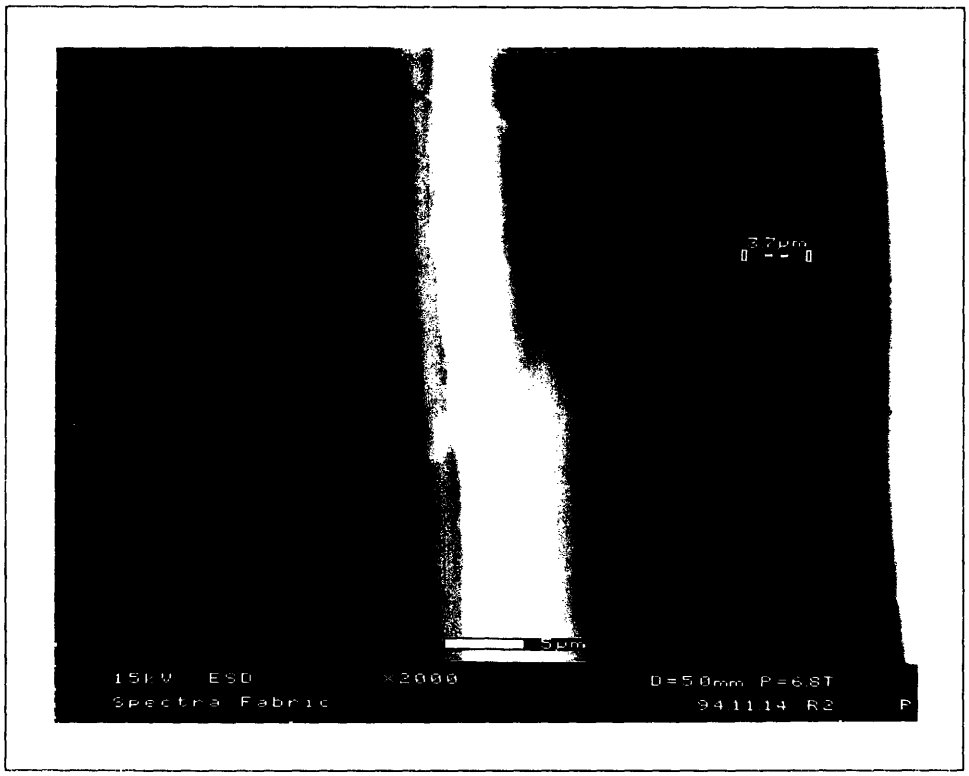

Figure 3-10: Plain woven Spectra 1000 fabric, style 955, magnification 1600X

horizontally oriented.

In this case of the fabric-based homocomposite, the cutting of fabric was done with a specially made 'fabric-cutter' (see Figure 3-12) such that cut sheets of fabric could be placed inside the mold cavity . This fabric cutter was needed because of the difficulty in cutting Spectra fibers. The cutter is designed to hold fabric in tension while it is being cut to the size of the mold cavity opening. The V_f. is achieved in the same manner as with the fiber method. The placement of cut fabrics into the mold involved placing each small sheet of fabric (4.0"x0.630") into the mold and then lightly sprinkling UHMWPE powder on top of each fabric after it had been placed. This manual deposition of UHMWPE powder is a source of variation in the distribution of the thicknesses of the fiber-matrix phases.

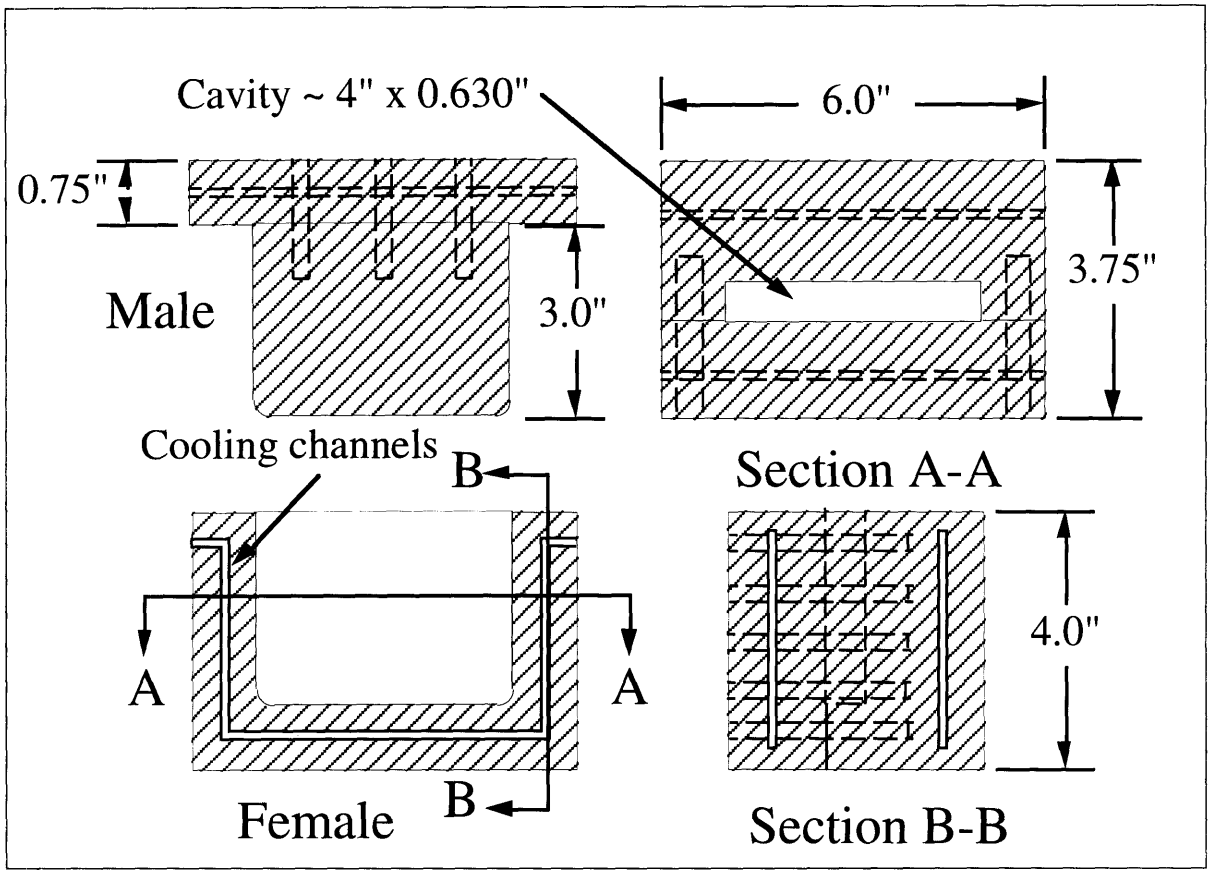

Figure 3-11: Aluminum mold used to produce homocomposites

3.5.2 Material and Processing Parameters

Several parameters all serve to influence the consistency and uniformity of the manufactured homocomposite. These parameters can be grouped into two main groups. The two broad classifications are material parameters and processing parameters. Under the first classification are the material parameters of volume fraction, level of irradiation, and uniformity of fiber-matrix phases. The second classification deals with the actual manufacture of the homocomposite and includes variables such as molding temperature, temperature distribution of the mold, molding time, and molding pressure. These variables were identified as manufacturing and wear testing data accumulated during the course of the development of the homocomposite.

Various temperature conditions were tried in order to find an optimum op-

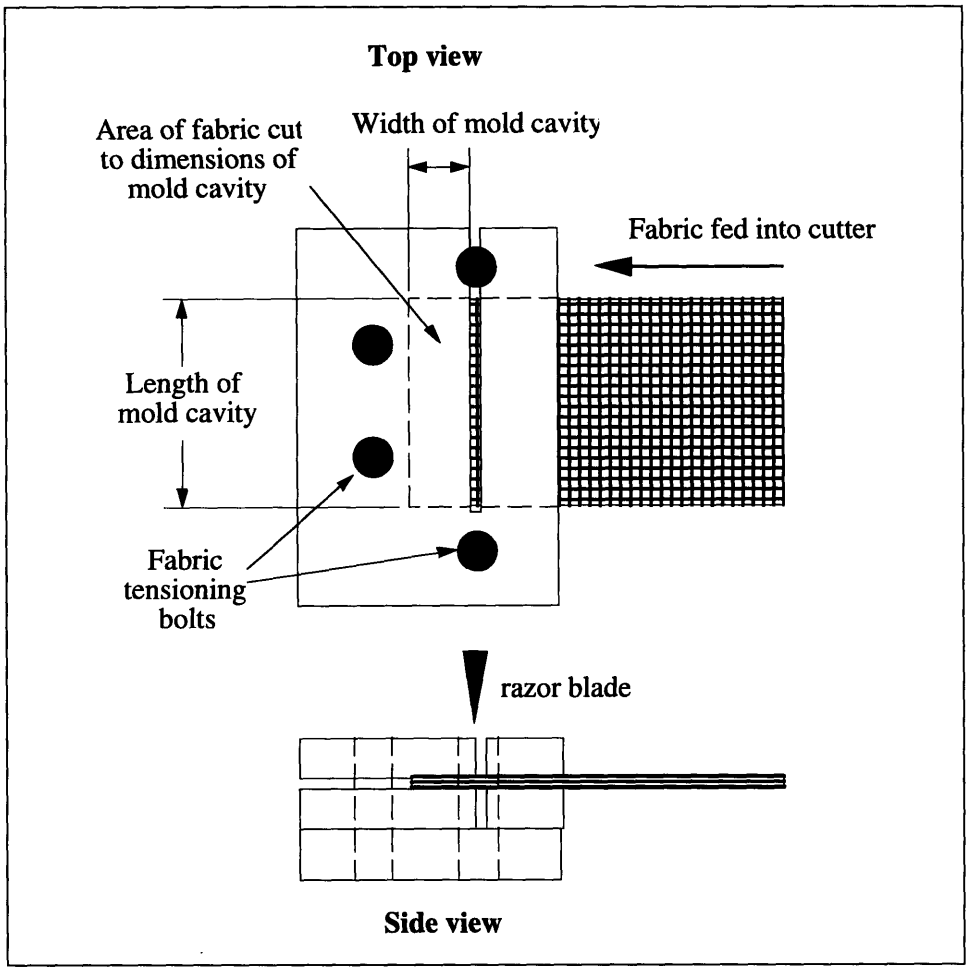

Figure 3-12: Device used to hold and cut Spectra fabrics

erating processing range. For this purpose, samples were made at 130°C, 140°C, 150°C and 160°C . It was found that 130°C yielded poor samples with the GUR 4150 resin not fully melted. At 140°C, samples were better consolidated however problems persisted with delamination failure of the fiber matrix bond. At 150°C samples showed much better bonding. At 160°C, consolidation between fiber matrix is excellent; however, thermal degradation issues begin to arise as samples exhibited signs of discoloration.

A molding time of a minimum of one hour was chosen to ensure adequate diffusion through the thickness of the sample. This is an important parameter which affects the strength of the fiber-matrix bond. The mold schematically shown earlier in Figure 3-11 has an unsymmetrical geometry leading to uneven

thermal distribution. The piston has a gradient along its length because its narrower cross-sectional area is exposed to convective cooling by air currents. This effect is somewhat reduced when insulation is used around the mold.

Pressure application is maintained throughout the molding cycle. The same principle used in the molding of the HDPE samples is also used in the molding of the homocomposite. Upon placement of the mold into the press, pressure is immediately applied and maintained throughout the heating and cooling phases of the mold cycle. Once again this ensures that by maintaining pressure on the fibers they will not lose their high degree of molecular orientation.

The molding pressure used was approximately 1500 psi (10.34 MPa). During molding there are some pressure drops which occur but these are corrected for by the pressure controller. It was found that steady application of pressure is necessary to ensure good fiber-matrix consolidation. The key is that a minimum pressure must be applied to achieve consolidation. A pressure greater than this minimum amount does not necessarily contribute to better material properties. In fact, excessive pressure will squeeze out the resin and extrude it through the clearance between the male and female walls of the mold. This results in fiber-rich and matrix-poor areas. Furthermore, when this minimum pressure is not achieved, the risk of voids in the bulk of the material also increases. Such voids become crack propagation sites for delamination of the fiber layers.

3.5.3 Irradiation

Irradiation of polymers is an effective means of achieving certain desirable mechanical properties not originally present in the material. The crosslinking benefits of irradiation were discussed in Section 3.3. In the various forms of polyethylene, crosslinking leads to formation of primary bonds between the carbon molecules in adjoining molecular chains. Such bonds between neighboring molecular chains can impart greater mechanical strength to the bulk material along with an increase in toughness. These are macroscopic phenomena which

can be observed when a polymer is crosslinked.

The potential benefits of radiation exposure can readily be lost and even lead to material degradation if the radiation dosages and rates are not administered in the correct quantities or at the appropriate rates. There is a limit to how much irradiation the polymer may be exposed to before degradation in mechanical properties occurs. Excessive dosages of radiation leads to an increase in the brittleness of the material. In extreme cases, a thermoplastic can attain properties similar to those of thermosets should the material in question receive a large dosage of radiation.

With artificial implants, the motivation behind irradiation of polyethylene implants is not to attain better mechanical properties, rather it is to achieve an acceptable level of sterilization for biological use. With this type of sterilization method utilizing irradiation, it is important to know the extent to which (in the case of UHMWPE) damage to the molecular structure occurs. There are many important issues which must be considered when subjecting polymers, especially polyethylene, to irradiation. The dosage, dosage rate, radiation type and irradiation atmosphere are all important parameters which can ultimately affect the resulting molecular structure present after the treatment has been carried out. These parameters have been investigated by various researchers [58, 42, 63, 66, 68, 67]. The dosage parameter and how it affects friction and wear of UHMWPE and homocomposites is discussed in the next chapter.

Chemical Effects of Irradiation in Polyethylene

Many of the observed changes in mechanical properties can be traced to the changes which occur at the chemical level as a result of irradiation. For this reason it is important to examine the chemical events which occur simultaneously. There are several events which occur at the chemical level as a result of irradiation in a polymer such as polyethylene. These events include breakage of C-C and C-H bonds leading to production of unsaturated groups, liberation

of H_2 gas, chain scission, crosslinking between molecular chains, and oxidation. Streicher [67] proposes these mechanisms (see Figure 3-13) as occurring in polyethylene as a result of exposure to radiation.

Also, it is suspected that after irradiation has occurred that postcrosslinking and postoxidation can occur in UHMWPE as latent free radicals trapped in crystalline regions migrate to amorphous regions [67]. The effect of irradiation on melting point is discussed in Section 4.6 in the DSC analysis of melting points of Spectra fabric.

Evidence of oxidation in polyethylene can be correlated to the increased presence of carbonyl groups C=O in the material. In general, oxidation has been shown to cause chain cleavage and to increase the brittleness of the UHMWPE. Associated with this decrease in the elasticity of UHMWPE are increases in density, yield strength, ultimate tensile strength and hardness. Increased water absorption has also been attributed to the effect of irradiation.

Radiation Sources

Two types of irradiation have been investigated in this work: gamma irradiation from a Co_{60} source and electron beam irradiation. There are advantages and disadvantages associated with each of these types of irradiation. In the early work with the ultra-drawn HDPE fibers, electron beam irradiation was used because of size restrictions on the amount of material that could be exposed. Irradiation was performed in the High Voltage Research Laboratory at M.I.T. using a source operating at an energy of 2.0 MeV. Typically, batches of fibers wound on aluminum plates were subjected to 0.25 MRads per pass. Although electron beam irradiation offers such benefits as shorter irradiation times and variable intensity, disadvantages such as low penetration and material heating require multiple exposures of thinly layered specimens to achieve the desired dosages. Gamma irradiation was used in the irradiation with fabric-based homocomposite samples because of the uniformity of penetration which

these gamma rays offer. It is important to note that the gamma irradiation is used by the medical community at levels of 2.5 MRad to achieve sterilization. In the production of the homocomposite, the levels of irradiation have been much lower, typically 0.15 MRad and 0.5 MRad.

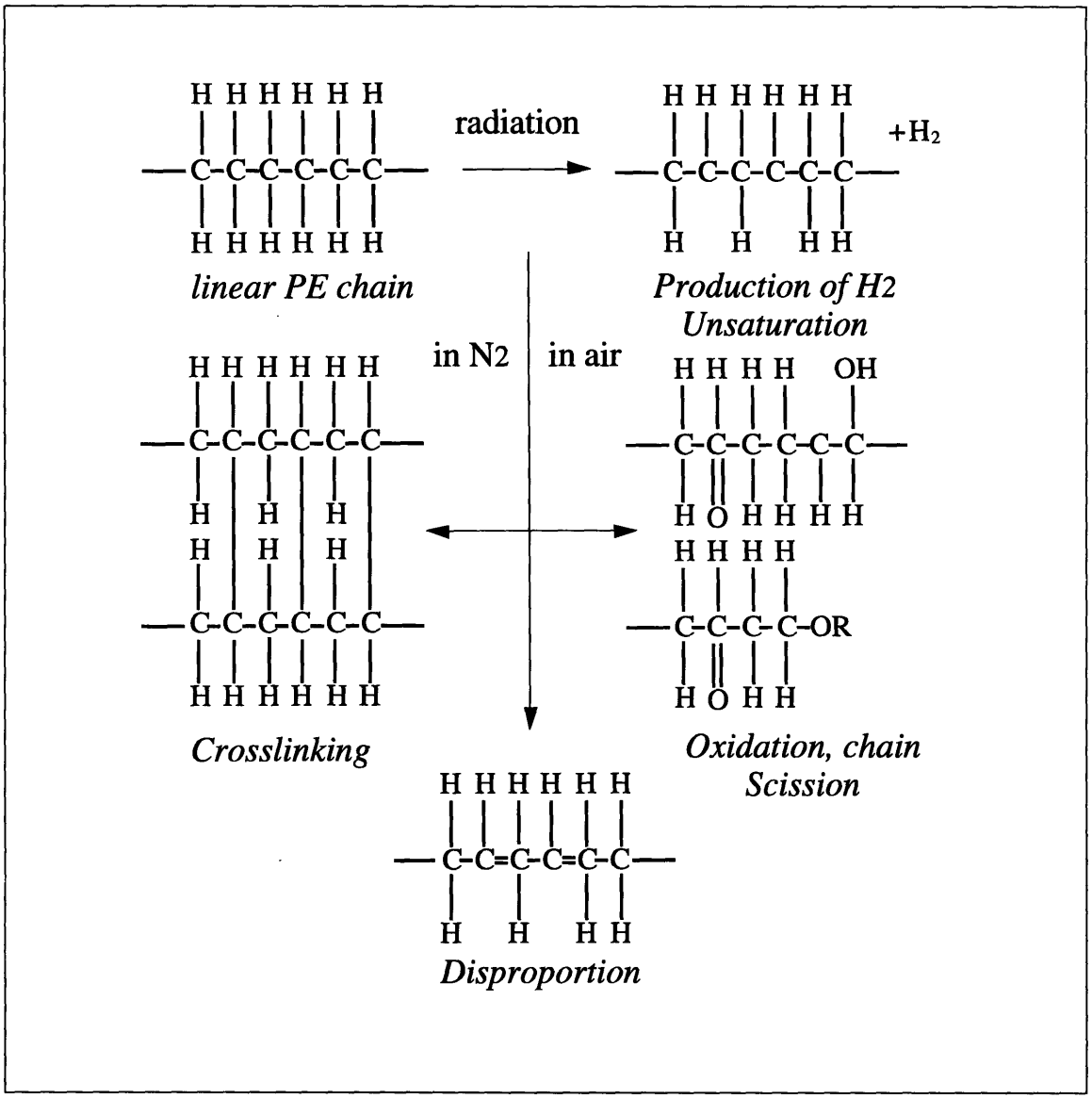

Figure 3-13: Chemical effects of irradiation exposure in polyethylene [67].

Chapter 4

Experimental Results

4.1 Introduction

Chapter 2 considered the theoretical requirements necessary for the improved friction and wear performance offered by homocomposites in counteracting the delamination wear process occurring in artificial knee prostheses. This chapter presents the experimental results of tested homocomposites and UHMWPE. The processing and manufacturing of homocomposites and their subsequent performance in testing has been evaluated using various experimental techniques. Though early work on homocomposites began with the use of HDPE, the performance of the homocomposite has been measured against the orthopedic industry standard of UHMWPE.

Although the bulk of experimental work on the homocomposite has focused on friction and wear experiments, additional experimental techniques were employed to compare the physical behavior of the homocomposite with respect to UHMWPE. These other techniques include the use of Environmental Scanning Electron Microscopy (ESEM), profilometry, and Differential Scanning Calorimetry (DSC). ESEM was used extensively to examine the internal structure of the homocomposite as well as to examine the surfaces of the sliding pairs before and

after testing. ESEM is a valuable tool in detecting changes which signal the onset of delamination wear, namely detection of subsurface cracks which when they join and propagate, eventually reach the surface and cause a delaminated wear sheet to come off. The use of a Dektak 8000 (contact type) profilometer provided topographical data about changes occurring during this process as a function of distance slid.

This chapter is organized based upon the experimental approach discussed above. Initially, a discussion into the specifics of friction and wear testing leads into the results of these experiments. To provide greater understanding into these results, the work done on ESEM examination, profilometry, and DSC is also presented.

4.2 Experimental Method

4.2.1 Sample Preparation

Prior to all wear tests a series of steps were followed to prepare the UHMWPE samples for testing. For the UHMWPE and homocomposites, the samples were flycut to give a surface with an average surface roughness of $R_a = 0.5$ μm. Various trials were made at different feedrates and spindle rotational speeds to optimize the surface finish using flycutting. It was determined that a spindle speed of 1600 rpm along with a feedrate of 0.75 in/min yielded a surface roughness of 0.5 μm. The radius of the tool tip was approximately 1/32 in[1]. Samples were cleaned with distilled water, isopropyl alcohol, and then ultrasonically cleaned[2] for one half hour in a bath of distilled water. Samples were then left 24 hours to dry at room temperature prior to weighing before the test was performed. A soak sample was subjected to the same steps as the samples

[1]It is interesting to note that in the case of the homocomposite, unless the tool was frequently sharpened a satisfactory surface finish could not be obtained.

[2]4.6 qt. AmericanBrand Ultrasonic Cleaner

that were actually tested. A similar cleaning procedure was followed for the metallic counterfaces. All counterfaces were ultrasonically cleaned in a bath of isopropyl alcohol for thirty minutes and then left to air dry for thirty minutes and finally were rinsed with distilled water and left to air dry for an additional thirty minutes. Care was taken during handling to minimize contamination so as to not transfer any hand oil to the counterface.

After each test, counterfaces were removed from their holders and placed under running hot water to remove excess residue from the bovine serum. Samples were weighed on a Mettler H51AR balance capable of measuring to a resolution of 0.00001 g. The bath holders into which the UHMWPE and homocomposite samples are fixed were also cleaned under running hot water following all experiments. Prior to all tests, the baths were cleaned with isopropyl alcohol and then rinsed with distilled water before the samples were secured.

At the conclusion of each test, samples were removed from their respective baths and rinsed under running water. Each sample was then wiped dry and allowed to air dry at room temperature for 24 hours. After 24 hours the samples were weighed to obtain the final mass. The soak sample was subject to this same procedure at the conclusion of the test. Once weighing of the samples had been completed, samples were stored in sealed polyethylene bags until further profilometry or ESEM analysis was performed.

4.2.2 Wear Tester

In tribological testing of materials, the requirements to observe certain friction and wear phenomena necessitate that an appropriate tester be used. By an appropriate test apparatus it is meant one which has the correct geometrical configuration and which has the capability to vary, control, and measure critical parameters such as load, sliding velocity, lubricant, test duration, and possibly even sample orientation.

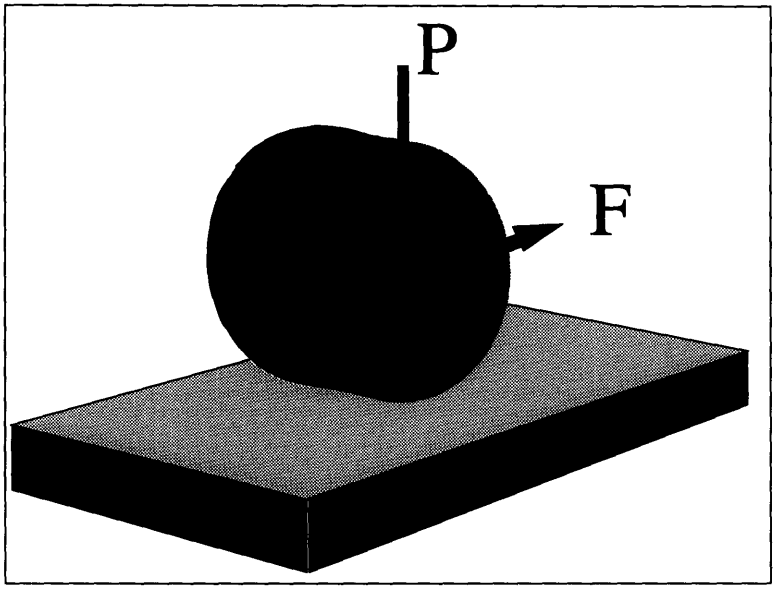

Figure 4-1: Three dimensional geometry of cylinder-on-flat

In tribological testing of artificial joint prostheses there has been much debate over the suitability and applicability of correlating *in vivo* wear tests with observed *in vitro* wear. Not withstanding these arguments, the use of a basic friction and wear test can still provide extremely valuable information with respect to wear processes.

One such process which has been observed and been experimentally verified is delamination wear[73]. Delamination wear as was discussed in Section 2.3 occurs in a sequence of steps in which the rate of subsurface nucleation of cracks due to repeated loading strongly influences the formation of delaminated wear sheets. It is this aspect of the delamination wear process occurring in artificial knee prostheses which can be simulated with the geometry of a cylinder on flat as shown in Figure 4-1.[3] The contact mechanics of such a loading geometry is discussed in Section 5.1 along with the corresponding stress distribution which occurs in the subsurface of the bearing material.

[3]Other wear testing geometries such as sphere on flat (pin-on-disk tester) are also capable of providing cyclic loading required to initiate and propagate cracks. Cyclic loading does not necessarily require oscillatory linear motion, rather it is the cyclic passage of asperities of one surface over another which is important.

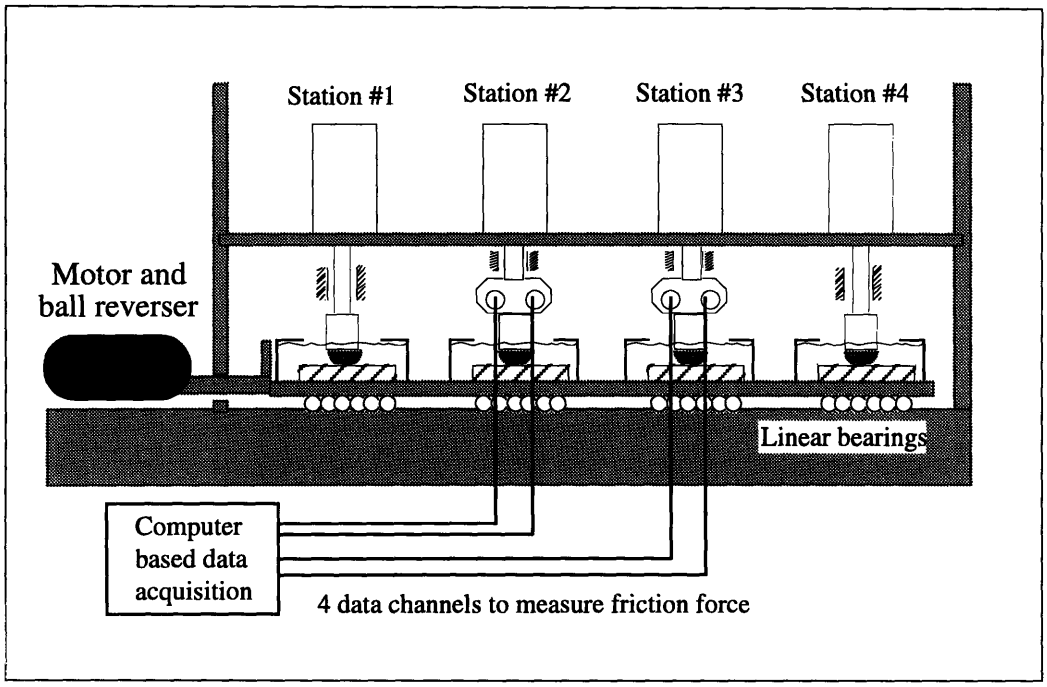

Figure 4-2: Four station cylinder-on-flat wear testing apparatus

The actual wear test apparatus used to generate the basic requirements of the sliding component in an artificial knee prosthesis is shown in Figure 4-2. It comprises four pneumatic cylinders connected to a high pressure N_2 tank (one supply line) so that constant pressure is applied to all four pistons. Two of the four stations have loadcells capable of measuring the applied normal force and the tangential force. The four stations each are bolted down to a common base which oscillates with a linear velocity of 3.4 "/sec over a distance of 1.12". The base moves on linear bearings and is driven by a 1/4 hp motor with a ball reverser coupling to convert rotational motion to oscillatory linear motion. Figure 4-3 shows the ball reverser mechanism.

Wear Tester Loadcells

The two loadcells shown in Figure 4-2 have the capability of measuring friction force and normal load simultaneously. The actual loadcell is shown in Figure 4-4 and is known as an extended double octagonal ring. The locations of the strain gauges are also shown along with the wheatstone circuit diagrams necessary to

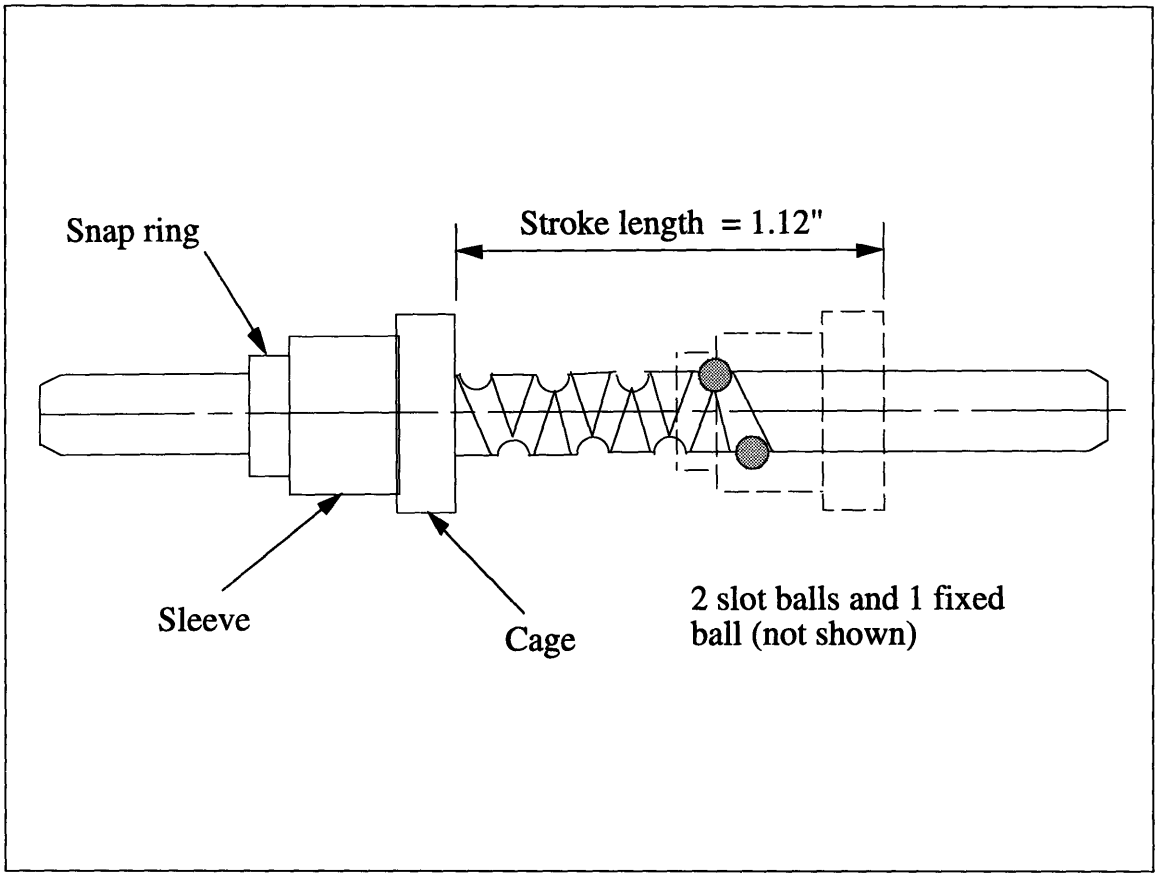

Figure 4-3: Ball reverser mechanism, Flennor Inc. (from technical brochure)

measure these forces. Using such an arrangement ideally provides decoupling of the N and F_f forces. However, due to the unavoidable constraint that the loadcell must be attached on both the top and bottom to a piston rod and counterface holder respectively, a moment of magnitude F_f x d exists.

To determine the sensitivity of the coupling of the N and F_f forces with respect to this moment, a series of calibration experiments were performed by applying known normal and tangential loads simultaneously and measuring the voltage output (see Appendix C for the actual calibration curves). An upper bound of $\mu = 0.2$ was assumed, and for an applied normal load of 170 lbs. (760 N), this corresponds to $F_f = 34$ lbs. In Figure C-2 in Appendix C, it can be seen that a F_f of 30 lbs. introduces a shift in the line of about 0.2 mV from the nominal 4.4 mV. This represents approximately 4.5 % error when $\mu = 0.2$ due to coupling effects. However, for a commonly encountered μ of 0.1 the error is about 2 %.

Wear Tester Data Acquisition System

The block diagram of the connection between the computer-based software and the actual loadcells appears in Figure 4-2. The data acquisition software is written in C-language and reads data from a Metrabyte data acquisition board connected to an external breadboard to which the loadcells are hardwired. The software data acquisition routines were written in order to compensate for the variation in μ which occurs with changes in sliding direction as is the case with this wear tester. In all tests, voltage is continuously read from the board at its maximum sampling rate. The maximum coefficient of friction is measured over a cycle and stored in memory. To find the average maximum friction coefficient, the average is taken of all of these values every 900 cycles. This corresponds to a sampling rate of 5 cycles/second. When a change in sliding direction occurs there is a point at which the sliding velocity is zero - at this point the friction coefficient is zero. Also, as sliding begins in the opposite direction there is a peak

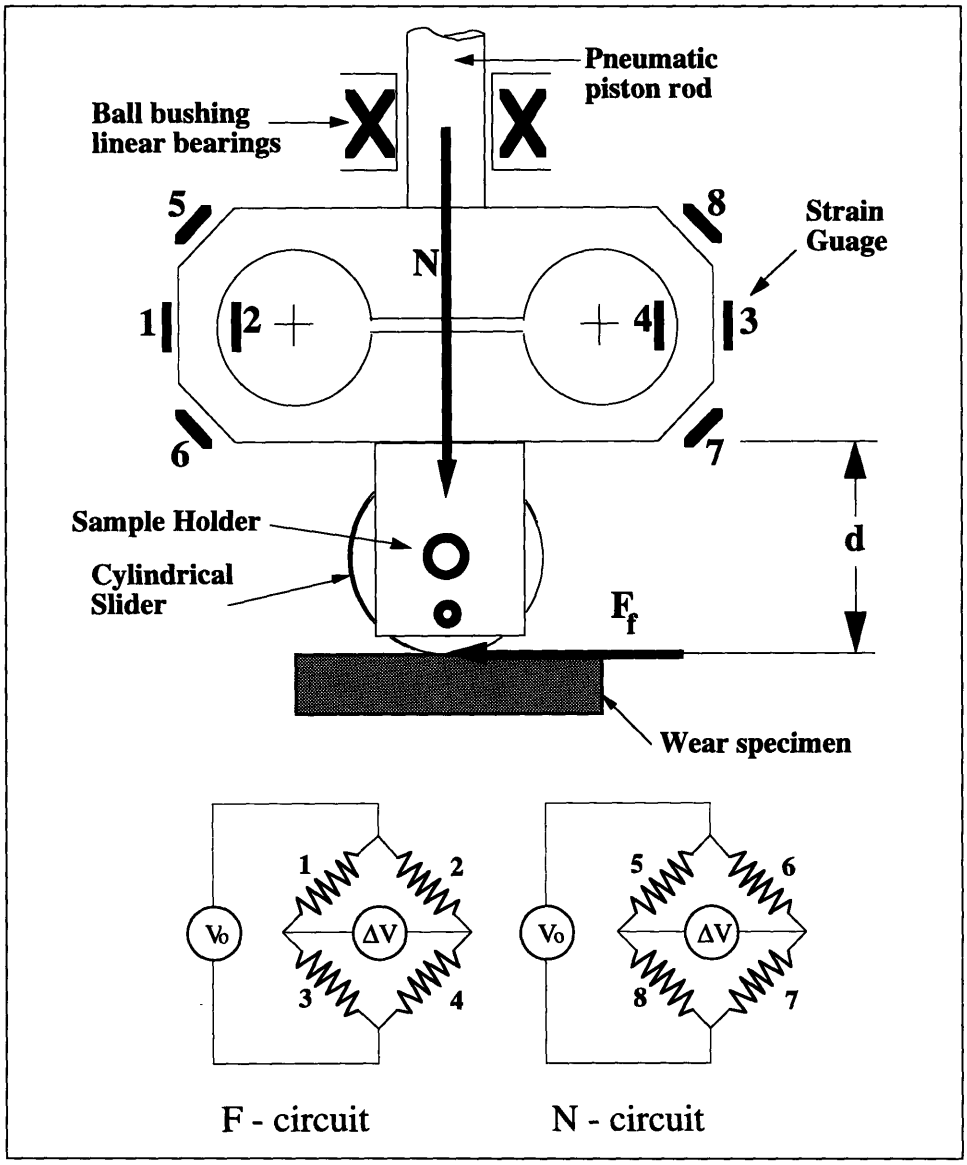

Figure 4-4: Loadcell for measuring normal load and friction force

in the friction coefficient as it changes from μ_{static} to $\mu_{dynamic}$. By performing continous averaging, the short peak does not affect measurements because a small delay is programmed to ensure that these peak readings do not affect the friction data.

4.3 Friction and Wear Experiments

4.3.1 Friction Experiments

Bovine calf serum was used as the lubricant in tests having sliding distances of approximately 7373.7 m, 14747.4 m, and 29494.9 m which correspond to 259200, 518400, and 1036800 cycle tests, respectively. Figure 4-5, Figure 4-6, and Figure 4-7 show the results of three different types of samples tested: 2.5 MRad γ-irradiated (in air) UHMWPE, unirradiated UHMWPE, and homocomposites. The friction coefficient plotted of each material is for only one sample. When measurements were made on the same loadcell, good repeatability was observed.

In these figures several trends are noticeable in the plots of the friction coefficient. First, the irradiated specimens exhibit the highest levels of friction among all the samples for both durations of tests. For the irradiated specimen in Figure 4-7 the friction coefficient drops slightly below 0.08 early in the test, but by the conclusion of the test it returns to 0.08. By comparison, the unirradiated UHMWPE in both test durations exhibits a steady state friction coefficient of 0.06, about 20% lower than the irradiated samples. With the unirradiated sample, it is important to note that the initial coefficient of friction was about 0.05, and in both tests within the first 3700 m slid or so increases to 0.07 and only drops to the steady state value of 0.06 after about 8500 m slid . This indicates that plowing of the surface by the hard asperities present on the counterface is occurring.

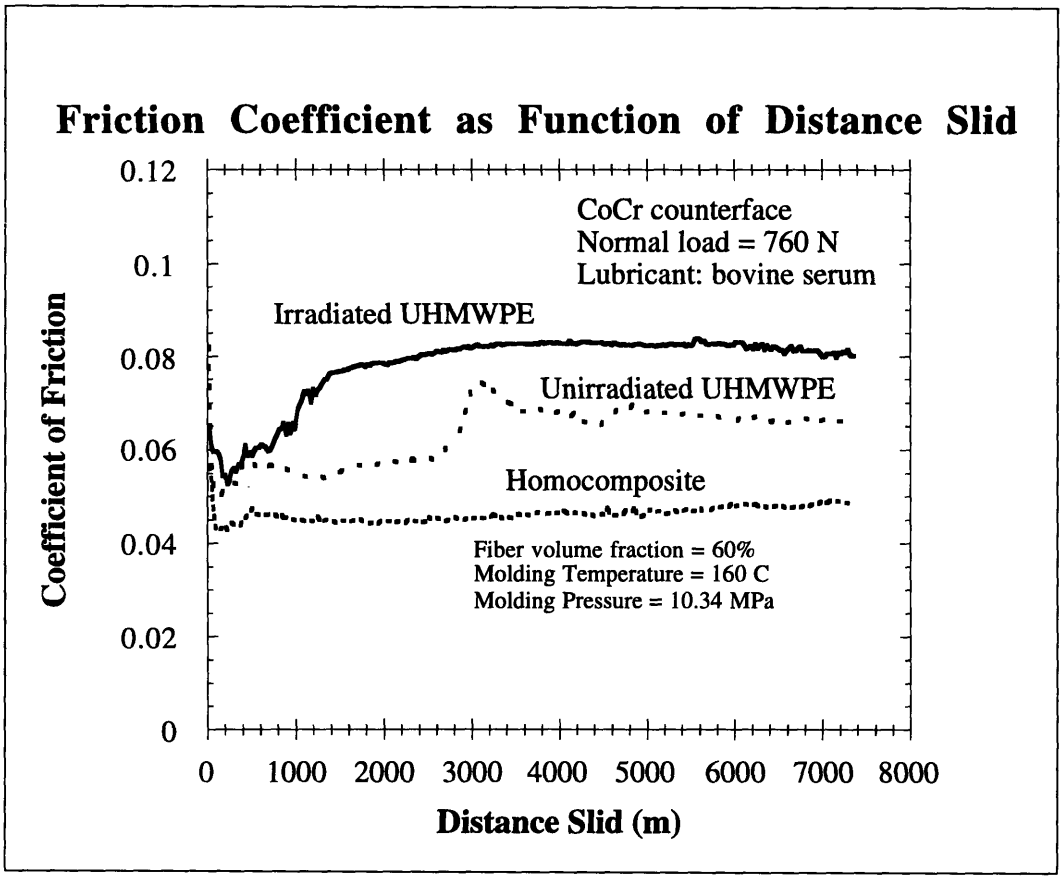

Figure 4-5: Friction test for 7373.7 m slid

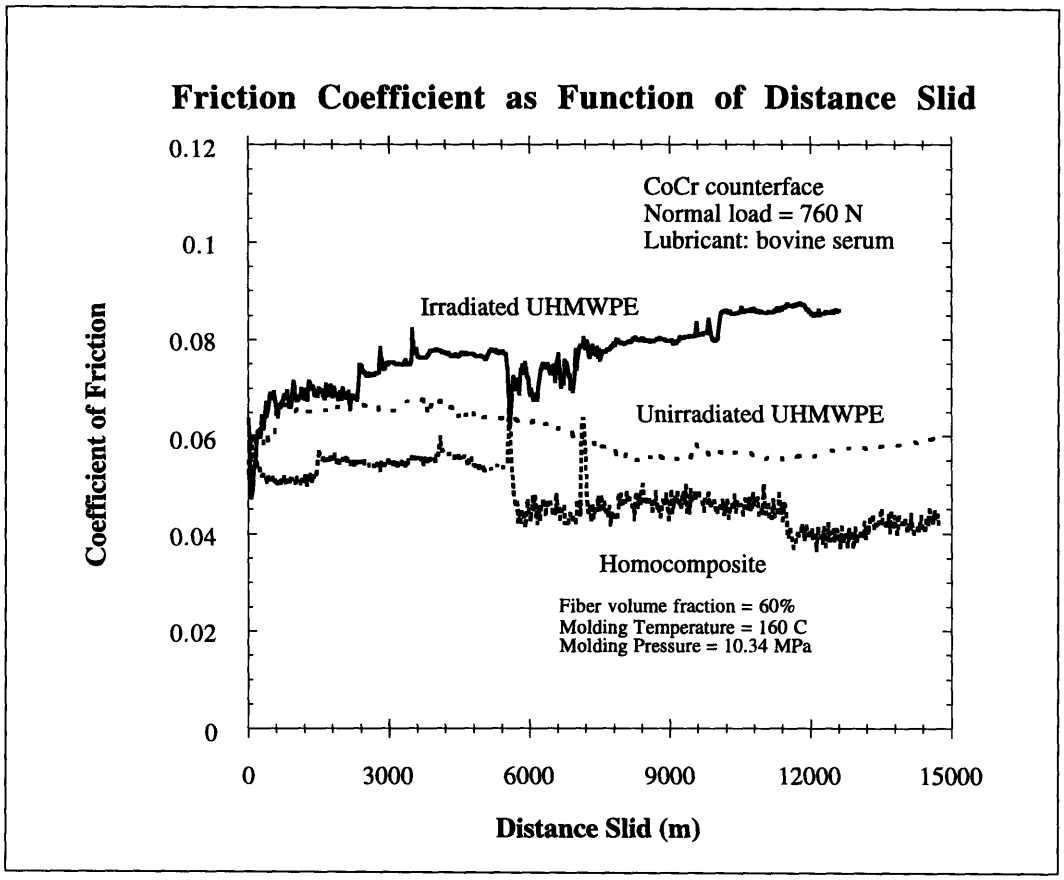

Figure 4-6: Friction test for 14747.4 m slid

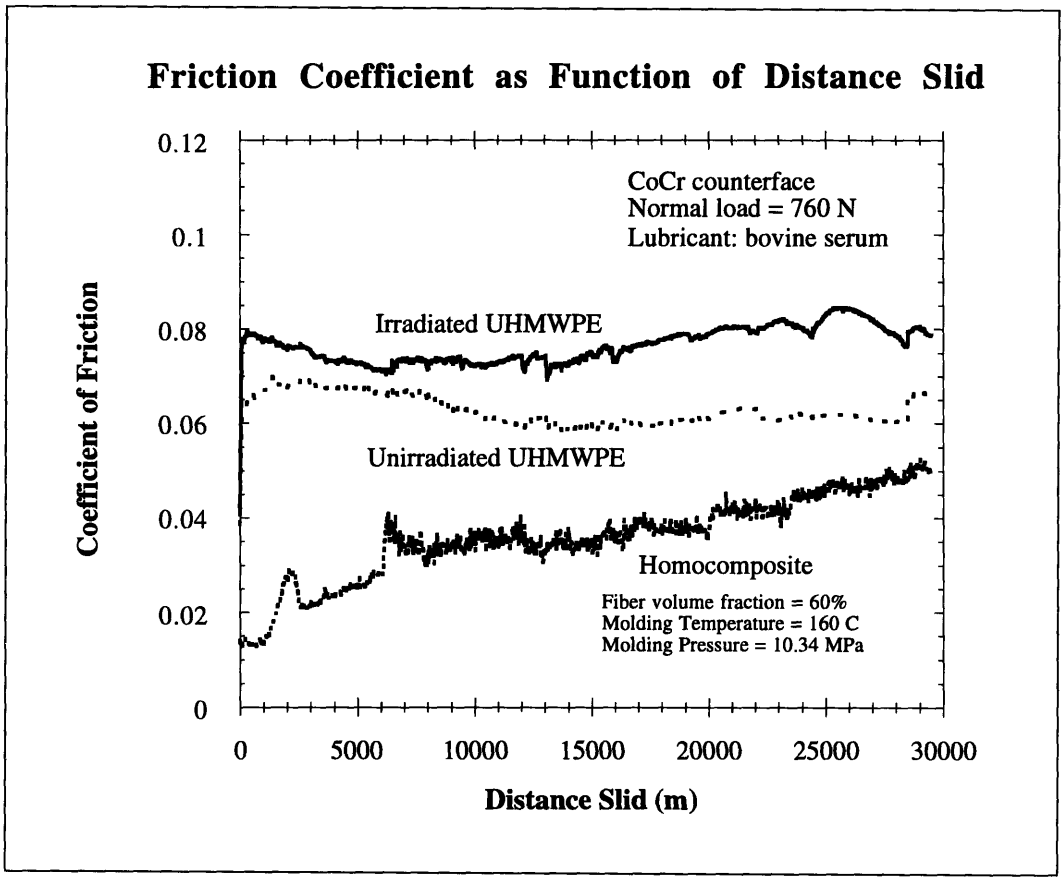

Figure 4-7: Friction test for 29494.9 m slid

Finally, the third specimen was that of the homocomposite. At the outset it should be noted that the samples of homocomposite in Figure 4-6, Figure 4-5 and Figure 4-7 are different because each was made with a slightly different processing method. The homocomposite in Figure 4-6 and Figure 4-5 was made with an aluminum mold and had a volume fraction of 60% and was made by hand layup. In Figure 4-7 the sample also had a volume fraction of 60%; however, it was made using an automated method. Both samples had the same molding conditions of approximately 160°C cavity temperature and 1500 psi (10.34 MPa). The sample in Figure 4-6 displays transitions suggesting the material may be changing as sliding progresses. From an initial value of about 0.05, it decreases to 0.045 before finally reaching the steady state value of 0.04 after 11400 m slid.

Since this sample, as all previous samples, was made by hand layup, the decreasing trend may be explained by the hypothesis that the fiber and matrix phases of the composite may be wearing at different rates. This is also an additional explanation for the "noisier" signal observed. Figure 4-7 on the other hand shows the friction coefficient of the sample made with the more automated method. Here the friction begins at a lower initial value and climbs to 0.05 by the conclusion of the test. This sample showed much steadier frictional force throughout the sliding distance. Furthermore, the occasional sharp peak observed in the homocomposite sample of Figure 4-6 was not present in the plot in Figure 4-7. This offers further support that the sample uniformity is reflected in a more well behaved friction plot. The homocomposite sample in Figure 4-7 was examined under ESEM in Section 4.4.

4.3.2 Wear

Measurement of Wear

In tribology, wear may be measured in different ways. Some of the methods which are commonly used are based on measurement of quantities such as mass, volume, and height (depth of wear track). In this work two methods were employed to check the validity of one method versus the other. The first method used is based on measuring the weight of a sample before and after testing. There are some advantages and disadvantages to this approach. The weight loss method is relatively straight forward to perform as only an accurate reliable balance is required. However, in the case of polymers, this method is greatly affected by moisture absorption. For this reason, great care must be taken to ensure that moisture absorbed is corrected for through the use of soak samples.

The second method employed in this work was that of a volumetric measurement of wear. To perform these measurements, a profilometer was used to measure the cross-section of the wear track. Figure 4-8 depicts how this was done. Using the profilometer described in Section 4.7.2 the wear track of a tested sample is scanned such that the scan is performed across the width of the wear track. Then, the area of the material worn away is calculated using a built-in software function that determines the area above the surface profile and below the zero line. By performing these scans every 0.112", a profile of the depth of the wear track as function of the length of the wear track can be obtained. With this information, the volume of wear can be calculated based on the following equation:[4]

$$\Delta V = \frac{L_{weartrack}}{10} \sum_{i=1}^{10} A_i \tag{4.1}$$

Once the volume of wear is known, the mass of wear can be calculated

[4]The summation equation is not as accurate as a fitting a curve to the data points; however, for the purpose of this calculation, the values are within the standard deviations.

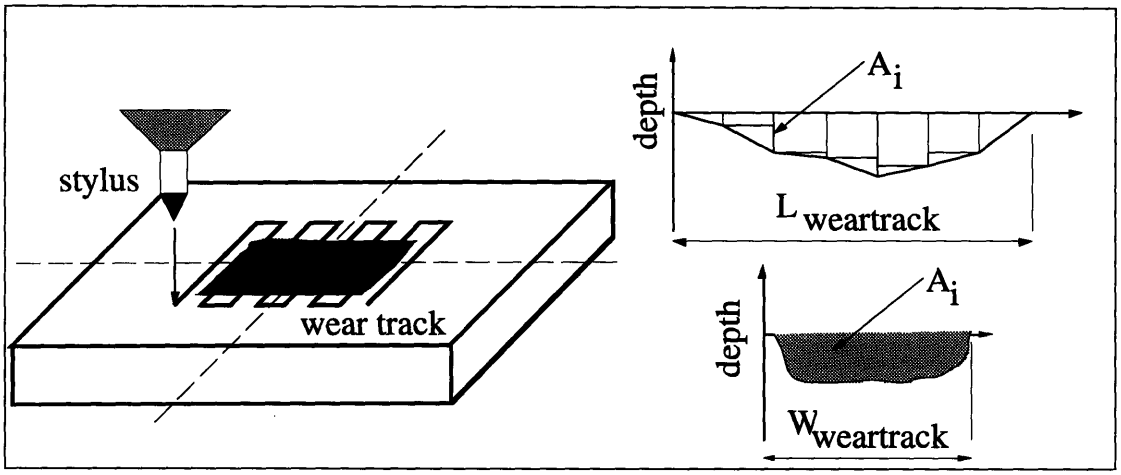

Figure 4-8: Use of profilometry to determine volume of wear

by multiplying ΔV by the nominal density of UHMWPE of 0.932 g/cm^3. The advantage that this method offers over weight measurement is that it is not affected by moisture absorption of the samples. However, a disadvantage of this method is that it is sensitive to creep in the material. Since polyethylene is a viscoelastic material this effect must be compensated for. This is done with the use of a control which is placed under a normal load for the same length of time as the test. Another approach to compensating for the effects of creep is to run a test of much shorter duration (eg., 50,000 cycles) and measure the deformed wear track. Since this wear is negligible compared to wear at 1,000,000 cycles, the deformation can then be attributed to creep. Subtracting the quantity of wear measured at 50,000 cycles from the wear at 1,000,000 cycles gives a value of wear which compensates for creep.

Wear Results

Figures 4-9 and Figures 4-10 show measurement of wear using the two methods described in the preceding section. As with friction testing, wear was measured at 7373.7 m, 14747.4 m, and 29494.9 m sliding cycles for bovine lubricated tests. Similar trends in the measurement of the friction coefficient, are also exhibited in the measurement of wear. First, samples of irradiated (2.5 MRad) UHMWPE

show the greatest amount of wear. In Figure 4-9 irradiated UHMWPE was approximately 33% greater than the unirradiated sample of UHMWPE, and 52% greater than the wear of the homocomposite for a sliding distance of 29494.9 m. For shorter tests of 7373.7 m slid, these differences in wear among the three types of samples are not manifested until approximately 11400 m slid. This in part can be attributed to the effect of moisture absorption on weight measurements.

Although a soak sample was used at all levels of testing, at a low number of test cycles, the weight of moisture absorption is of the same order as the amount of wear. As wear increases, the relative contribution of moisture absorption decreases and the actual mass of wear begins to strongly dominate weight measurements such that the effect of moisture absorption is reduced. This is the reason why the data points and their associated standard deviations are closely grouped at a distance slid of 7373.7 m in Figure 4-9. In all cases in Figures 4-9 and Figure 4-10, a minimum sample size of three was used to calculate the standard deviation.

As wear increases, the standard deviation slightly increases, however the spread between data points becomes more pronounced. In these wear measurements based on weight loss, the standard deviation is in general larger than the standard deviations where profilometry is used to measure wear (Figure 4-10). The reason for this is twofold. First, the affects of moisture gain though they can be corrected for, are still a source of variability. Secondly, there exists variation among the four wear test stations themselves. This is a result of the construction of the wear tester itself.

Though new sample holders were successfully introduced to minimize variation in counterface positioning and alignment, structural inaccuracies in the machine design of the tester cannot be completely eradicated. As an example of this variability, the alignment of counterface holder with respect to the sliding direction was checked with an indicator to an accuracy of +/-0.005". However,

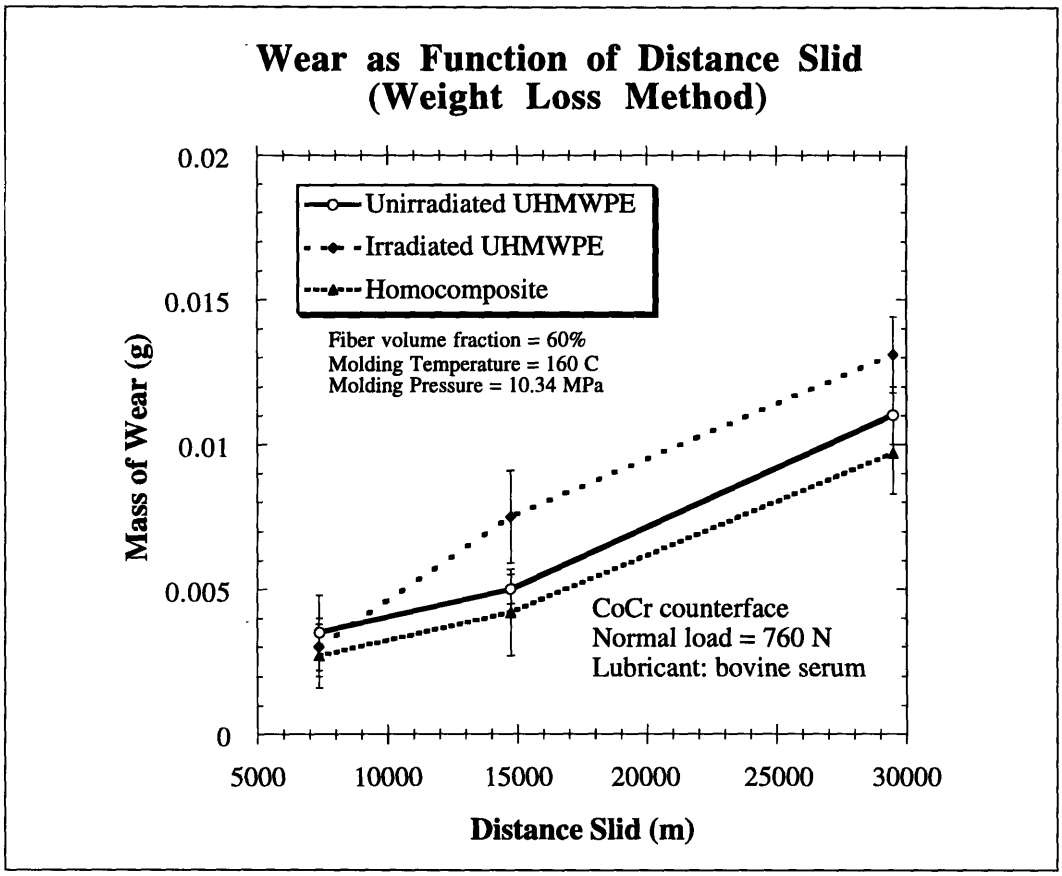

Figure 4-9: Wear results based on mass of wear for 7373.7 m, 14747.4 m, 29494.9 m slid

this tolerance is magnified and readily detected when the wear track is scanned with a profilometer. This is discussed in greater detail in Section 4.7.3.

In addition to the observation that the standard deviation is lower in profilometry-based wear measurements, Figure 4-10 shows two other main points of comparison. First, the relative wear of the three materials remained unchanged with irradiated UHMWPE exhibiting the highest wear followed by unirradiated UHMWPE and finally the homocomposite material. Secondly, wear overall was higher compared to the wear measured by weight loss. The reason for this is the difficulty in accurately measuring the effect of creep with the profilometer. The same approximation that was used to calculate the volume of wear based on ten scans of the wear track is more prone to variance as a function of the locations of scans within the area where the creep test is

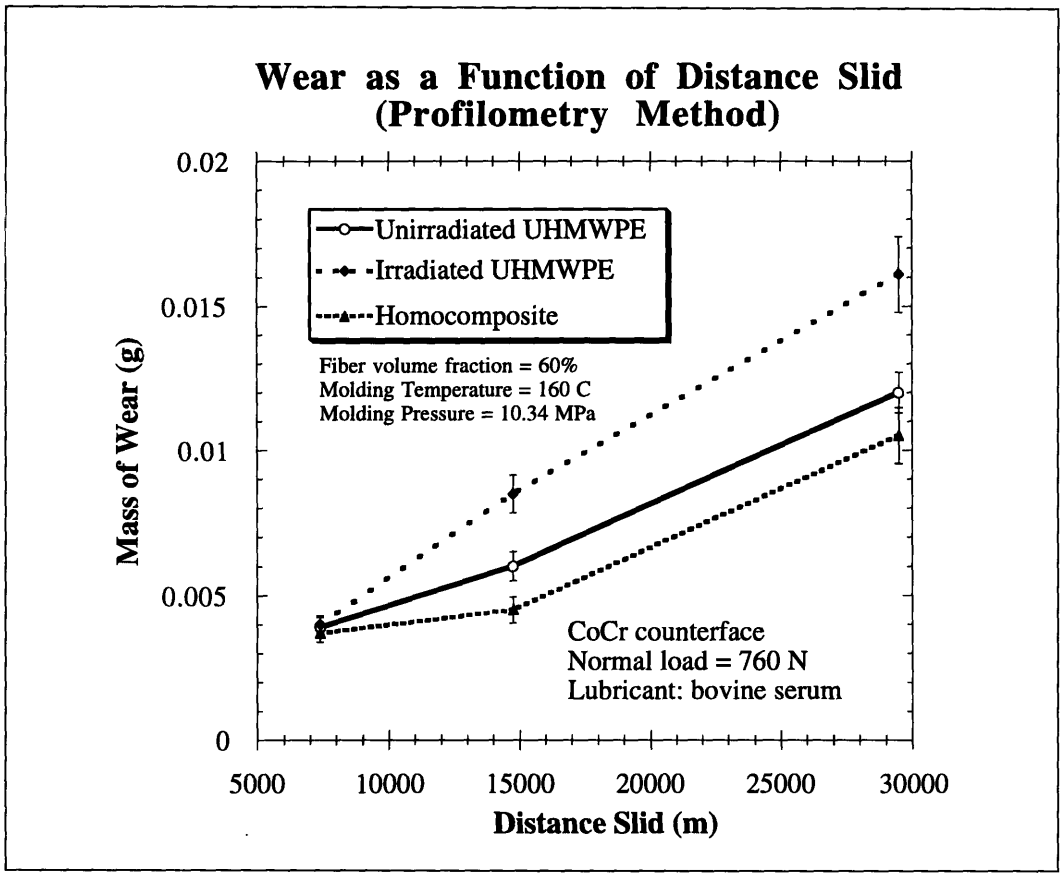

Figure 4-10: Wear results based on use of a profilometer to measure wear for 7373.7 m, 14747.4 m, 29494.9 m slid

performed.

4.3.3 Fiber-Matrix Debonding in Homocomposites

The two previous sections presented the friction and wear data for homocomposites which had not exhibited any anomaly during testing. This section treats the phenomena known as fiber-matrix debonding which can occur in homocomposites if either the pressure or temperature conditions vary significantly from the target values which are used to prevent this problem. The temperature and pressure molding conditions have a great impact on consolidation of the fiber-matrix phases of the homocomposite. If the pressure is low, i.e. less than 1000 psi (6.9 MPa) then voids will be present in the final sample and will be sites

for crack initiation at the fiber-matrix interface. Similarly, if the temperature is not sufficiently high enough, then the matrix will not fully melt and form a good bond with the fiber phase of the homocomposite (155°C to 160°C has shown good bonding).

The results when these conditions are not satisfied are shown in Figure 4-11. These are the coefficients of friction for homocomposites tested in bovine serum. For the reasons indicated on the plot, the homocomposites showed sharp transitions to higher friction coefficients at varying distances slid. The magnitude of these transitions depended on how much deviation from the optimal condition occurred. The sample which exhibited the greatest deviation was the one molded at a pressure of 500 psi (3.45 MPa) and at $T_{mold} = 150°C$. Furthermore, this sample exhibited debonding readily visible on the surface of the wear track. The three samples made at $P_{mold} = 1500$ psi (10.34 MPa) and at $T_{mold} = 140°C$, 150°C, and 155°C by comparison did not show as high a friction coefficient.

To see the actual debonding sites, an ESEM (discussed in greater detail in following sections) micrograph was taken of the worn surface after 29494 m of sliding. These two micrographs of the same image at different magnifications are shown in Figure 4-12 and Figure 4-13. The voids where debonding has occurred are clearly visible in the bright charged areas which is where the matrix no longer is bonded to the fibers. This particular example illustrates the sensitivity of the homocomposite molding process to temperature and pressure as describe in Chapter 3. Clearly, if tight control over these two parameters is not maintained, the result is an inferior sample which does not yield the performance that it is otherwise capable of yielding.

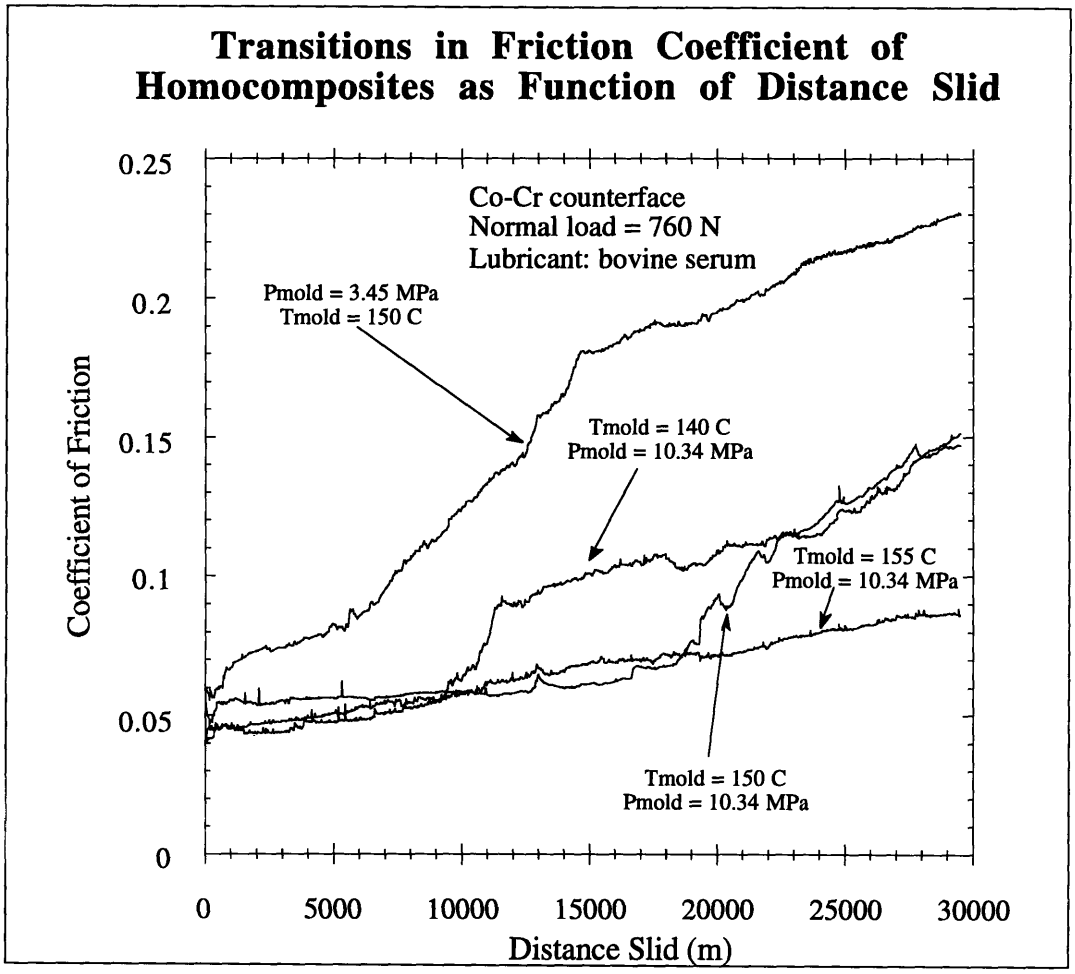

Figure 4-11: Transitions of Friction Coefficient in debonding of homocomposite

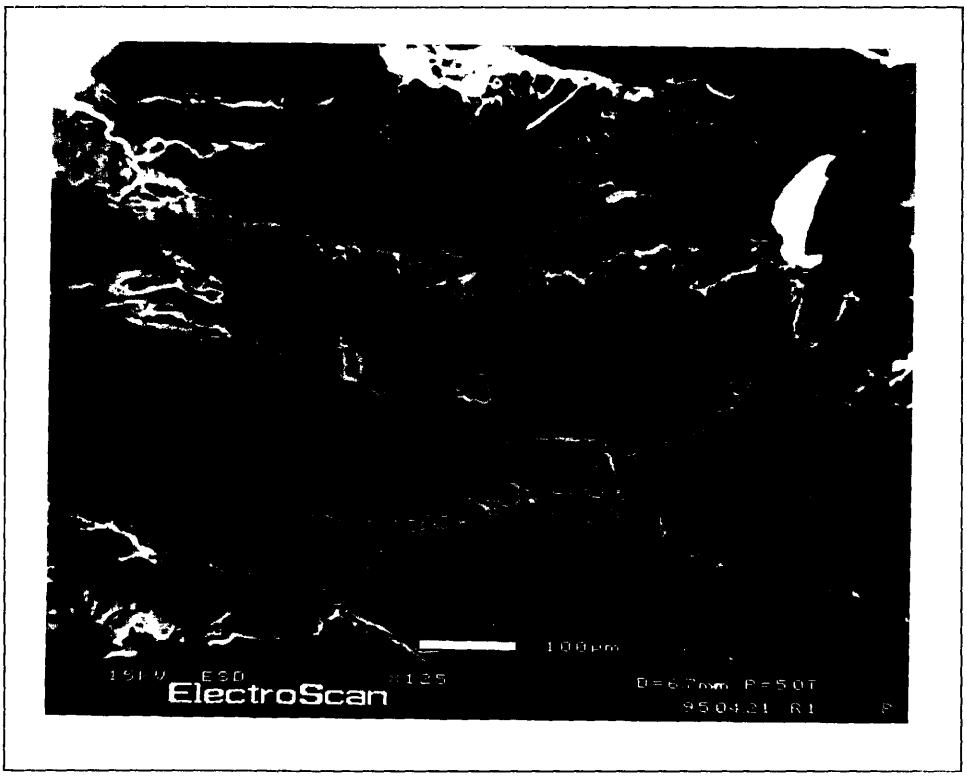

Figure 4-12: ESEM of debonded worn surface of homocomposite, 29494 m slid, 125X

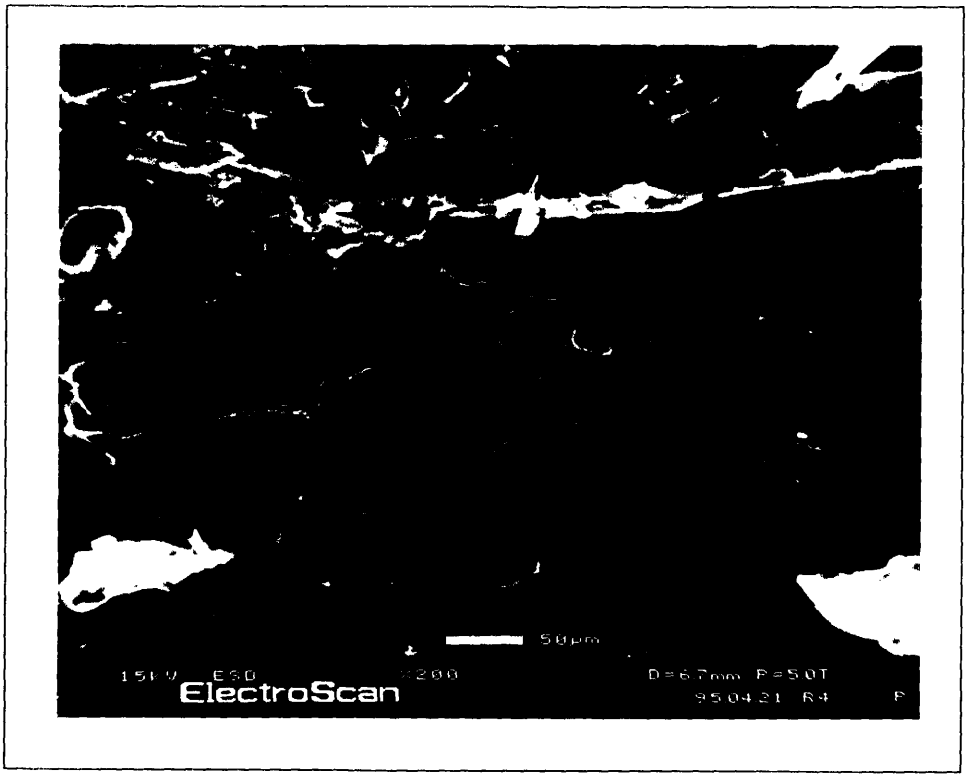

Figure 4-13: ESEM of debonded worn surface of homocomposite, 29494 m slid, 200X

4.4 Examination of Structure of Homocomposite: Freeze Fracture Study

A knowledge of the structure of the homocomposite is vital to understanding its friction and wear behavior. In addition, such knowledge can provide insight into the effect of processing parameters on the fiber and matrix regions of the homocomposite. As was stated in Section 2.3, the homocomposite is highly sensitive to the molding temperature. Specifically, there exists the danger of seriously degrading the resin and more importantly, losing the highly oriented state of the UHMWPE Spectra fibers.

To visually verify the state of the fiber fraction in a particular homocomposite sample, a freeze fracture study was carried out on a sample molded at a temperature of 159°C and which had received a dosage of 0.15 MRad gamma irradiation in vacuum. Since homocomposites are anisotropic it was necessary to select specific viewing orientations of the fractured surface. The two types of fracture samples are illustrated in Figure 4-14. They consist of a sample with the fracture through the fiber axis and of a sample with fracture parallel to the fabric/fiber layers. Small samples having the desired orientation were cut from a larger molded block and then were notched with a band saw. The crack tip was sharpened with a razor blade. Each sample was then dropped into a dewar containing liquid nitrogen and allowed to cool down (until boiling of the $N_{2(l)}$ had stopped). Using a pair of forceps, the samples were taken out of the dewar and quickly placed into a vise. With a hammer and a chisel, a sharp blow was applied and the specimen fractured.

Figure 4-15 shows the fractured surface parallel to the layers of fabric. At a magnification of 125x, the existence of fibers is unmistakable. Furthermore, Figure 4-16 at an even higher magnification of 1600x shows the surface of individual filaments. Both of these figures exhibit blurred boundaries/edges at the resin-fiber/filament interfaces where resin has infiltrated during the molding

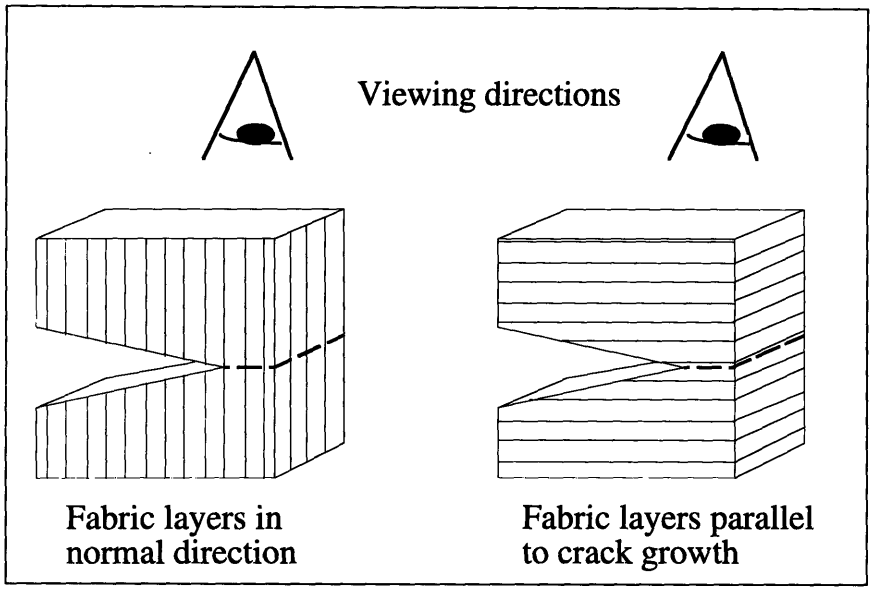

Figure 4-14: Fracture of homocomposite sample

process and where potentially partial melting of the fibers has occurred.

In contrast to these two figures is Figure 4-17 showing the same sample with fracture perpendicular to the fiber/fabrics. The fabric layers, along with the corresponding filaments are less clearly visible than the preceding photomicrographs. At the 125x magnification, the orderly pattern of the plain weave is not visible. Various broken fibers can be seen, and in general the fracture has not left a well cleaved surface for viewing.

From a basic qualitative measure, the fracture of the parallel orientation occurred much more easily than did the normal orientation. This indicates the both higher strength and higher toughness of the homocomposite in the normal orientation. Recall, Figures 3-9 and 3-10 shown earlier of a sample of Spectra 1000 fabric which had not been molded nor irradiated offer a sharp contrast to Figures 4-15 and 4-16 which are of a sample that has been both molded and irradiated. This comparison highlights the changes which the fabric/fibers undergo during molding, namely that under high pressure and high temperature the filaments and resin diffuse into one another.

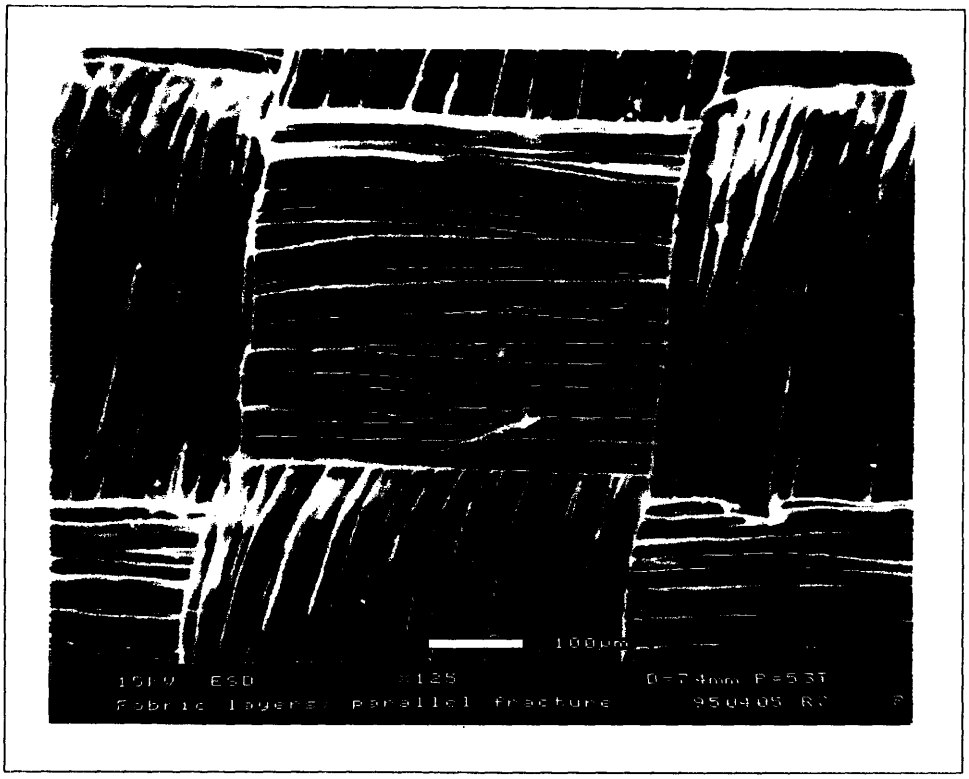

Figure 4-15: Specimen fractured parallel to layers of fabric, $T_{mold} = 159^{o}$C, 125X.

4.5 Examination of Worn Surfaces

4.5.1 ESEM Examination of Polyethylene Wear Tracks

An ESEM study of worn surfaces of UHMWPE was undertaken to examine the polyethylene wear surface as a function of sliding distance. Also the wear surfaces were examined for indications of the wear mechanism present. All tests were performed with bovine serum as the lubricant and with a cobalt chrome counterface. Three types of samples were studied: unirradiated UHMWPE, air-irradiated UHMWPE, and homocomposites. Surfaces were examined after wear testing using an environmental scanning electron microscope (ESEM) and were respectively compared to an untested control (flycut machined surface).

Figure 4-18 is of a flycut surface[5] of unirradiated UHMWPE prior to test-

[5]Flycutting was done at a spindle speed of 1600 rpm with a feedrate of approximately 0.75 in/min.

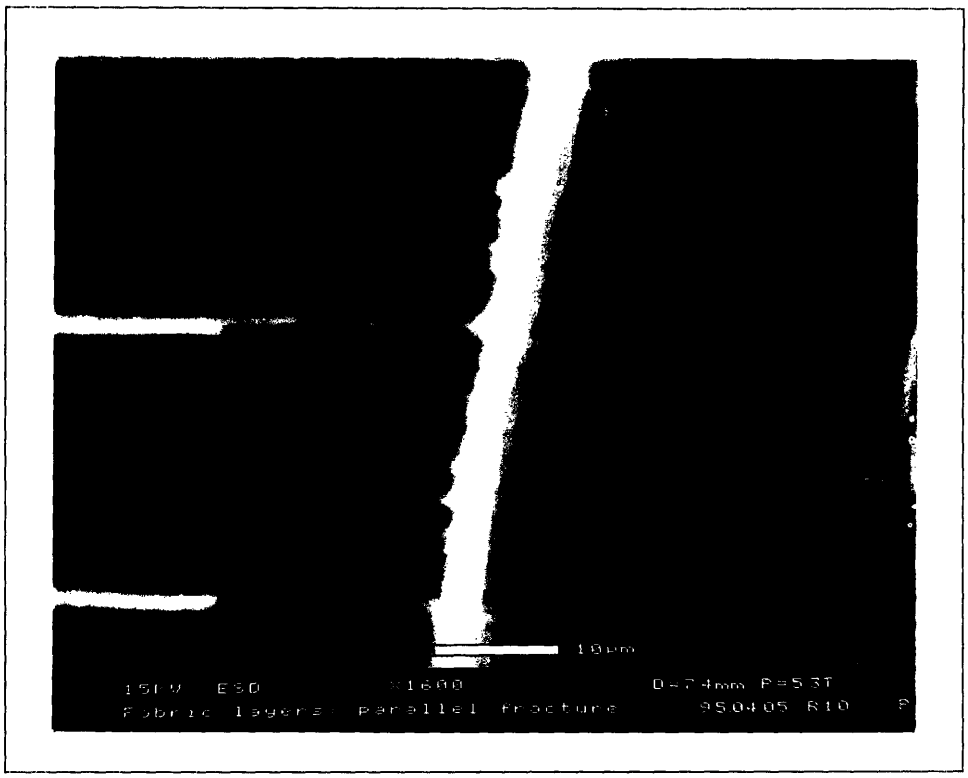

Figure 4-16: Specimen fractured parallel to layers of fabric, T_{mold} = 159°C, 1600X.

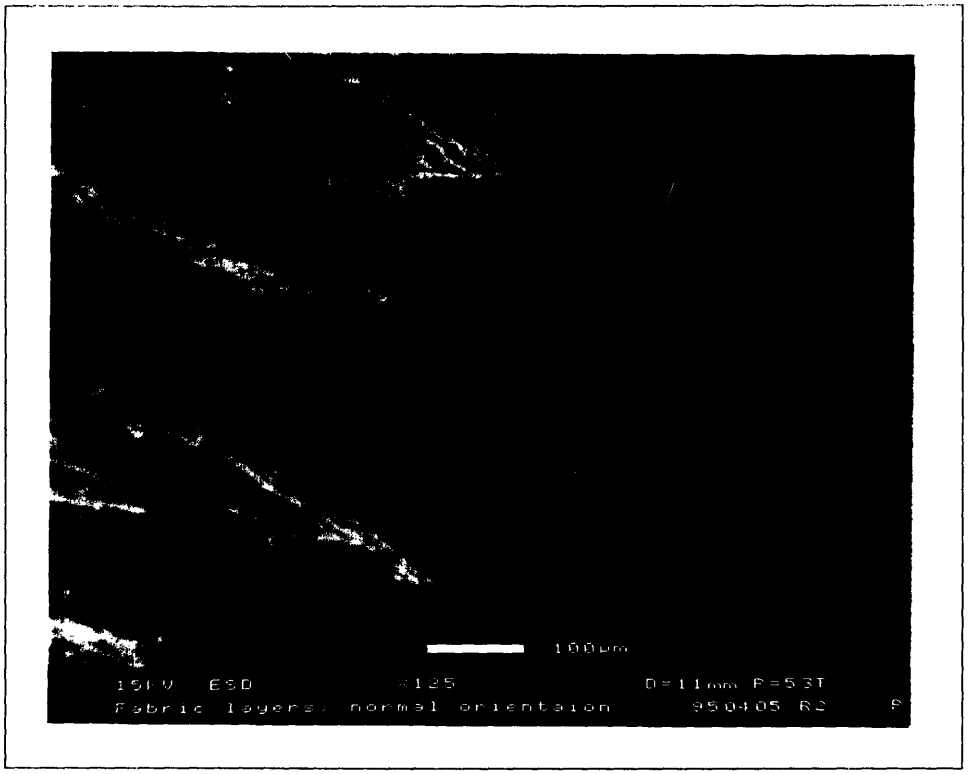

Figure 4-17: Specimen fractured normal to layers of fabric, T_{mold} = 159°C, 125X.

ing. No difference was observed between the flycut surfaces of irradiated and unirradiated UHMWPE. Figure 4-19 and Figure 4-20 are of unirradiated samples of UHMWPE corresponding to sliding distances of 14747.4 m, and 29494.9 m respectively. Clearly much more damage has occurred to the surface in the latter of the two cases. In Figure 4-19 some of the machining marks are still visible. The important feature of these two figures is the distinct pattern of cracks which are visible. These dark areas appear to be tears at the surface which have occurred as a result of the high traction force exerted on the surface of the polyethylene by the CoCr slider. Furthermore, these cracks appear to be about 20 μm in length by about 3-6 μm in width.

Figure 4-22 shows that the 2.5 MRad irradiated specimen also exhibits these surface features at a sliding distance of 29494.9 m. However, if we directly compare Figure 4-20 of the unirradiated sample to Figure 4-22 of the irradiated sample we can see that the quantity of these cracks is higher (greater density) and in addition the cracks have lengths in excess of 40 μm and in many cases have joined to form cracks with lengths up to 100 μm. This evidence of greater surface damage may point to some of the effects of irradiation treatment, namely increased brittleness which would make the material more susceptible to crack formation and propagation as a result of a decrease in ductility.

Another focus of the ESEM examination of the wear tracks concerns the high tensile stresses developed at the surface which cause cracks to form behind the slider as it moves over the surface. Section 5.4 on the contact mechanics of the sliding cylinder discussed the high stresses present at the edges of the slider. It would be expected that in these areas where the stress exceeds the yield stress of UHMWPE that increased surface damage would be visible, and examining Figure 4-24 this is indeed what is observed. This ESEM micrograph is of the same sample in Figure 4-19 however the difference being that it is taken at the edge. There is a large amount of damage in this localized region spanning about 200 μm in width. It should be pointed out that this micrograph was taken at

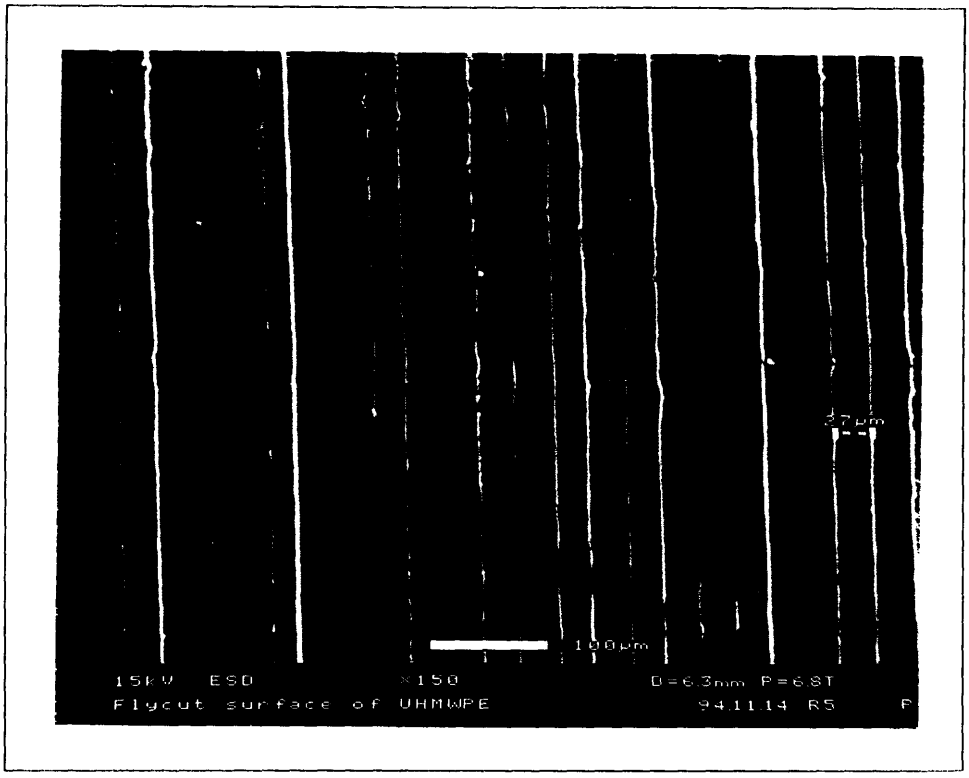

Figure 4-18: Flycut surface of UHMWPE

a magnification of 150x whereas all of the previous micrographs were at 500x. Furthermore, this extensive localized damage has occurred within just the first 14200 m slid alone.

4.5.2 ESEM Examination of Worn Counterfaces

In addition to the examination of worn polyethylene surface, the corresponding metallic counterfaces were also examined for signs of change. Throughout testing, metallic counterfaces of SS304 and CoCr were used. All counterfaces were polished to a finish of $R_a \approx 0.1$ μm as measured by the technique discussed in Section 4.7.1. It should be noted that a comparison between the wear of SS304 sliders and CoCr is not intended here. Such a comparison requires systematic examination of surfaces after all tests. Instead the purpose of these observations was to simply learn and observe the changes if any that occur on the surface of the metallic counterface.

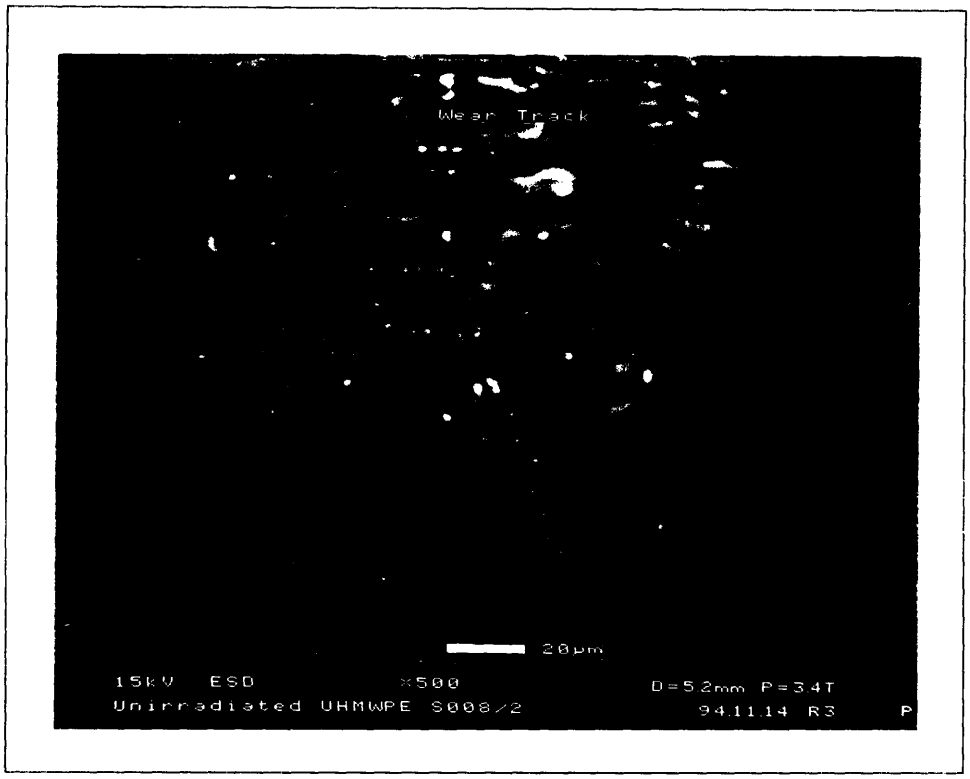

Figure 4-19: Unirradiated UHMWPE at 14747.4 m slid

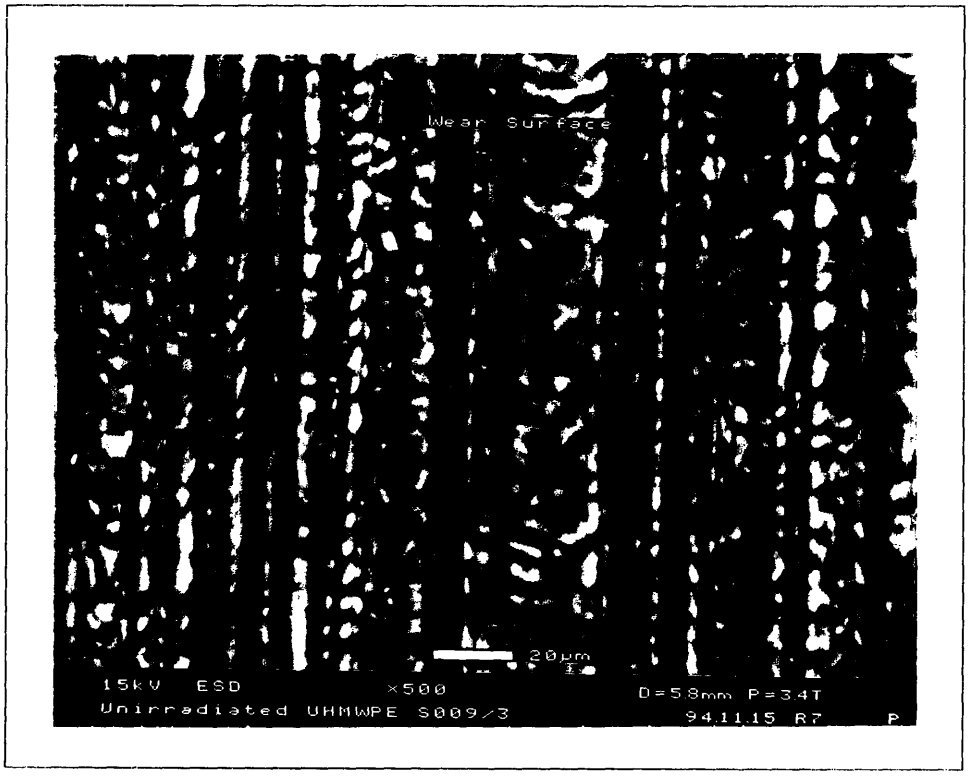

Figure 4-20: Unirradiated UHMWPE at 29494.9 m slid

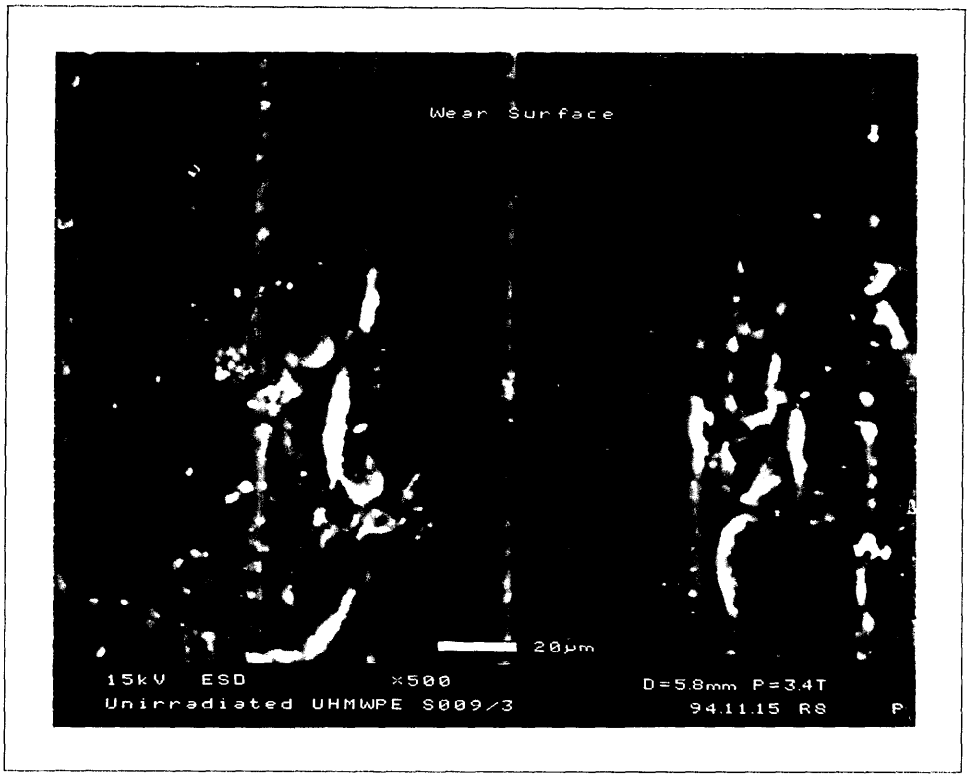

Figure 4-21: Irradiated UHMWPE at 14747.4 m slid

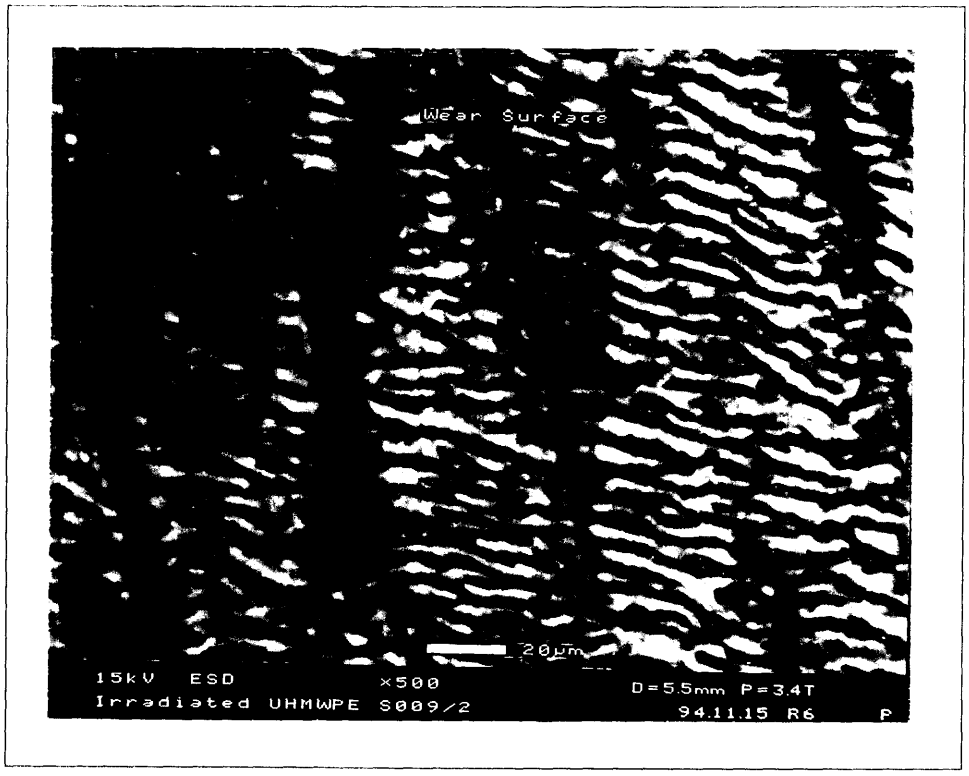

Figure 4-22: Irradiated UHMWPE at 29494.9 m slid

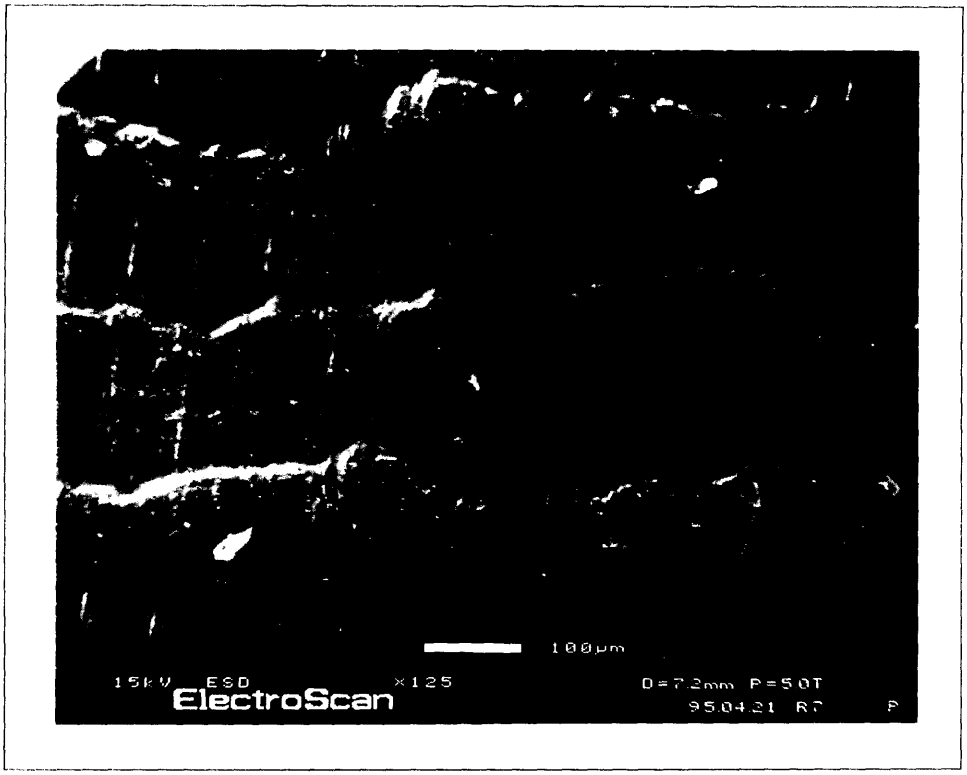

Figure 4-23: Homocomposite at 29494.9 m slid

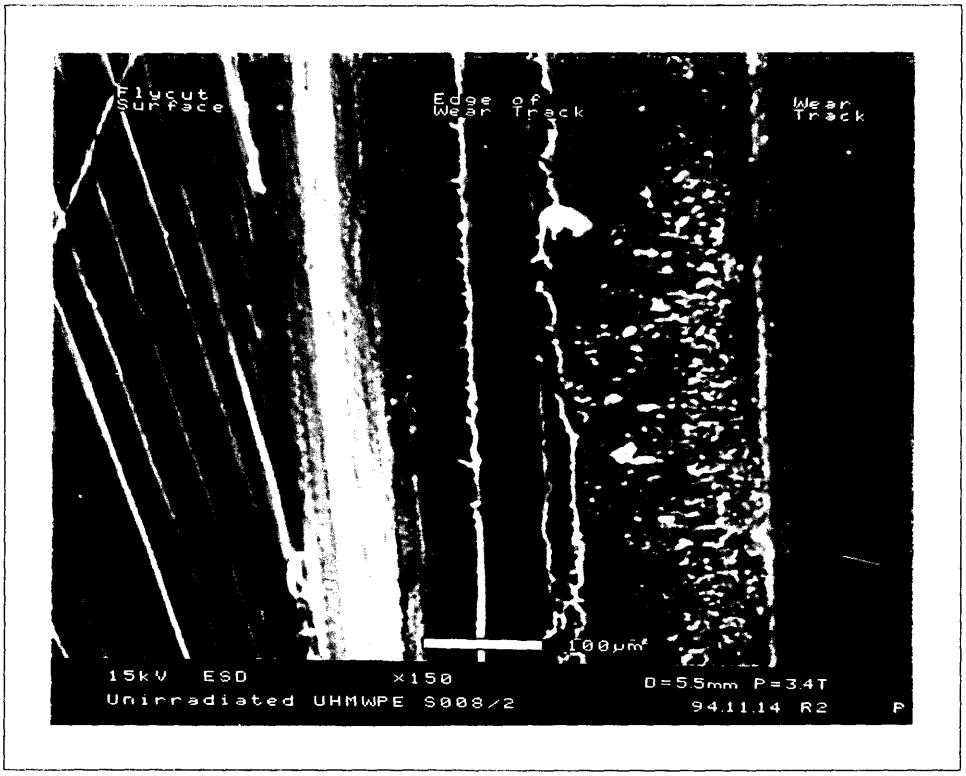

Figure 4-24: Edge of a wear track of worn UHMWPE

Figure 4-25 shows the polished surface of a CoCr sample prior to wear testing. The fine lines ($\leq$ 1 μm) visible at regular intervals are the result of the polishing process. The counterfaces of two different sliders of SS304 and CoCr were examined after 29494.9 m slid and are shown in Figure 4-26 and Figure 4-27. Figure 4-26 is of a CoCr slider which had been worn for 29494.9 m slid against a sample of 2.5 MRad irradiated UHMWPE that had been used with bovine serum as the lubricant. The micrograph has been taken at a magnification of 83x to show the full area that has been worn. Since, the full length of the worn area cannot be shown a split image was taken. The area of wear shown is approximately 2000 μm in length by 600 μm in width. This micrograph shows polyethylene which has been transferred to the counterface as evidenced by the aligned charged areas in the direction of sliding. From this image the contact area can be determined to be approximately 2000 μm x 1.6 cm (thickness of the cylindrical slider).

Figure 4-27 of a SS304 slider is also for 29494.9 m slid. At a higher magnification of 900x, the area in the center is of a very thin layer of polyethylene since areas showing the polishing process are still visible running through the polyethylene areas. This particular SS304 slider was also tested for 29494.9 m cycles against unirradiated UHMWPE under bovine lubricated conditions.

In summary, there was no significant difference in the wear behavior of the metallic counterfaces with respect to the irradiation or unirradiated cases, suggesting that structural changes in the UHMWPE cannot be detected by observing the worn surface of the metallic counterface alone.

4.6 Differential Scanning Calorimetry

Section 3.5.3 dealt with the effects of irradiation on UHMWPE. One of the ways to characterize these effects is to perform Differential Scanning Calorimetry (DSC) on a specimen which has been exposed to irradiation. DSC is an

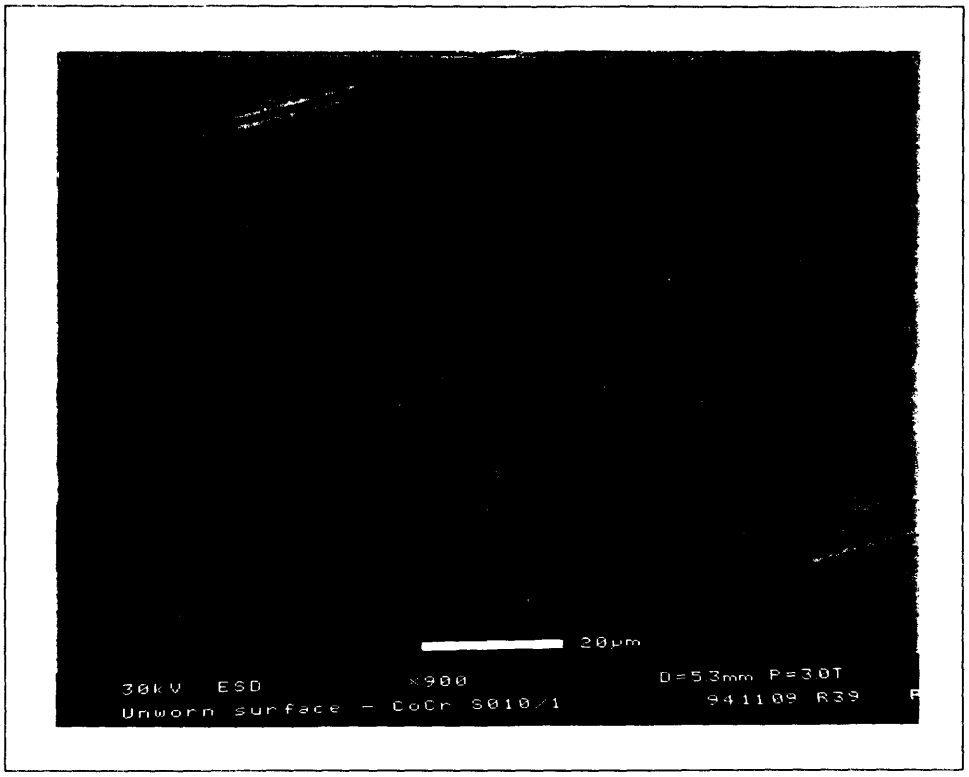

Figure 4-25: Polished surface of a CoCr slider

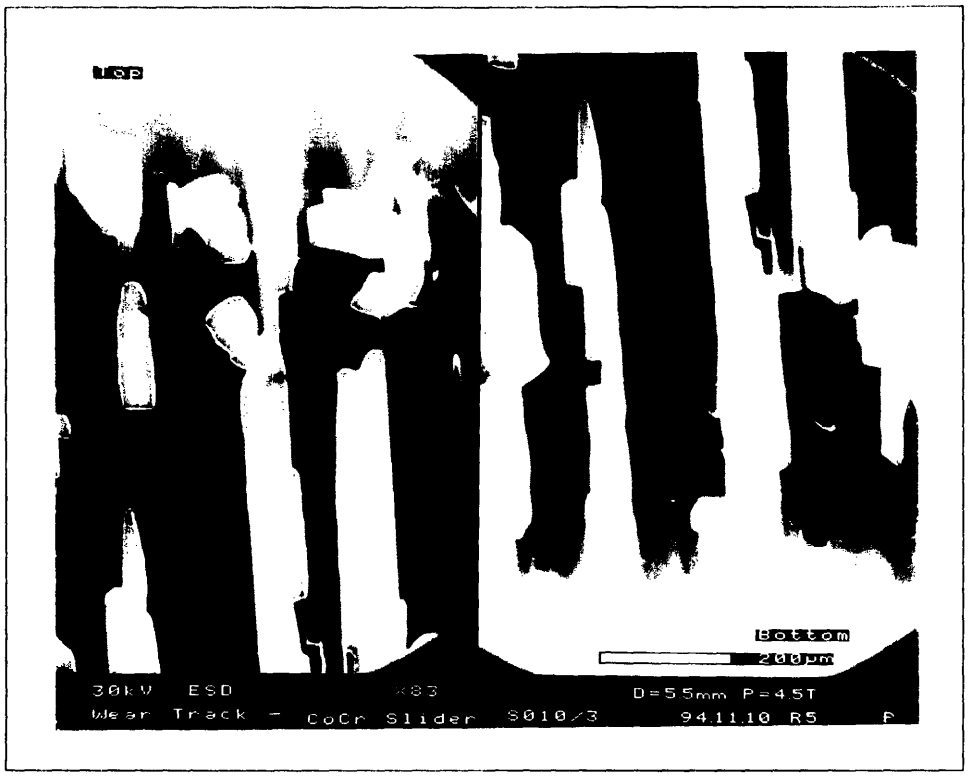

Figure 4-26: Worn surface of a CoCr slider after 29494.9 m slid

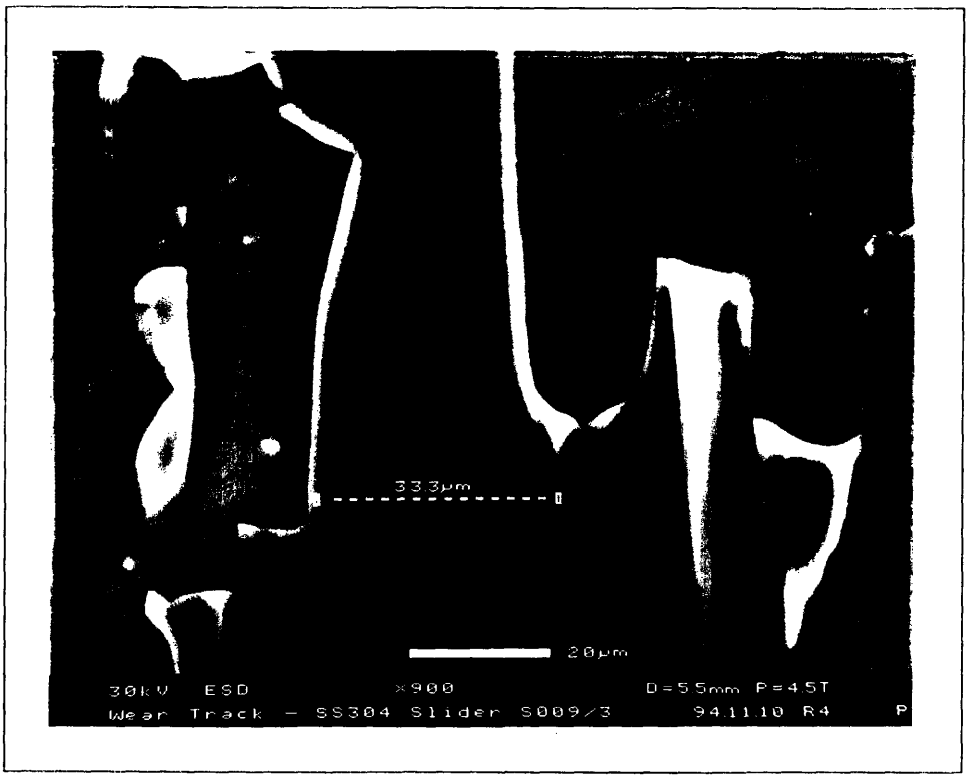

Figure 4-27: Worn surface of a SS304 slider after 29494.9 m slid

effective tool for measuring changes which occur in the melting point of materials which have been irradiated. In this work, DSC was used to provide insight into melt processing of the homocomposite. Knowledge of the melting point of the reinforcing fibers in the homocomposite permits tighter control on the temperature molding conditions.

Background on DSC

When a material goes through a phase change, there is either a release or absorption of energy. A differential scanning calorimeter is able to measure the enthalpy of such a transition by measuring the differential heat flow required to maintain a sample of the material and an inert reference at the same temperature as the two are heated. By scanning over a specific temperature range and thus producing a thermogram, the DSC produces a curve of the heat input as a function of temperature. On this curve there is a peak, or maximum at the

point at which a phase change occurs. This peak is the melting point of the material[6].

4.6.1 DSC of Irradiated Spectra Fabric

As was stated above, knowledge of the melting point of the reinforcing fibers used in the manufacture of homocomposites is necessary in order to select a molding temperature to ensure the matrix resin UHMWPE GUR 4150 melts and the fibers do not. To determine these melting points, Spectra fabrics used in the manufacture of the homocomposites were irradiated in air and in vacuum at different levels and their melting points subsequently measured. In addition, samples of UHMWPE were also measured.

Figure 4-28 shows a compilation of the melting point data obtained from these measurements. Three actual DSC plots were selected and plotted as obtained directly from the instrument[7], these curves are shown in Figure 4-29. The first feature noticed in both of these figures is the existence of two melting peaks of the fabrics for all of the irradiated levels. Similar phenomena has been observed by other researchers. Song and Ehrenstein [61] attribute the second higher melting peak as an increase in the number of thermally stable crystalline structures. According to Song and Ehrenstein [61], the formation of thermally stable crystalline structures in the fibers is not uniformly distributed over the cross section of the fibers. In other words, there is a variation in the crystallinity of the fibers as a function of the radius as a result of processing of the fibers.

In Figure 4-29 as the irradiation level increases, the two peaks become less distinct. This indicates the effect which irradiation may be having on the crystallinity of the fibers. Furthermore, Figure 4-28 shows a slight decrease in the melting point of both peaks as a function of increasing irradiation level.

[6]DSC analysis performed in this work was calibrated with a sample of Indium prior to all measurements

[7]Perkin-Elmer DSC-2

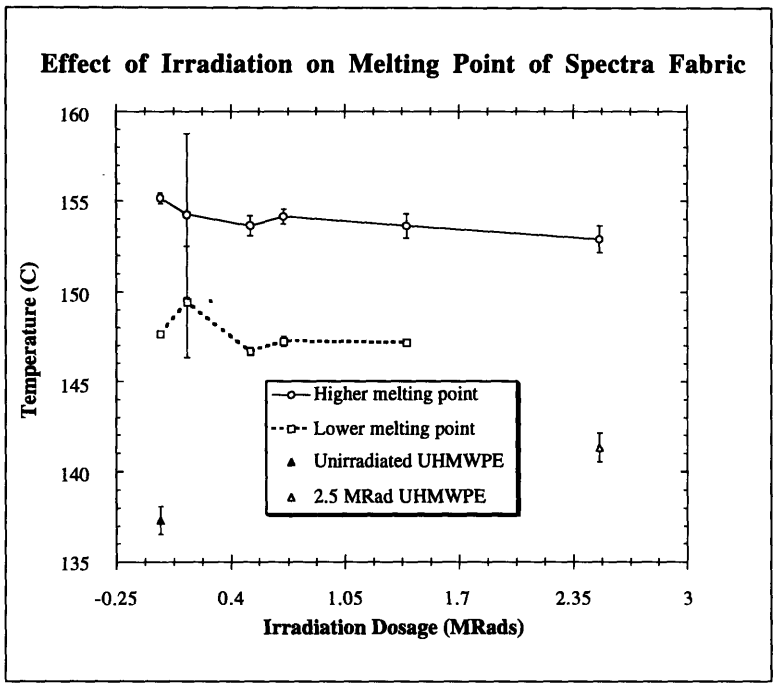

Figure 4-28: DSC analysis of melting points of irradiated fabrics

The more important observation here is that the melting point of the fabric is above that of the UHMWPE which has a melting point of approximately 137^oC. This indicates that there is about an 8 to 10 degree process window for the homocomposite where the fiber phase will not melt and the matrix phase will.

4.6.2 DSC of Air and Vacuum Irradiated Spectra Fabric

A study was undertaken to determine the potential benefits of vacuum irradiation in order to improve the process window for molding of the homocomposite. Samples of fabric received dosages of 2.5 and 5.0 MRads in an air environment as well as in high vacuum. The melting point data is summarized in Figure 4-30 with the corresponding DSC curves plotted for the 2.5 MRad level in Figure 4-31. The melting point data in Figure 4-30 shows that as the irradiation level is increased for vacuum-specimens the melting points hold constant whereas the

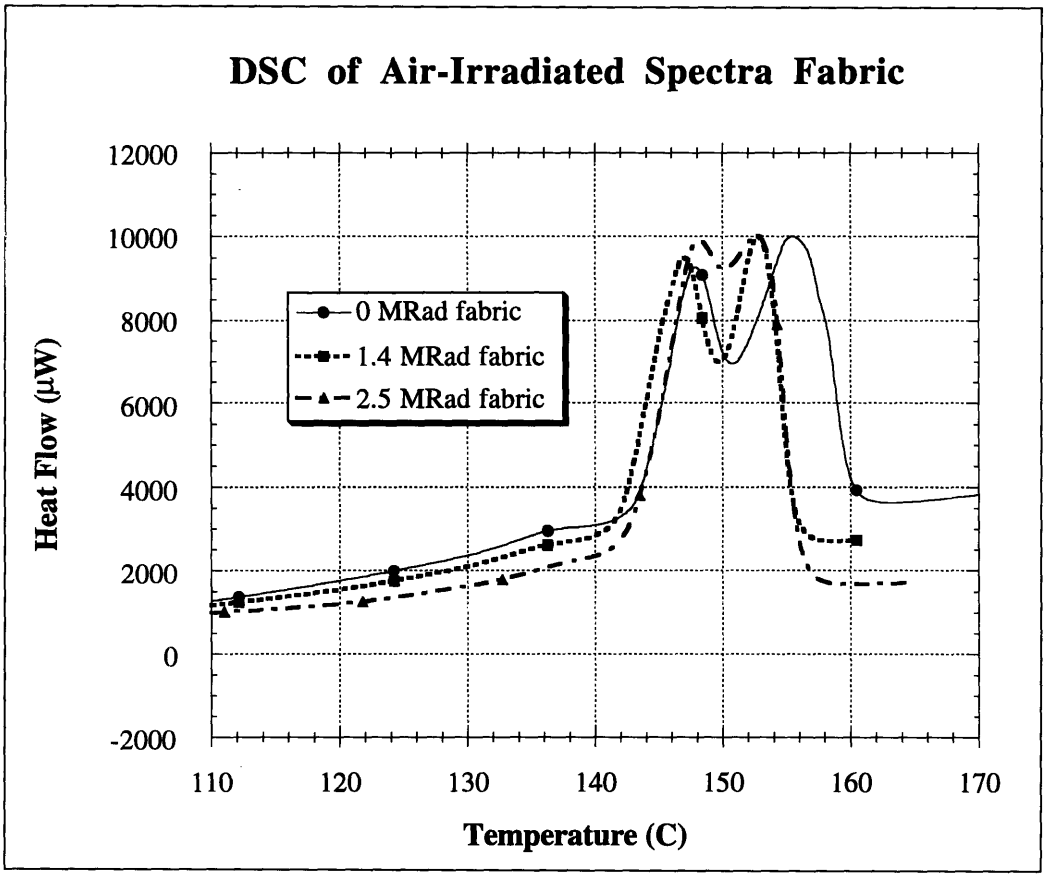

Figure 4-29: DSC analysis of melting points from selected irradiated fabrics

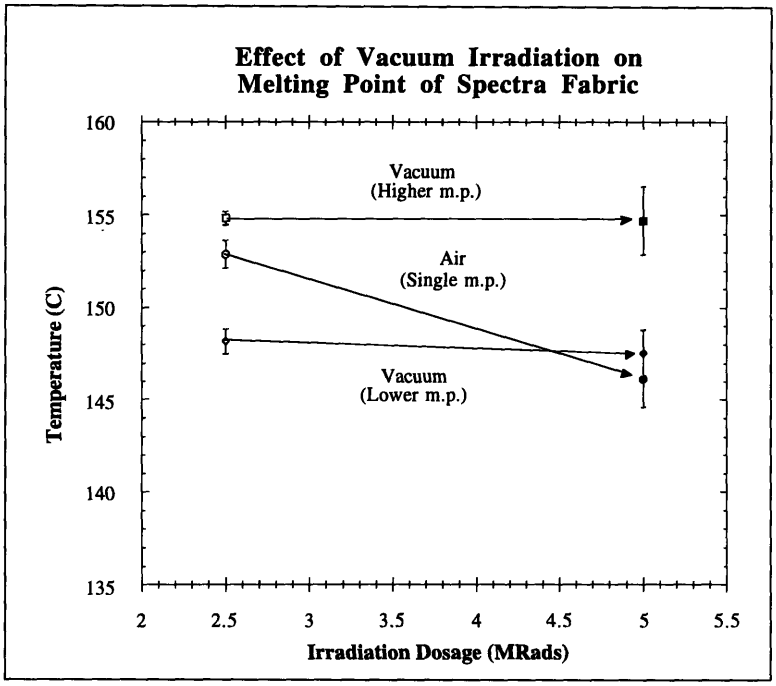

Figure 4-30: DSC melting points of fabric irradiated in air and vacuum

melting points of the air-specimens decrease. Furthermore, in Figure 4-31 at an irradiation level of 2.5 MRad, the vacuum-specimens retained the distinct double peak whereas melting peak(s) for the air-specimens became less distinct compared to the unirradiated specimens. No measurements were performed at intermediate irradiation levels other than 2.5 and 5 MRad, so it is difficult to identify a trend. However, it appears that vacuum-irradiated specimens do not undergo the same changes which specimens that are irradiated in air undergo.

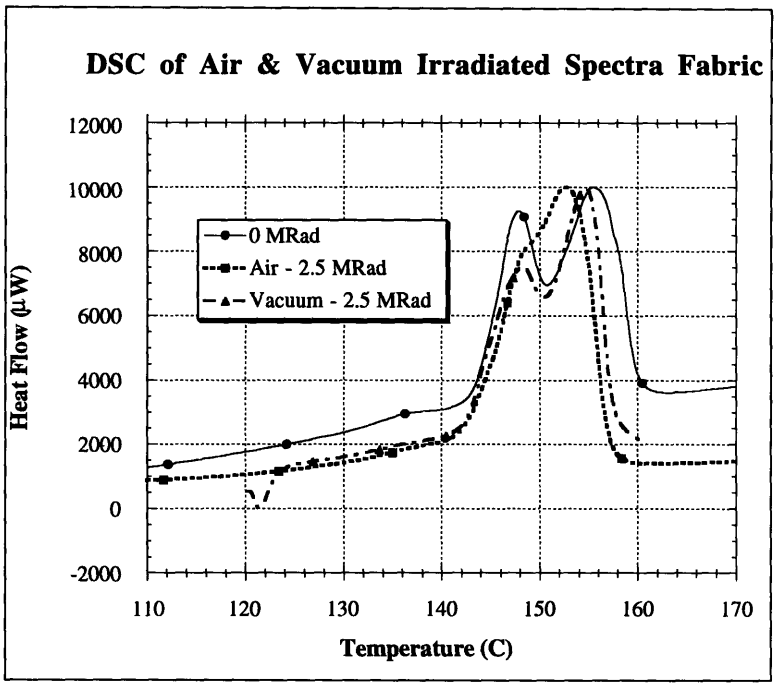

Figure 4-31: DSC melting curves of fabric irradiated in air and vacuum

4.7 Profilometry of Wear Tested Surfaces

4.7.1 Introduction

In general sliding situations, surfaces change as the distance slid increases. In some cases, the changes that occur in surface topography is a good indication of the wear process occurring between the sliding pairs. For example, in Section 2.3 concerning delamination wear theory, the earliest event which occurs is the deformation and fracture of asperities of the softer surface leaving behind a relatively smooth surface. Such changes in surface topography can be analyzed qualitatively using visual techniques such as optical and scanning electron microscopy. However, to quantitatively assess the wear occurring in a sliding system by examination of surface topography, a device such as a profilometer must be used. A profilometer is an electromechanical system capable of measuring surface features characteristic of engineering surfaces.

To understand the wear process occurring between UHMWPE/homocomposites

and CoCr (and SS304) the polyethylene surfaces and counterfaces were characterized using profilometry as a function of distance slid. In addition, profilometry was used to measure the volume of wear at specific intervals of 7373.7 m, 14747.4 m, and 29494.9 m slid by the method described in Section 4.3.2.

4.7.2 Contact Profilometry

All profilometry was performed using a Dektak 8000 profilometer. The Dektak 8000 measures surface features by moving the sample material underneath a diamond-tipped stylus having a radius of 2.5 μm. This is a contact method of profilometry since the stylus which makes physical contact with the surface is mechanically coupled to the core of an LVDT. As the stylus moves over surface features, the LVDT produces analog signals which are conditioned and converted to digital signals by electronic circuitry and processed by the host computer. As described previously in Section 4.3.2, the Dektak 8000 can be programed to automatically scan specified areas of a surface and calculate desired quantities. Other features of the Dektak 8000 that were made use of are the large vertical range of 2620 k$\mathring{A}$ and the programmable stylus tracking force (1-100mg).

4.7.3 Profilometry of Worn UHMWPE and Homocomposite Surfaces

The profilometry scans of UHMWPE and homocomposite wear surfaces are shown in Figure 4-32, Figures A to D. To establish a reference, an untested, flycut sample of UHMWPE shown in Figure A was scanned yielding an R_a = 0.356 μm. The scan of this untested sample serves as a control to ensure that Figures B to D are indeed of wear tracks. Some relative comparisons may be immediately made. First, the irradiated sample of UHMWPE showed the highest roughness of the three with $R_a = 0.908\ \mu m$, compared to $R_a = 0.716\ \mu m$

for the homocomposite and $R_a = 0.605\ \mu m$ for the unirradiated UHMWPE. The fact that the irradiated UHMWPE had the highest roughness may be explained by the removal of asperities which occurs in a brittle fashion leading to a rougher surface instead of a smoother one. This difference is best seen by comparing Figure B and Figure C. The homocomposite in Figure D gave an intermediate value of $R_a = 0.716\ \mu m$ and its roughness can be attributed to the different surface properties of the fiber and matrix phases.

A final point which merits discussion is the raised edge followed by a 'deep valley' in the wear track present in all three figures B,C, and D. Two possible reasons explain these features. First, the surface profile is greatly enhanced in the z- direction with respect to the horizontal scan length, so these apparently sharp peaks in reality are not so sharp. In Section 4.3.2 it was briefly mentioned that the alignment of the axis of the counterface with respect to the sliding direction has a tolerance of approximately +/- 0.005" or +/- 125 μm. Examining all three figures, this value of +/- 125 μm is a good approximation to the 'width' of the valley at different depths. Furthermore, the valley at the edge of the wear track coincides with the location of the high stress concentration that was discussed in the analysis of subsurface stresses in Section 5.1.

4.7.4 Profilometry of Worn CoCr Surfaces

For every UHMWPE and homocomposite surface which was scanned, the corresponding CoCr counterface was also scanned. The scanning of the polyethylene surfaces is relatively straight forward and only involves scans across the wear track. However, the scanning of the counterfaces is not trivial and deserves discussion. Scanning of the surface of CoCr cylindrical counterfaces was done parallel to the longitudinal axis of the cylinder. The problem which exists in scanning this surface is the difficulty in being able to scan along the centerline of this axis. Being too far away from this line leads to inaccurate scans. To ensure that scans were being taken as close as possible to this optimum scan

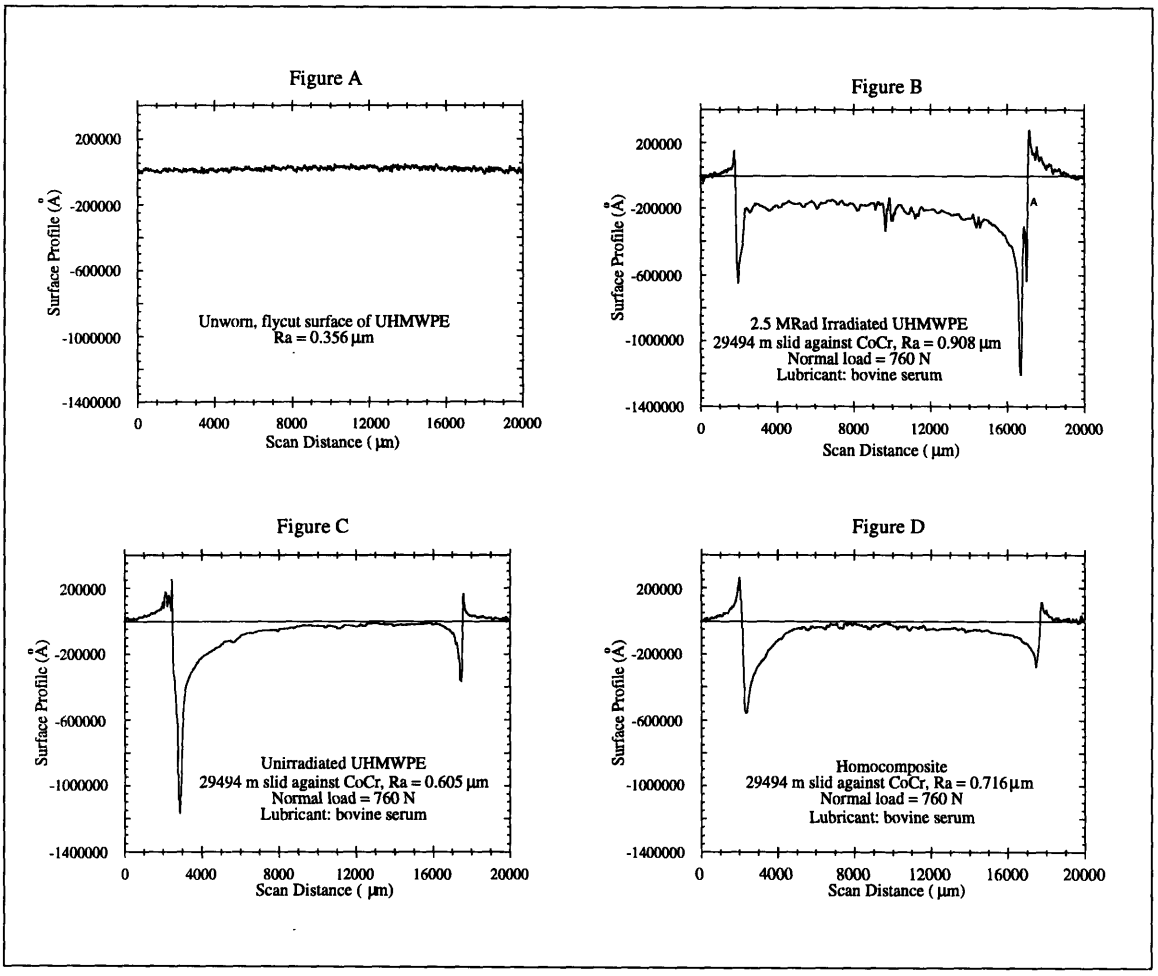

Figure 4-32: Profilometry of worn UHMWPE and homocomposite surfaces

path, trial scans were taken in the perpendicular direction to find the "high point" of the cylinder. This led to good repeatability in scanning as exhibited in the standard deviations in Figure 4-33.

Figure 4-33 summarizes the profilometry performed on CoCr counterfaces of which some of these scans are shown in Figure 4-34, Figures A to C. Figure 4-33 shows that over the first 30,000 m slid, the roughness of the counterface increases linearly. Then over the next 60,000 m slid, the roughness reaches a constant value. The first question which must be answered when interpreting this data is: How and Why does the roughness of the hard counterface increase? The answer to this question may be found by considering the mechanical effects of the plowing of the soft polyethylene by the hard asperities of the counterface. In other words, the roughness of the counterfaces seemingly increases not because the metal is worn away but rather because polyethylene wear particles are entrapped in the asperities of the counterface. Hence, the roughness appears to increase because the 2 μm stylus scans over polyethylene which has agglomerated in the asperities of the counterface. This is supported by the ESEM evidence of polyethylene seen in the micrograph of the tested CoCr surface in Figure 4-26.

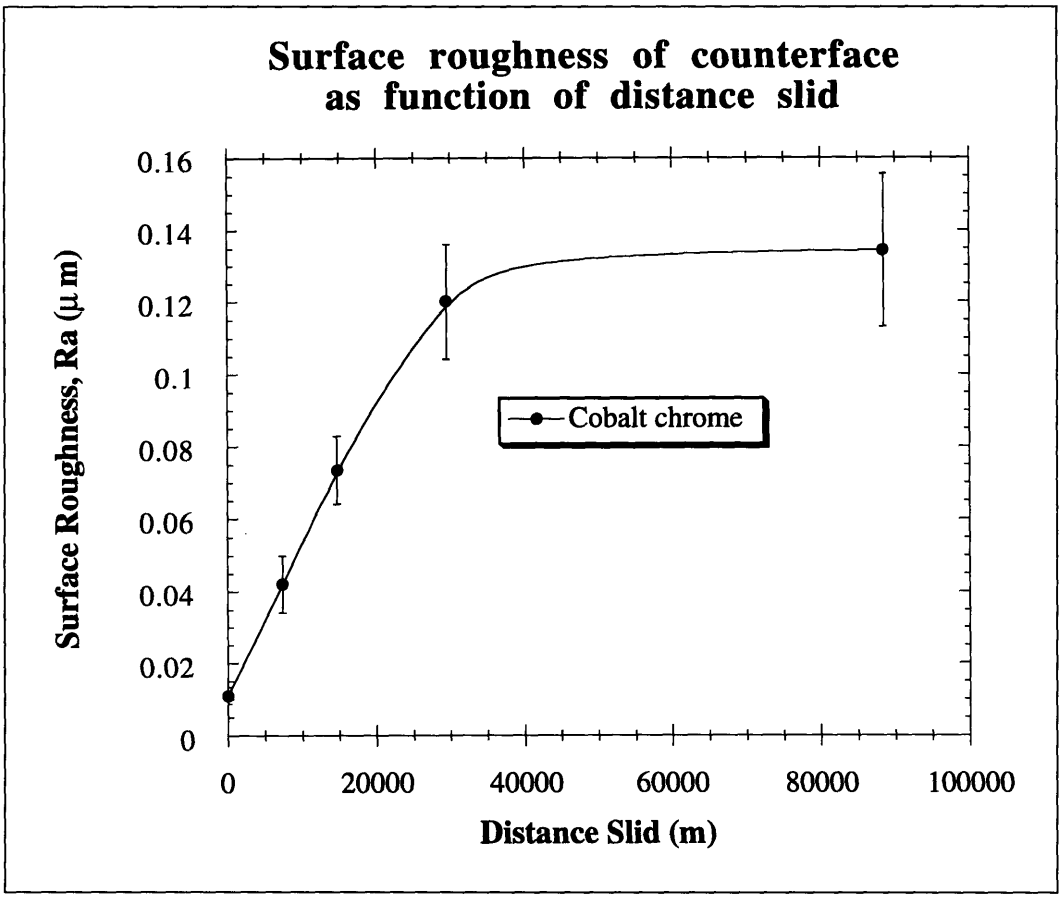

Figure 4-33: Surface roughness of cobalt chrome counterfaces

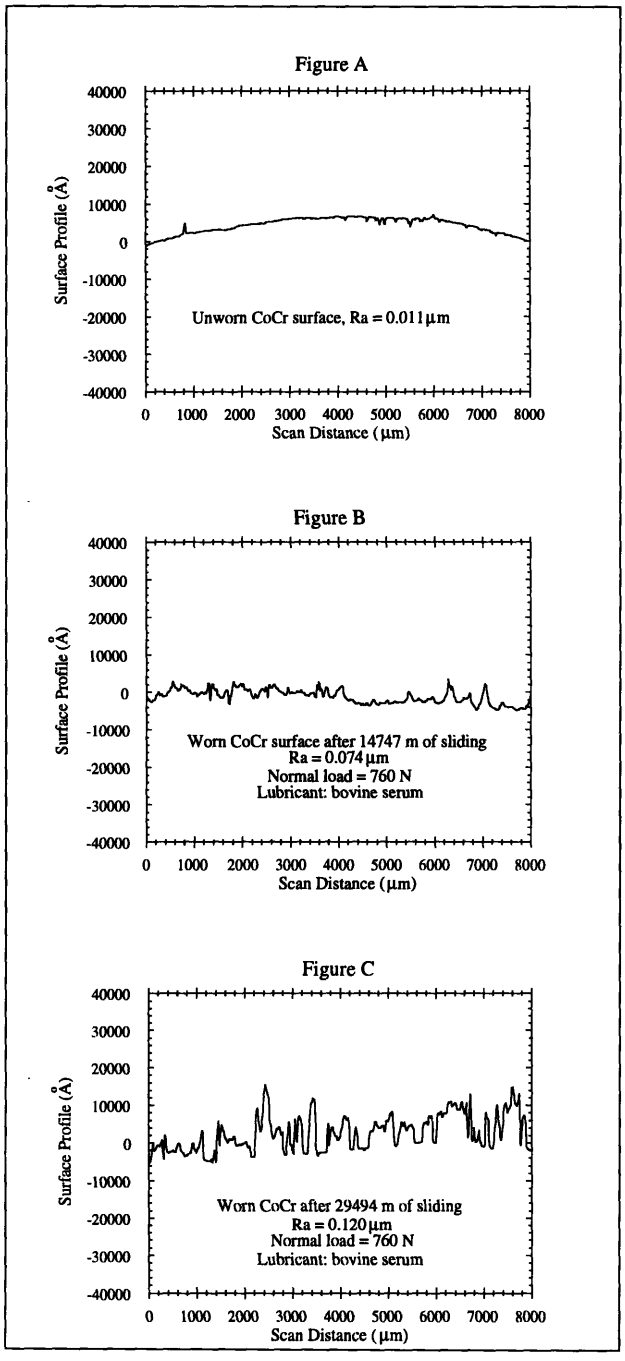

Figure 4-34: Profilometry of surfaces of CoCr

Chapter 5

Mechanical Behavior of the Sliding Interface

Chapter 2 discussed the importance of the plastic deformation of the surface and subsurface which precedes the wear failure of UHMWPE. This chapter reviews the contact stresses which arise in the wear tests conducted in this work and how they can lead to plastic deformation of the surface and subsurface.

5.1 Nonconformal contacting surfaces

Hertzian contact theory is limited to frictionless surfaces and perfectly elastic solids, and as a result certain assumptions have to be made about the bodies in contact. First, the contact area is small relative to the bodies themselves. For this reason the stresses are localized and can be considered stress concentrations. If the two bodies are conformal, the contacting surfaces are comparable to the bodies themselves; hence, the contact stresses become part of the overall stress distribution throughout the bodies. Johnson [34] defines conformal contact as two bodies whose surfaces 'fit' exactly or closely together without deformation and nonconformal contact as bodies having dissimilar profiles. Such nonconfor-

mal surfaces when initially brought into contact make contact either at a point or along a line. A sphere-on-flat or sphere-on-sphere make point contacts. A cylinder-on-flat as is the case with the geometry of the wear tester used in this work makes line contact. This line contact results because the cylinders have profiles which conform in one direction and do not conform in the *perpendicular* direction.

5.2 Stress distribution - uniform pressure

This section concerns the development of the relationships for the stress distribution which arise from the application of a uniform pressure. The cylindrical slider may be thought of as applying such a constant distributed load when viewed normal to the sliding direction. This orientation is best illustrated in the end view shown in Figure 5-4. The following derivation uses the concept of the elastic half-space to obtain this stress field.

To apply elasticity (linear small strain theory) it must be assumed that the two bodies contact each other over an area whose dimensions are small compared with the radii of curvature of the undeformed surfaces [34]. If it is assumed also that the size of the bodies is large in comparison to the size of the contact area, then the stresses in the contact region are not strongly influenced by the shape of the bodies far from the contact region. Johnson [34] defines an elastic half-space by considering each body as a semi-infinite elastic solid bounded by a plane surface. This simplifies boundary conditions greatly (see Figure 5-1). This model is used commonly in elastic contact stress theory to find the stress field σ_x, σ_z, and τ_{xz} and the displacements u_x, u_z in the body from its initial undeformed state. To solve for these quantities the following series of equations must be used.

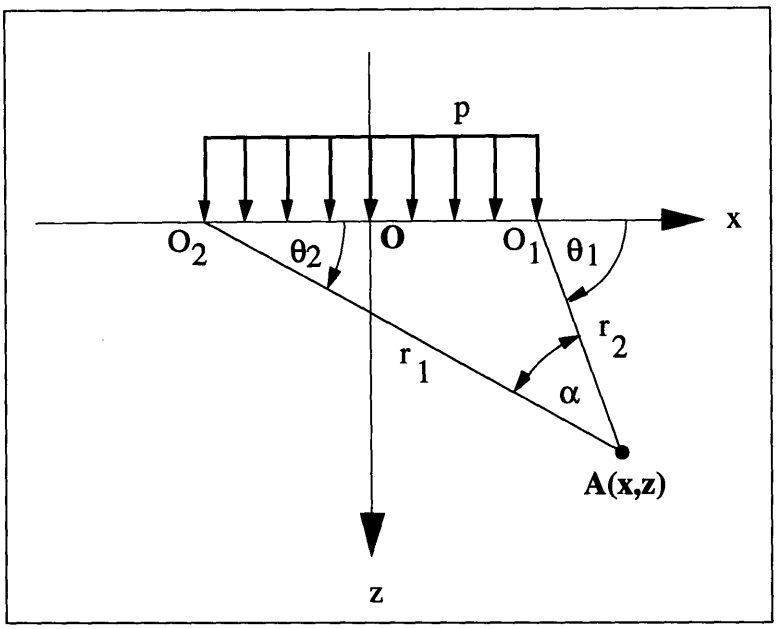

Figure 5-1: Elastic half space used in analysis [34]

Two-dimensional equilibrium must be satisfied:

$$\left.\begin{aligned} \frac{\partial \sigma_x}{\partial x} + \frac{\partial \tau_{xz}}{\partial z} &= 0 \\ \frac{\partial \sigma_z}{\partial z} + \frac{\partial \tau_{xz}}{\partial x} &= 0 \end{aligned}\right\} \tag{5.1}$$

Compatibility requirements must also be fulfilled:

$$\frac{\partial^2 \epsilon_x}{\partial z^2} + \frac{\partial^2 \epsilon_z}{\partial x^2} = \frac{\partial^2 \gamma_{xz}}{\partial x \partial z} \tag{5.2}$$

The corresponding strain-displacement relations are:

$$\left.\epsilon_x = \frac{\partial u_x}{\partial x}, \quad \epsilon_z = \frac{\partial u_z}{\partial z}, \quad \gamma_{xz} = \frac{\partial u_x}{\partial x} + \frac{\partial u_z}{\partial z}\right\} \tag{5.3}$$

In assuming plane strain conditions, it is assumed that the thickness of the body is large compared with the width of the load region:

$$\left.\begin{aligned} \epsilon_y &= 0 \\ \sigma_y &= \nu(\sigma_x + \sigma_y) \end{aligned}\right\} \tag{5.4}$$

Thus Hooke's Law becomes:

$$\left.\begin{aligned} \epsilon_x &= \tfrac{1}{E}[(1-\nu^2)\sigma_x - \nu(1+\nu)\sigma_z] \\ \epsilon_z &= \tfrac{1}{E}[(1-\nu^2)\sigma_z - \nu(1+\nu)\sigma_x] \\ \gamma_{xz} &= [\tfrac{2(1+\nu)}{E}]\tau_{xz} \end{aligned}\right\} \tag{5.5}$$

A stress function $\phi(x,z)$ can be defined such that:

$$\left.\sigma_x = \tfrac{\partial^2\phi}{\partial z^2}, \quad \sigma_z = \tfrac{\partial^2\phi}{\partial x^2}, \quad \tau_{xz} = -\tfrac{\partial^2\phi}{\partial x \partial z}\right\} \tag{5.6}$$

Equations 5.1,5.2, and 5.5 will be satisfied if $\phi(x,z)$ satisfies the biharmonic equation:

$$\left(\tfrac{\partial^2}{\partial x^2} + \tfrac{\partial^2}{\partial z^2}\right)\left(\tfrac{\partial^2\phi}{\partial x^2} + \tfrac{\partial^2\phi}{\partial z^2}\right) = 0 \tag{5.7}$$

with B.C.'s:

$$\left.\begin{aligned} \sigma_x(x, z=0) &= 0 \quad for \quad x < -b \; or \; x > +a \\ \tau_{xz}(x, z=0) &= 0 \end{aligned}\right] \tag{5.8}$$

$$\left.\begin{aligned} \sigma_x(x, z=0) &= -p(x) \quad for \quad -b \leq x \leq a \\ \tau_{xz}(x, z=0) &= -q(x) \end{aligned}\right] \tag{5.9}$$

$$\left.\begin{aligned} \sigma_x(x, z) &= 0 \quad for \quad x \to \pm\infty \; and \; z \to +\infty \\ \sigma_z(x, z) &= 0 \\ \tau_{xz}(x, z) &= 0 \end{aligned}\right] \tag{5.10}$$

To find the solution two of the following four quantities must be known: $p(x), q(x), u_x(x, z =$

0), or $u_z(x, z = 0)$. By specifying $p(x)$ to be constant and $q(x) = 0$, the stress distribution due to a uniform normal pressure[34] is obtained:

$$\left.\begin{aligned} \sigma_x(x,z) &= -\tfrac{p}{2\pi}[2(\theta_1-\theta_2)-(\sin 2\theta_1-\sin 2\theta_2)] \\ \sigma_z(x,z) &= -\tfrac{p}{2\pi}[2(\theta_1-\theta_2)+(\sin 2\theta_1-\sin 2\theta_2)] \\ \tau_{xz}(x,z) &= -\tfrac{p}{2\pi}(\cos 2\theta_1-\cos 2\theta_2) \end{aligned}\right\} \tag{5.11}$$

where

$$\tan\theta_{1,2} = \frac{z}{x \mp a} \tag{5.12}$$

and

$$\alpha = \theta_1 - \theta_2 \tag{5.13}$$

so that the principal stresses can be calculated according to:

$$\left.\begin{aligned} \sigma_{1,2} &= -\tfrac{p}{\pi}(\alpha \mp \sin\alpha) \\ \tau_1 &= \tfrac{p}{\pi}\sin\alpha \end{aligned}\right\} \tag{5.14}$$

Note that a maximum shearing stress of $\tau_1 \mid_{max} = \frac{p}{\pi}$ occurs at $\alpha = \frac{\pi}{2}$.

5.3 Stress distribution - cylinder-on-flat contact

This section treats the two types of two-dimensional stress distributions for a cylinder-on-flat contact. The first section considers only the effect of the normal load, while the following section the considers both the effects of a normal as well as a frictional force. Furthermore, both sections contain plots of data for the loading conditions found in the wear tests described in Chapter 4.

5.3.1 Hertzian Contact Stresses

Stachowiak and Batchelor [62] consider the cylinder-on-flat geometry and derive the following equations to determine the maximum Hertzian pressure as well as the formula for the maximum shear stress.

The contact area of the cylinder-on-flat is rectangular in shape and has dimensions $2l$ by $2b$. The thickness of the cylinder is the dimension $2l$, and the contact width $2b$ is given by:

$$b = \sqrt{\frac{4PR'}{\pi l E'}} \tag{5.15}$$

R' and E' are the reduced radius and reduced stiffness respectively and may be calculated using the following relations:

$$\frac{1}{R'} = \frac{1}{R_{cylinder}} + \frac{1}{R_{flat}} \tag{5.16}$$

where $R_{flat} \rightarrow \infty$

$$\frac{1}{E'} = \frac{1}{2}[\frac{1-\nu^2_{cylinder}}{E_{cylinder}} + \frac{1-\nu^2_{flat}}{E_{flat}}] \tag{5.17}$$

The maximum Hertzian pressure which is based on an elliptical pressure distribution is:

$$P_{max} = \frac{P}{\pi b l} \tag{5.18}$$

and the average pressure is simply the applied load acting on the apparent contact area b x l:

$$P_{average} = \frac{P}{4bl} \tag{5.19}$$

The maximum shear stress τ_{max}:

$$\tau_{max} = 0.304 P_{max} \tag{5.20}$$

occurs at depth given by:

$$z = 0.786b \tag{5.21}$$

Equations 5.18, 5.19, and 5.20 were used to generate the curves in Figure 5-2. All three curves were obtained for the case of a CoCr cylinder applying a load to a flat surface of UHMWPE. This is the geometry used in the friction and wear tests discussed in Chapter 4. Values of P_{max}, P_{avg}, and τ_{max} were calculated for loads ranging from 100 N to 1000 N. Furthermore, a vertical line is drawn at an applied load of approximately 760 N which is the load that was used in all friction and wear experiments. At this load of 760 N the P_{max} and the P_{avg} exceed the yield strength σ_y of UHMWPE (horizontal line in Figure 5-2). Also at this load, the maximum shear stress calculated is greater than that of 5.20 for UHMWPE (lower horizontal line in Figure 5-2).

5.3.2 Hertzian Contact Stresses with friction

This section considers the effect of friction on the stress field below the slider. The following expressions for $\sigma_x, \sigma_z, and\ \tau_{xz}$ can be found in Suh [74] and are derived using the elastic half-space in Figure 5-1:

The surface tractions are assumed to be distributed elliptically in accordance with Hertzian contact stress theory such that:

$$p(x) = \begin{cases} 0 & for \quad \mid x \mid > a \\ -p_o\sqrt{1-(x/a)^2} & for \quad \mid x \mid \leq a \end{cases} \tag{5.22}$$

$$q(x) = \begin{cases} 0 & for \quad \mid x \mid > a \\ q_o\sqrt{1-(x/a)^2} & for \quad \mid x \mid \leq a \end{cases} \tag{5.23}$$

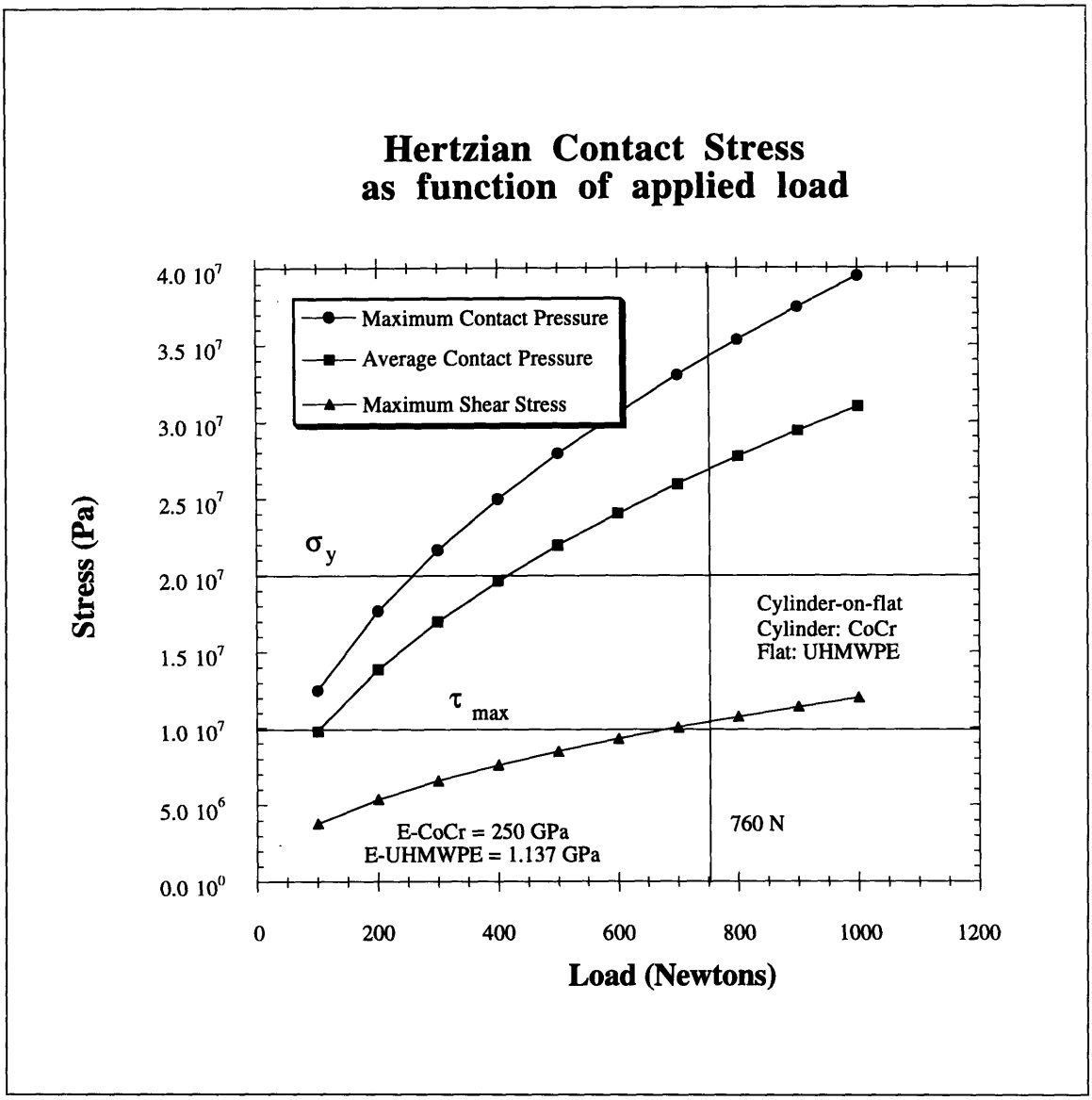

Figure 5-2: Maximum and average Hertz contact pressures, and maximum shear stress at a (depth of $z = 0.786P_{max}$) as functions of applied load

Integration of the general expressions for distributed loads yields:

$$\begin{aligned}
\sigma_x(x,z) &= \tfrac{q_o}{\pi}[(2x^2-2a^2-3z^2)\psi \\
&\quad +2\pi\tfrac{x}{a}+2(a^2-x^2-z^2)\tfrac{x}{a}\overline{\psi}] \\
&\quad -\tfrac{p_o}{\pi}z[(\tfrac{a^2+2x^2+2z^2}{a})\overline{\psi}-\tfrac{2}{a}-3x\psi] \\
\sigma_z(x,z) &= \tfrac{q_o}{\pi}z^2\psi-\tfrac{p_o}{\pi}z(a\overline{\psi}-x\psi) \\
\tau_{xz}(x,z) &= \tfrac{q_o}{\pi}[(a^2+2x^2+2z^2)\tfrac{z}{a}\overline{\psi} \\
&\quad -2\pi\tfrac{z}{a}-3xz\psi]-\tfrac{p_o}{\pi}z^2\psi
\end{aligned}$$

where

$$\begin{aligned}
\psi &= \tfrac{\pi}{k_1}\left\{\frac{1-\sqrt{\frac{k_2}{k_1}}}{\sqrt{\frac{k_2}{k_1}\left[2\sqrt{\frac{k_2}{k_1}}+\left(\frac{k_1+k_2-4a^2}{k_1}\right)\right]}}\right\} \\
\overline{\psi} &= \tfrac{\pi}{k_1}\left\{\frac{1+\sqrt{\frac{k_2}{k_1}}}{\sqrt{\frac{k_2}{k_1}\left[2\sqrt{\frac{k_2}{k_1}}+\left(\frac{k_1+k_2-4a^2}{k_1}\right)\right]}}\right\}
\end{aligned} \tag{5.24}$$

and

$$\begin{aligned}
k_1 &\equiv (a+x)^2+z^2 \\
k_1 &\equiv (a-x)^2+z^2
\end{aligned}$$

If P, and Q are the applied forces per unit length:

$$p_o = \tfrac{2P}{\pi a}, \quad q_o = \tfrac{2Q}{\pi a} \tag{5.25}$$

such that the coefficient of friction is:

$$\mu = \frac{q_o}{p_o} \tag{5.26}$$

the contact width a required in the above relations can be calculated from:

$$a = \sqrt{\frac{2P\Delta}{\pi}} \tag{5.27}$$

where:

$$\Delta = \left\{ \frac{2}{\left(\frac{1}{R_1} + \frac{1}{R_2}\right)} \right\} \left\{ \frac{1-\nu_1^2}{E_1} + \frac{1-\nu_2^2}{E_2} \right\} \tag{5.28}$$

let $R_1 \rightarrow \infty$ for a semi-infinite solid.

The formulas for σ_x, σ_z, and τ_{xz} in Equation 5.24 were used to generate nine curves of the maximum shear stress distribution in Figure 5-3. The maximum shear stress distribution was calculated for loads of 100 N, 760 N (load used in all friction and wear experiments), and 1000 N. Essentially this plot depicts how the maximum shear stress varies beneath a cylindrical slider as a function of the contact width (given by the ordinate axis). Also, as with Figure 5-2, the curves in Figure 5-3 were obtained for the friction and wear testing geometry of a CoCr cylinder applying a load to a flat surface of UHMWPE.

The general trend which is evident in Figure 5-3 is that as the load is increased, the contact width increases. Another trend evident in Figure 5-3 is the effect of friction. As the friction coefficient is increased from 0.05 to 0.2, the curves lose their symmetry about the centerline at $x = 0$. The friction force in this case causes the curves to stretch towards the left.

At a load of 760 N, the maximum shear stress τ_{max} of UHMWPE of 10 MPa (see horizontal line in Figure 5-3) is exceeded at a point 275 μm to the left and right of the centerline of the cylindrical slider. The maximum shear stress is not exceeded closer to the centerline because of the hydrostatic state of stress which exists directly beneath the slider.

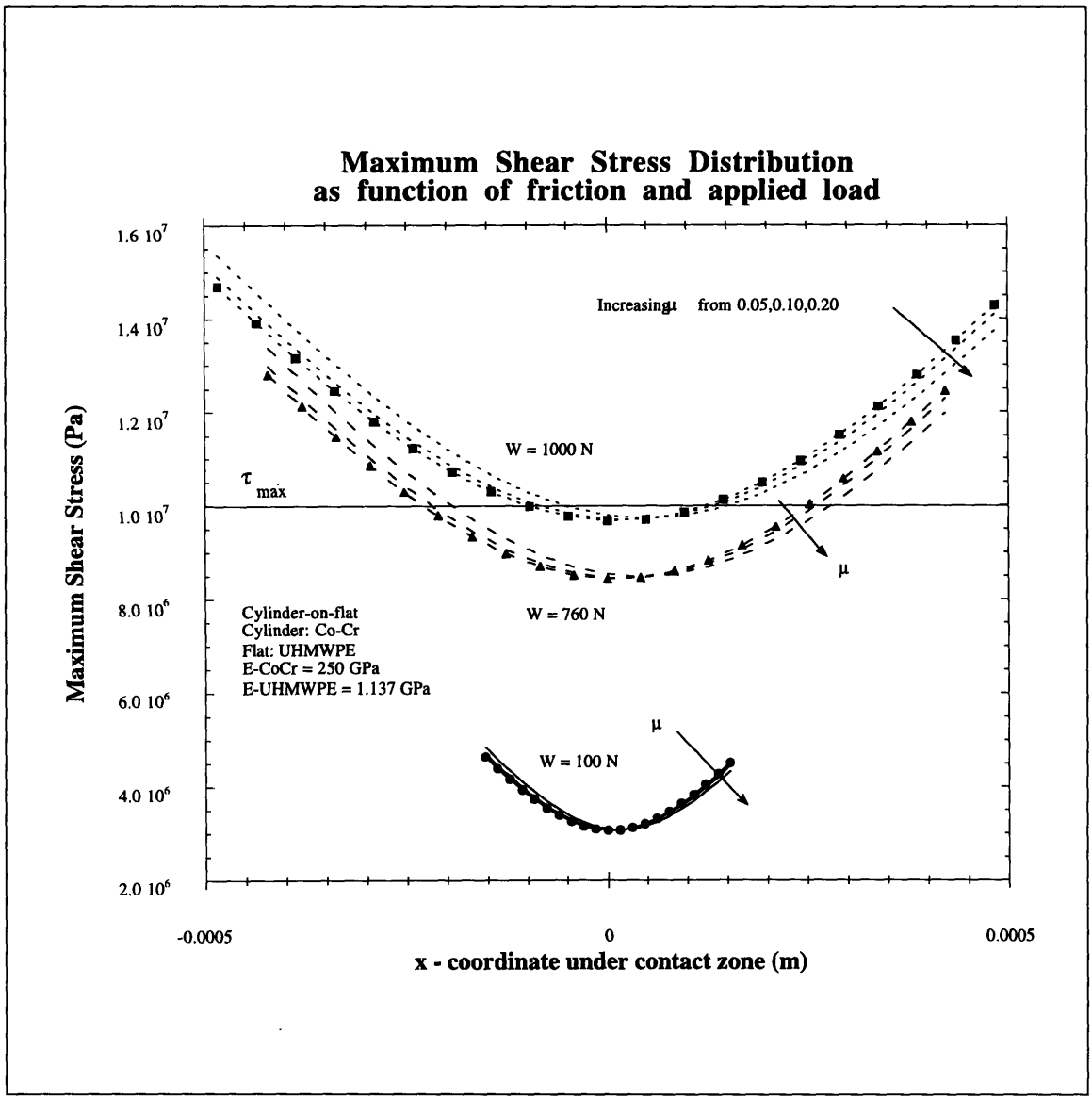

Figure 5-3: Maximum shear stress for varying friction coefficients and normal loads

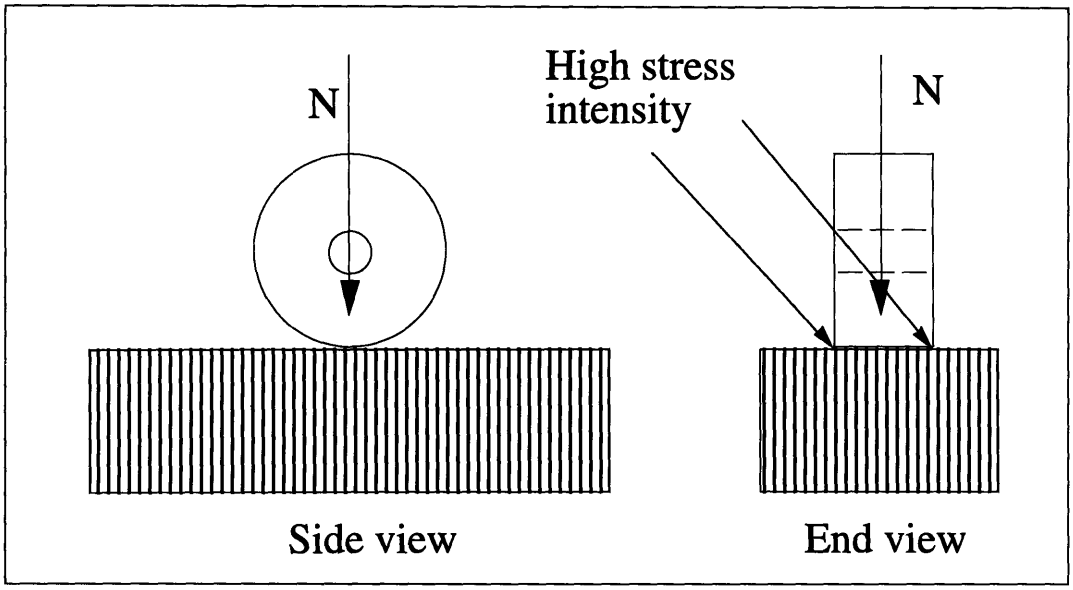

Figure 5-4: Edge effects occurring in the cylindrical slider

5.4 Edge effects in finite length cylinders

The linear theory of elasticity is only valid for small strains. Since the cylindrical indenter with square edges has a discontinuous profile a high stress concentration occurs at the edge. Linear elasticity theory yields infinite stress at this edge; since materials yield at a finite stress, elasticity theory only holds true for small strains.

Based on linear elasticity theory, the pressure distribution under a square indenter is:

$$p(x) = \frac{P}{\pi\sqrt{a^2 - x^2}} \tag{5.29}$$

These edge effects cannot be ignored because it is at these points that localized yielding occurs. This was observed in the ESEM micrographs and profilometry scans which showed large amounts of plowing and deformation at the edge of the wear tracks. This occurred despite the presence of a chamfer on the slider. Figure 5-4 shows two views of the slider and the location where the stress is concentrated at the edge of the slider.

This is a complex problem and cannot be solved using the previous relations for a 2D Hertzian contact cylinder-on-flat case. A three dimensional analysis of the edge effects is required to obtain the correct stress field beneath the slider. This problem has been examined by Ahamadi [1] and Lundberg [46]. Lundberg derived an expression for the pressure distribution acting over the rectangular area l x a on which the short cylinder sits, such that $l \gg a$.

$$p(x,y) = (\frac{P}{\pi a l})\sqrt{1-(x/a)^2} \tag{5.30}$$

where

$$a^2 = \frac{4PR}{\pi E^*} \tag{5.31}$$

At the very center he found that depth of the indentation is:

$$\delta(0,0) = \frac{P}{\pi l E^*}\{1.886 + \ln(l/a)\} \tag{5.32}$$

$$\Delta(y) \approx \frac{P}{2\pi l E^*} \ln\{1-(y/l)^2\} \tag{5.33}$$

However, at the ends this equation is not accurate and another equation valid at $y = \pm l$ should be used:

$$\Delta(y = \pm l) \approx \frac{P}{2\pi l E^*}\{1.193 + \ln(l/a)\} \tag{5.34}$$

These equations give the profile necessary to achieve a uniform pressure distribution given by p(x,y) so that at the very least, the stress singularity would not occur.

5.5 Modelling of Mechanical Behavior of Composites in Sliding Applications

5.5.1 Introduction

In many tribological applications of composites, the deformation of the surface under the action of the force of friction determines how well a composite material will perform with respect to wear and friction. The preceding section dealt with stresses due to a cylinder on flat. This Hertzian contact stress analysis is applicable to general isotropic materials; however, for viscoelastic and composite materials, such an analysis is not accurate.

To understand how a composite material will behave under frictional loading, it is important to know what the mechanical behavior of the composite surface will be. In cases which the composite consists of aligned fibers, the tensile and bending theories of fibers and laminates are suitable for yielding insight into the stresses and deformations which they undergo during sliding. However, the equations for bending and shearing of aligned fibers in a laminate are not the same as those for woven structures due to the more complicated geometry of fibers as found even in the common plain weave structure.

Although a great deal of experimental work has been done in the above areas of aligned fibers, relatively little work has been done in the modelling of textile composites in friction and wear applications. Researchers studying textile composites have focused on the behavior of single fabric laminates in attempting to characterize their mechanical properties [38, 72]. Tsukizoe, and Ohmae [81] have studied the frictional behavior of carbon, glass, stainless steel, and aramid fiber composites in many different sliding conditions. Friedrich [30] has proposed various models for the wear of composite materials and has specifically reviewed the use of the Rule of Mixtures approach in predicting the frictional behavior of a composite material.

The first section discusses a model for the friction coefficient μ in aligned-fiber composites proposed by Suh and Burgess [17]. The section which follows uses a similar approach; however, composite lamination theory is used to estimate μ for a woven textile composite [4].

5.5.2 Single Fiber Deformation Model

The following model for the calculation of the friction coefficient of a single carbon fiber was developed by Burgess [17]. By considering the work done on a single fiber, (i.e., the strain developed in the fiber due to the force of friction), the coefficient of friction may be determined. This is shown in equation 5.35. Figure 5-5 shows an idealized fiber subject to a normal and friction force. This model also considers the strain energy stored in the matrix of the composite U_M, and α the fraction of energy lost due to internal damping.

$$W_{diss} = F\delta \quad and \quad W_{diss} = \alpha U_M \tag{5.35}$$

Combining these two relations gives:

$$\mu = \frac{\alpha U_M}{N\delta} \tag{5.36}$$

Introducing the matrix volume V_M between two adjoining fibres shown in Figure 5-6 and integrating equation 5.37 yields equation 5.38:

$$U_M = \frac{1}{2} G_M \int_{V_M} \gamma^2 dV_M \tag{5.37}$$

$$U_M = \frac{G_M l r_f^3 \theta_d^2}{2c} \tag{5.38}$$

From the geometry in Figure 5-5, the following series of relations are obtained:

$$\begin{aligned} \delta &= R(1-\cos\theta_d) \\ l &= R\sin\theta_d + \lambda \\ l &= R\theta_d \\ \theta_d &= \sin\theta_d + \tfrac{\lambda}{R} \end{aligned} \tag{5.39}$$

Substituting equations 5.39 into equations 5.38 yields the friction coefficient:

$$\mu = \frac{\alpha}{N\delta}\left(\frac{G_M l r_f^3 \theta_d^2}{2c}\right) \tag{5.40}$$

The importance of this result is that it shows that a relation for the coefficient of friction may be derived beginning from the basic unit of a single fiber embedded in a matrix of known volume. This formula is quite adequate for a composite having aligned fibers. If the fibers are in a woven structure as is the case with the fabric-based homocomposite, then this relation does not hold true because of the effects of fibers in the perpendicular weave direction. However, using a similar approach based on the bending of a single fiber, the next section uses classical lamination theory to provide the necessary relations to calculate a friction coefficient for a woven structure.

5.5.3 Development of Cross-ply Model

This section presents the use of a $[0/90]_n$ layup as an approximation to a plain woven structure, and with Classical Lamination Theory (CLT) [35], a relation for the coefficient of friction is derived [4]. A numerical estimate of the coefficient of friction is calculated using CLT and compared to an estimate obtained by using the Rule of Mixtures [30].

The effect of friction on a single fiber in a ply oriented perpendicular to the frictional force is shown in Figure 5-7. By modelling the deformation of a fiber δ as a cantilever, the frictional force F can be determined if M and l_{fiber} are known. The length of the fiber can be experimentally determined; however,

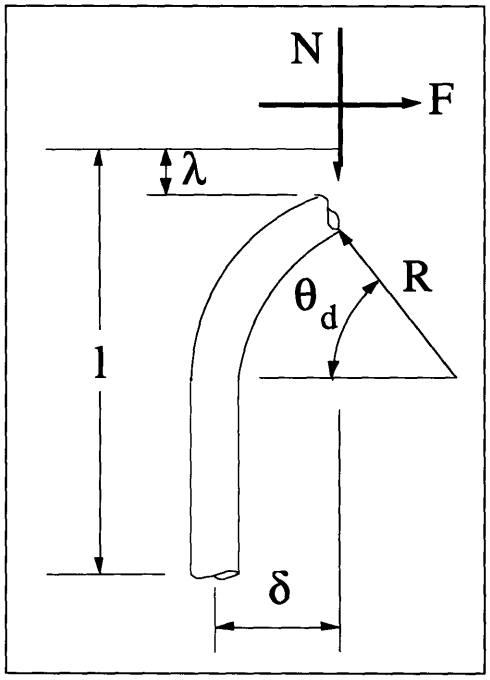

Figure 5-5: Model of deflected fiber used to determine μ [17]

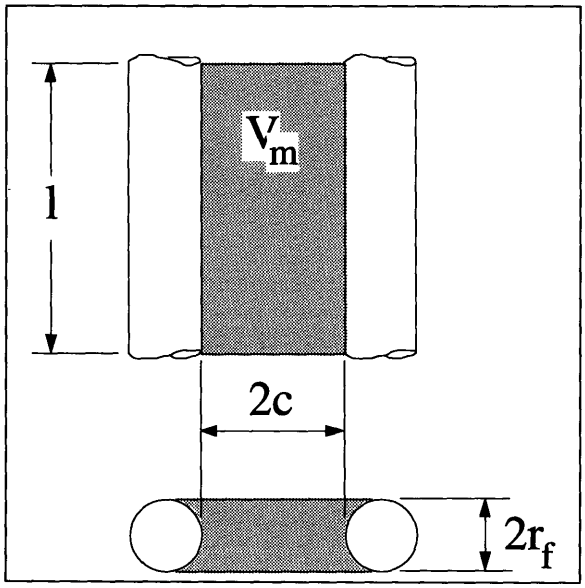

Figure 5-6: Matrix volume between two fibers undergoes deformation [17]

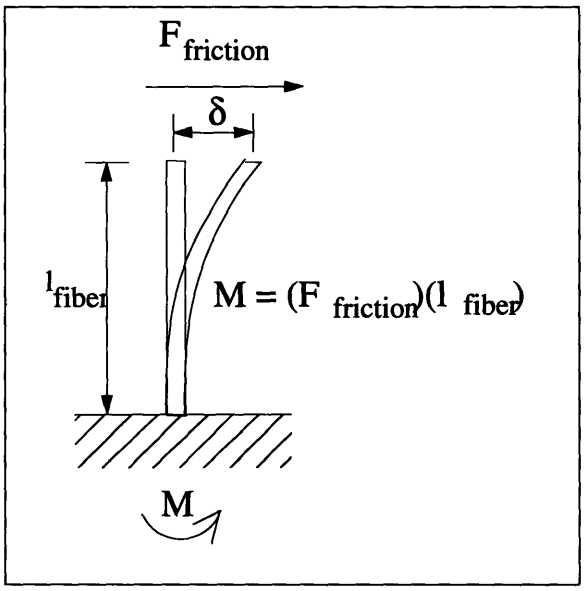

Figure 5-7: Model of single fiber bending as a cantilever

further analysis is necessary to find M. To find M, CLT is introduced. Since CLT considers only laminates comprising aligned fibers in a matrix, it was assumed that a $[0/90]_n$ layup could approximate a layup of plain woven fibers. This simplifying assumption is shown in Figure 5-8.

Such a layup is known as an antisymmetric layup because there are an even number of plies (n plies). Equations 5.41 and 5.42 are the resultant force and moment relations for this layup. The presence of B_{ij} terms in both of these equations means that there is coupling between the extensional stiffnesses A_{ij} and bending stiffnesses D_{ij}. To apply these equations a physical model is required. Such a model is shown in Figure 5-9 with a cylindrical indenter shown moving over a surface of normally oriented woven laminae. This is essentially the physical representation of a typical friction test discussed in Chapter 4.

$$\begin{Bmatrix} N_x \\ N_y \\ N_{xy} \end{Bmatrix} = \begin{bmatrix} A_{11} & A_{12} & 0 \\ A_{12} & A_{22} & 0 \\ 0 & 0 & A_{66} \end{bmatrix} \begin{Bmatrix} \epsilon_x^o \\ \epsilon_y^o \\ \epsilon_{xy}^o \end{Bmatrix} + \begin{bmatrix} B_{11} & 0 & 0 \\ 0 & -B_{11} & 0 \\ 0 & 0 & 0 \end{bmatrix} \begin{Bmatrix} \kappa_x^o \\ \kappa_y^o \\ \kappa_{xy}^o \end{Bmatrix} \tag{5.41}$$

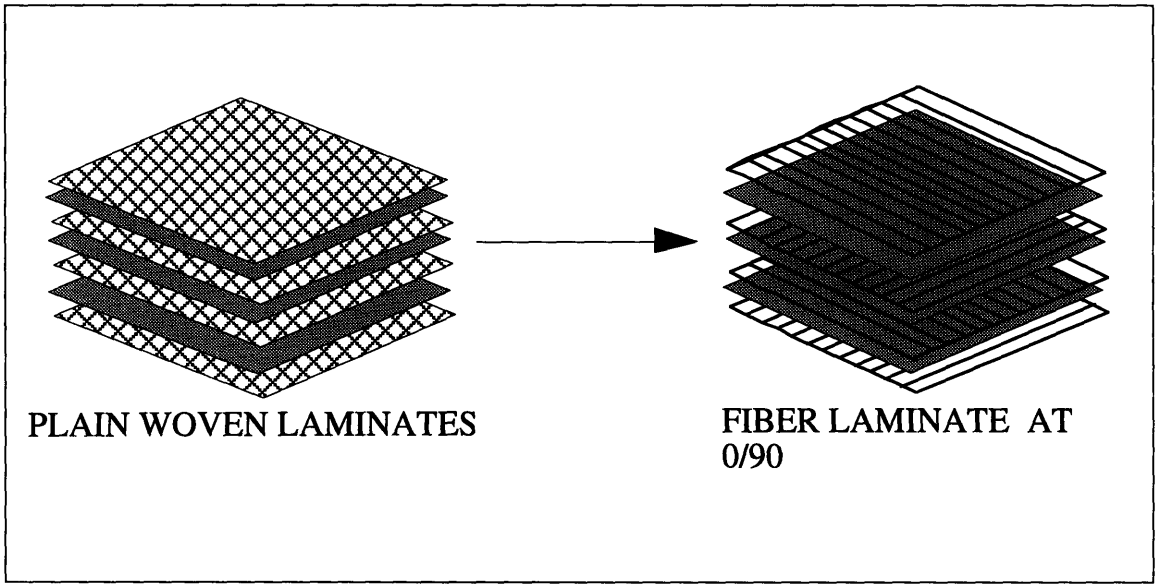

Figure 5-8: Approximation of a plain woven laminate by a fiber laminate

$$\begin{Bmatrix} M_x \\ M_y \\ M_{xy} \end{Bmatrix} = \begin{bmatrix} B_{11} & 0 & 0 \\ 0 & -B_{11} & 0 \\ 0 & 0 & 0 \end{bmatrix} \begin{Bmatrix} \epsilon_x^o \\ \epsilon_y^o \\ \epsilon_{xy}^o \end{Bmatrix} + \begin{bmatrix} D_{11} & D_{12} & 0 \\ D_{12} & D_{22} & 0 \\ 0 & 0 & D_{66} \end{bmatrix} \begin{Bmatrix} \kappa_x^o \\ \kappa_y^o \\ \kappa_{xy}^o \end{Bmatrix} \tag{5.42}$$

In this physical situation, $N_{xy} = N_y = 0$ and similarly $M_{xy} = M_y = 0$. With equations 5.41 and 5.42, the force resultant is the applied normal force N_x and the only moment resultant is M_x which is unknown.

Equations 5.41 and 5.42 must be inverted in order to calculate the strains which are necessary for this analysis. The set of equations resulting from this inversion is given by equation 5.43. The first equation from 5.43 is the only one of interest because it is the one that contains the unknown M_x.

$$\begin{Bmatrix} \epsilon_x \\ \epsilon_y \\ \epsilon_{xy} \end{Bmatrix} = [A'] \begin{Bmatrix} N_x \\ N_y \\ N_{xy} \end{Bmatrix} + [B'] \begin{Bmatrix} M_x \\ M_y \\ M_{xy} \end{Bmatrix} \tag{5.43}$$

Solving for M_x yields equation 5.44. In this equation N_x is the known applied

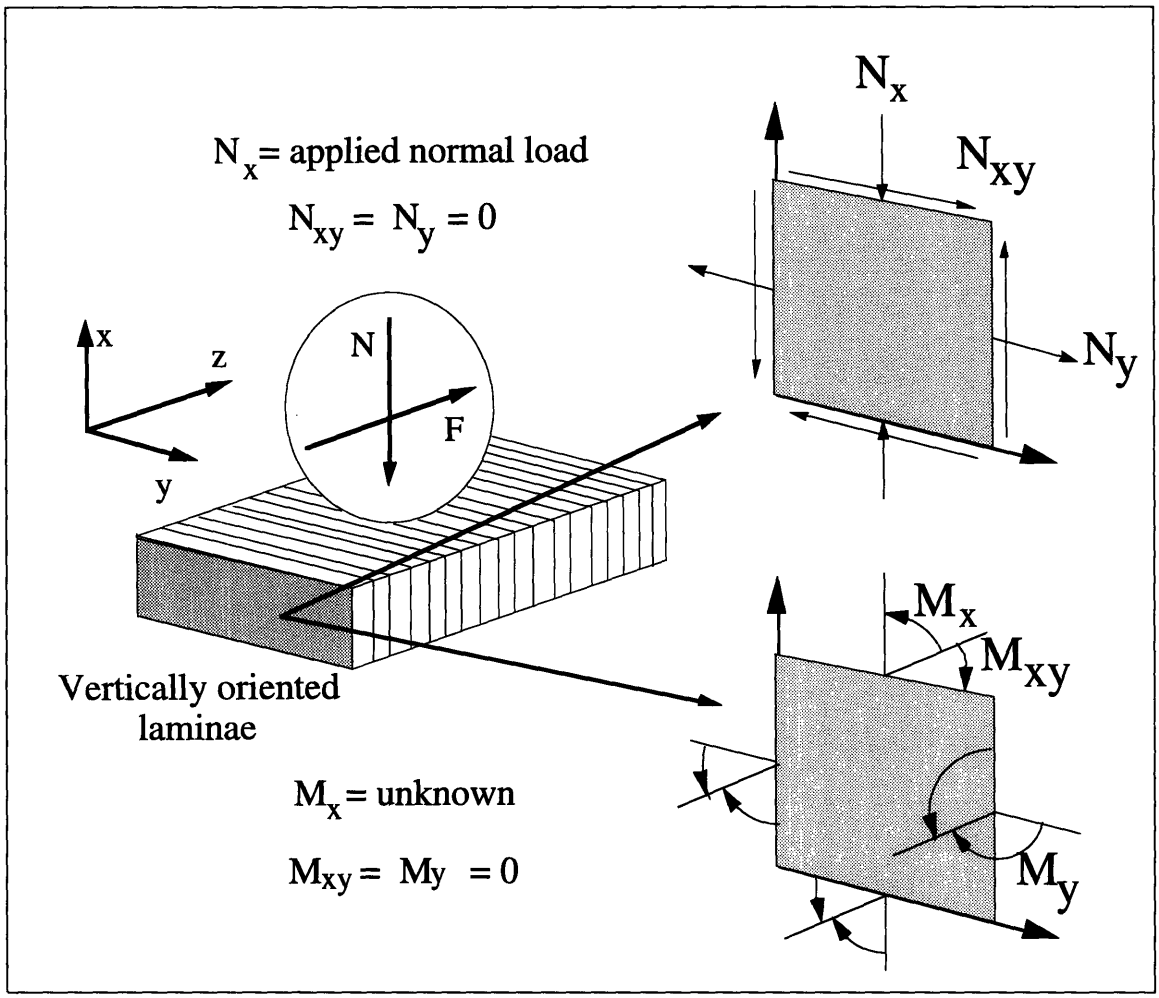

Figure 5-9: Physical modelling of forces applied by a cylindrical slider moving on top of vertically oriented laminae

normal load, and ϵ_x can be calculated from equation 5.45, where Δ is obtained by measuring the deformation in the x direction and L_{fiber} is the length of the fiber which is deformed. The deformation in the x direction can be experimentally determined using surface measurement techniques such as profilometry. Hertzian contact stress theory (Section 5.3.1) can be used to calculate the depth of deformation beneath a cylindrical contact load. For this analysis L_{fiber} was calculated to be approximately 500 μ m.

$$M_x = \frac{\epsilon_x - A'_{11} N_x}{B'_{11}} \tag{5.44}$$

$$\epsilon_x = \frac{\Delta}{L_{fiber}} \tag{5.45}$$

The only two values which remain to be found are A'_{11} and B'_{11}, these are numerically determined using the summation relations for N-layered laminates [35]. With all of the above quantities known, it is then possible to calculate the coefficient of friction as shown in equation 5.46.

$$\mu = \frac{F_{friction}}{N} = \frac{\left(\frac{M_x}{L_{fiber}}\right)}{N} = \frac{\left(\frac{\frac{\epsilon_x - A'_{11} N_x}{B'_{11}}}{L_{fiber}}\right)}{N} \tag{5.46}$$

Finally a method to predict the coefficient of friction which has received much attention in the literature [30, 81] uses the Rule of Mixtures approach frequently used in micromechanical analysis of laminae [35]. Equation 5.47 assumes that the friction and normal forces are carried by the fiber and matrix phases of the composite in proportion to the respective volume fraction of each phase. This assumption yields equation 5.48. To apply equation 5.48, the volume fraction must be known, and in addition, values of the friction coefficient of the fibers and matrix must be known independently.

$$\mu = \frac{F}{N} = \frac{F_f + F_m}{N_f + N_m} \tag{5.47}$$

$$\frac{1}{\mu} = V_f \frac{1}{\mu_f} + V_m \frac{1}{\mu_m} \tag{5.48}$$

Results

Friction coefficients were compared based on calculations using the Cross-ply Model, the Rule of Mixtures Model, and experimental data. This comparison is shown in Figure 5-10. The data obtained from the numerical simulation of the Cross-ply model was based on a plain woven textile composite (having the layup used in the homocomposite). The specific textile properties were those of UHMWPE Spectra 1000 with the properties listed in Table 3.4.3. This was compared to experimental μ values obtained from friction tests of a cylinder-on-flat (see Section 4.3). The sliding tests had an applied load of 760 N, a sliding distance of 14747.4 m, and bovine serum as the lubricant. The Rule of Mixtures Model was applied for values of $\mu_f = 0.05$ to $\mu_f = 0.15$ and $\mu_m = 0.15$.

The experimental data points curve exhibits a stronger dependence on the volume fraction than does the Rule of Mixtures three curves. The Cross-ply data was generated using a ply thickness of 250 μm and a laminate consisting of 20 plies. The single data point for the Cross-ply model friction coefficient is 0.11 which is lower than the experimentally obtained μ at a similar volume fraction. The reason for this may be due to the fact that the Cross-ply model doesn't account for distance slid nor the lubrication condition and as such may underestimate the coefficient of friction.

5.5.4 Discussion

In determining the accuracy and limitations of this Cross-ply model, the theory on which it is based should be considered. CLT assumes that a laminate consists of perfectly bonded laminae. Also, these bonds are assumed to be infinitesimally thin as well as non-shear- deformable. In the case of the woven fabric, bonds

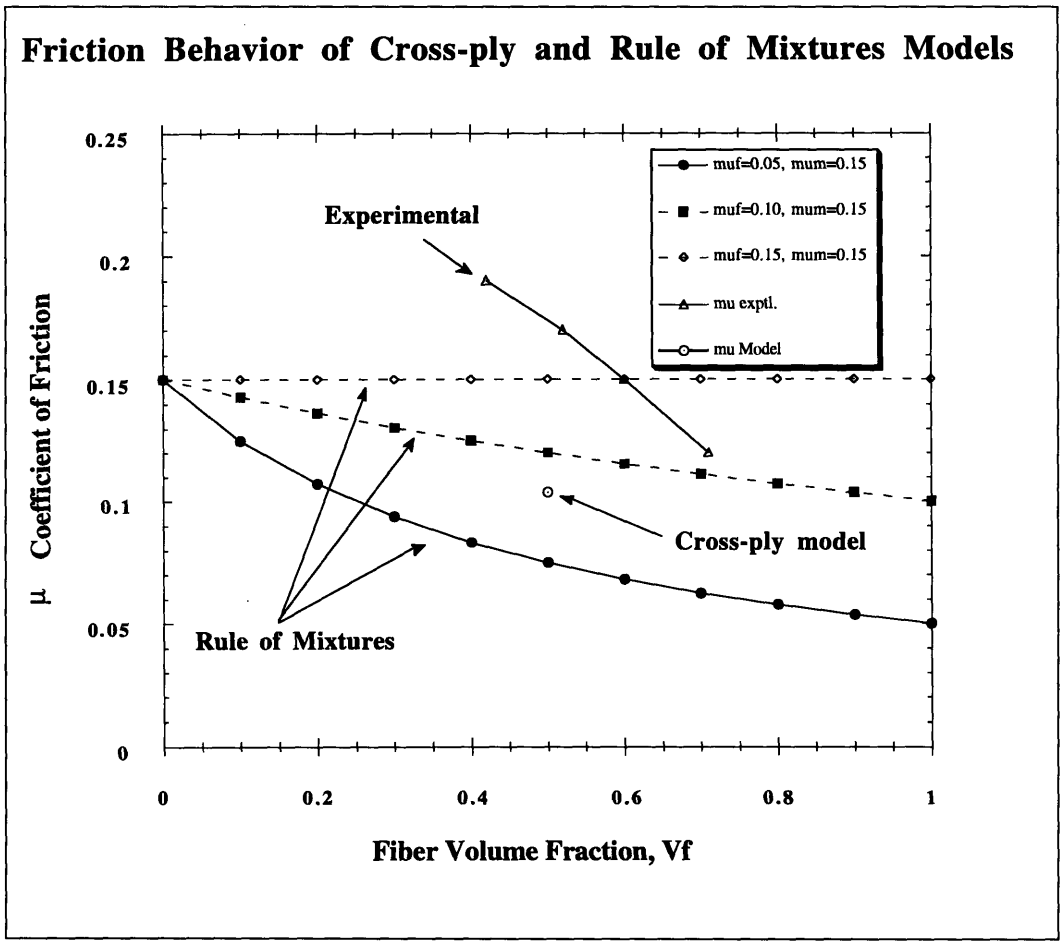

Figure 5-10: Comparison of theoretical results for various materials using the cross ply model to experimental data.

cannot be assumed to be perfect between the fabric and the matrix due to the voids caused by the woven structure. Also, the approximation of a woven laminate by a $[0/90]_n$ layup ignores the fiber interactions in the weave. The crimping effect which is known to occur in textiles under loading, affects the mechanical behavior of the weave and its ability to carry applied loads.

Another assumption made in the numerical simulation is the number of layers in the laminate. At any given moment, the slider only causes deformation in a localized area beneath it. This localized area is the contact area given by Hertzian contact stress theory. The width of this region was used as the thickness of the laminate in the calculations. In other words, as the distance from the centerline of the cylindrical slider increases, the effect of the friction force decreases asymptoically (as in the case of the stress field below a point load). Therefore, the number of layers considered should only equal the number which are present in the deformed zone beneath the slider. If N increases by more than 25 % of this value, the results begin to deviate significantly.

In summary, the Rule of Mixtures model for the friction coefficient was effective in giving a quick estimate of the μ; however, this method may only be used if the fiber and the matrix frictional properties are known independently. This method has limited use because of the added need to determine these properties experimentally.

Chapter 6

Conclusions and Future Recommendations

6.1 Summary

From the beginning, the goal of this research was to develop a material which could improve on existing commercially available UHMWPE used in artificial joints. Work began with ultra-tough high density polyethylene which exhibited improvement over unmodified high density polyethylene; however, when compared to UHMWPE still greater improvement was necessary. Nonetheless, the idea of reinforcing polyethylene with fibers was still valid and maintaining this concept led to experimentation with combinations of fiber/matrix UHMWPE and subsequently to the development of homocomposites. Once the idea had been transferred to UHMWPE, the benefits of the fiber reinforcement became immediately clear. One significant advantage is a low friction coefficient of 0.04 in bovine serum lubricated conditions, about one half of that of UHMWPE under the same conditions. Results were similar in tests with fiber-reinforced homocomposites and fabric-reinforced homocomposites.

6.2 Homocomposite Process Sensitivities

Despite progress with homocomposites, the manufacturing process of homocomposites is still to a certain extent influenced by manual processing. For example, the cutting of either fibers or fabrics is done manually; hence, there exists variability in fiber lengths and alignment. In addition, the process of fiber and matrix deposition has variability with respect to the uniformity of the fiber/matrix phases. This variability has manifested itself as debonding of the fiber matrix interface which has led to premature delamination and consequently higher friction and wear rates. This occurrence was discussed in Section 4.3.3. This variability can be minimized through careful control of the resin deposition rate and of the temperature during the molding cycle.

The final temperature in molding has been shown to be an extremely critical parameter in determining the overall strength of the fiber matrix bond. If the temperature is less than 150^oC, then poor bonding occurs and as a result the homocomposite can fail earlier than expected. Above the 160^oC threshold bonding is improved; however, the risk of degradation of the material increases. To minimize these effects of temperature fluctuations on quality, precise control of the temperature over the duration of the molding cycle is required. When this is achieved, the result is a reliable material which yields excellent friction and wear properties.

6.3 Friction and Wear Results

The data generated by friction and wear testing is ultimately the best indicator of the performance of the homocomposite and of UHMWPE. However, friction and wear data must be well analyzed in order to obtain insight into the performance of the material particularly with respect to the sliding history. The sliding history of all three materials tested showed some common trends. The most important of these is the need to test for a sufficient sliding distance in

order to achieve steady state conditions. In the case of the unirradiated samples of UHMWPE, it was not until a sliding distance of about 5000 m that the steady state friction coefficient was reached. Similar phenomena was observed for the irradiated UHMWPE. In some cases, debonding of the homocomposite occurred only after a specific number of cycles had elapsed. This varied according to molding conditions used and was discussed in Section 4.3.3.

In terms of wear data, similar precautions must be taken when analyzing data. With wear measurements performed using the weight loss method, the effect of water absorption can lead to significant errors. Without the use of the soak sample, some measurements actually give results indicating weight gain instead of loss. In particular, if fibers become exposed during wear testing as a result of debonding, then water absorption is significant. For this reason, tests should be of sufficiently long duration to ensure that weight loss clearly dominates over inaccuracy originating from water absorption. Sliding distances greater than 20000 m tends to give data which is relatively insensitive to this effect.

6.3.1 Recommendations for Friction and Wear Testing

Some important issues should be addressed in future friction and wear testing of homocomposites and UHMWPE. The first involves improving the nature of the debonding problem which can occur with homocomposites. In cases where processing conditions are correct, the resulting homocomposite can yield excellent friction and wear data. However, if fiber-matrix debonding occurs, then it would be useful to know the specific moment at which this occurs and correlate it with process parameters. This would be invaluable in improving the quality and performance of homocomposites.

The crack nucleation and growth problem should be investigated more closely. The ESEM results on worn UHMWPE surfaces showed evidence of surface cracks and tearing as a result of the high tensile stress behind the slider.

A study of the subsurface of both UHMWPE and homocomposites as a function of sliding distance could detect the nucleation and growth of these cracks. Such a study would require careful sectioning of the material beneath the wear track. Furthermore, prolonged tests (beyond 30000 m sliding distance) would be expected to generate the most information since greater cyclic plastic deformation would accumulate in the subsurface.

With regards to friction force measurement, the installation of two more friction measurement loadcells would be beneficial to increasing the confidence level of friction data. Currently only two loadcells of the four possible stations are instrumented. It has been observed that there is variance among the results between the four test stations. Care should be taken when making comparisons between test stations and calculating the standard deviation of experiments.

6.4 Overall Recommendations

The key to improving the performance of homocomposites is to improve the reliability of their manufacture. Automatic deposition of the fibers and matrix in a controlled manner would reduce variance in the fiber volume fraction. Also, the strength of the critical fiber-matrix bond which was emphasized in the previous section must be improved to eliminate debonding. This can be accomplished with better wetting of the fibers by the resin. Since polyethylene is non-polar, the wetting difficulty of Spectra fibers appears during molding. Allied Signal has found that plasma coating of fibers can increase their wettability. This is certainly an avenue that should be pursued in future research.

Throughout this research, compression molding has been the method used to manufacture homocomposites. However, the production of homocomposites using other composite manufacturing processes should be investigated. For example, pultrusion is a process which can give high production rates while still yielding high quality material. Furthermore this process can be varied

to give different volume fractions depending on the application in which the homocomposite is being used.

In more general terms, the applications of the homocomposite to biomedical applications has great societal benefits; however, its use should not be restricted solely to these applications. The use of UHMWPE as a bearing material is widespread in engineering applications, so other applications should be investigated. Finally, the concept of the homocomposite -a composite which is reinforced by fibers made of the same material as the matrix - has the potential to make a large impact in applications where there are tight constraints on the material combinations which can be used.

Bibliography

[1] N. Ahamadi, L.M. Keer, and T. Mura. Non-Hertzian contact stress analysis - normal and sliding contact. *International Journal of Solids and Structures*, 19:357, 1983.

[2] Philip E. Alei. Improvement of mechanical properties of polymers by molecular orientation. Master's thesis, Massachusetts Institute of Technology, 1983.

[3] J.M. Andrews and I.M. Ward. *Journal of Materials Science*, 5:411, 1970.

[4] J. Arinez. Composites 2.882 M.I.T. course assignment, 1995.

[5] J.R. Atkinson, D. Dowson, G.H. Isaac, and B.M. Wroblewski. Laboratory wear tests and clinical observatoins of the penetration of femoral heads into acetabular cups in total replacement hip joints I: A microscopical study of the surfaces of charnley polyethylene acetabular sockets. *Wear*, 104:217–224, 1985.

[6] ANSI/ASME B46.1-1985. Surface texture (surface roughness, waviness, and lay). Technical report, 1985.

[7] T.S. Barrett, G.W. Stachowiak, and A.W. Batchelor. Effect of roughness and sliding speed on the wear and friction of ultra-high molecular weight polyethylene. *Wear*, 153:331–350, 1992.

[8] Z. Bartczak and A.S. Argon R.E. Cohen. Deformation mechanisms and plastic resistance in single-crystal-textured high-density polyethylene. *Macromolecules*, 25(19):5036–5053, 1992.

[9] Z. Bartczak, R.E. Cohen, and A.S. Argon. Evolution of the crystalline texture of high-density polyethylene during uniaxial compression. *Macromolecules*, 25(18):4692–4704, 1992.

[10] A. Bellare, M. Spector, and R.E. Cohen. Quantitative characterization of the nanostructure of UHMWPE: a small angle x-ray scattering study. In *Annual meeting of the Society for Biomaterials*, 1995.

[11] E. Benz, B. Sherburne, J. Hayek, K. Falchuk, J.J. Godleski, C.B. Sledge, and M. Spector. Migration of polyethylene wear debris to lymph nodes and other organs in total joint replacement patients. In *20th annual meeting of the society for biomaterials*, April 1994.

[12] G.W. Blunn, P.S. Walker, A. Joshi, and K. Hardinge. The dominance of cyclic sliding in producing wear in total knee replacements. *Clinical Orthopaedics and Related Research*, (973):253–260, December 1991.

[13] L.L. Bohm. Ethylene polymerization process with a highly active Ziegler-Natta catalyst: 1. kinetics. In *Makromolekulares Kolloquim*, March 1977.

[14] L.L. Bohm. Ethylene polymerization process with a highly active Ziegler-Natta catalyst: 2. molecular weight regulation. In *Makromolekulares Kolloquim*, March 1977.

[15] L.L. Bohm. Reaction model for Ziegler-Natta polymerization processes. In *Makromolekulares Kolloquim*, March 1977.

[16] A.R. Bunsell. Fibre development for composite materials. *Fibre Reinforcements for Composite Materials*, 2:1, 1988.

[17] S. Burgess. Friction and wear of composites. Master's thesis, Massachusetts Institute of Technology, 1983.

[18] G. Capaccio and I.M. Ward. *Polymer Engineering Science*, 15:219, 1975.

[19] A.R. Champion, S. Li, K. Saum, E. Howard, and W. Simmons. The effect of crystallinity on the physical properties of UHMWPE. In *40th Annual Meeting of the Orthopaedic Research Society*, page 585, February 1994.

[20] P. Christel. The applications of carbon-fibre-reinforced-carbon composites (CFRC) in orthopaedic surgery. Technical report, Report from the Laboratoire de Recherches Orthopediques, U.A. CNRS 1161 ,10 avenue de Verdun, F - 75010 PARIS -France, 1993.

[21] J.R. Cooper, D. Dowson, and J. Fisher. Birefringent studies of polyethylene wear specimens and acetabular cups. *Wear*, 151:391–402, 1991.

[22] D.S. Cordova and A. Bhatnagar. High performance hybrid reinforced fiber composites-optimizing properties with polyethylene fibers. 1994.

[23] D.S. Cordova and D. S. Donnelly. Spectra extended chain polyethlene fibers. Technical report, 1994.

[24] D.J. Dijkstra, W. Hoogsteen, and A.J. Penning. Cross-linking of ultra-high molecular weight polyethylene in the melt by means of electron beam irradiation. *Polymer*, 30:866–873, May 1989.

[25] D. Doswon and R.T. Harding. The wear characteristics of ultra-high molecular weight polyethylene against a high density alumina ceramic under wet (distilled water) and dry conditions. *Wear*, 75:313–331, 1982.

[26] D. Dowson and N.C. Wallbridge. Laboratory wear tests and clinical observations of the penetration of femoral heads into acetabular cups in total replacement hip joints I: Charnley prostheses with polytetrafluoroethylene acetabular cups. *Wear*, 104:203–215, 1985.

[27] Allied fibers technical center. Ballistic systems with spectra composites. Technical report, 1994.

[28] J.R. Fleming and N.P. Suh. Mechanics of crack propagation in delamination wear. *Wear*, 44:39–56, 1977.

[29] J.R. Fleming and N.P. Suh. The relationship between crack propagation rates and wear rates. *Wear*, 44:57–64, 1977.

[30] Klaus Friedrich, editor. *Friction and wear of polymer composites.* Elsevier, 1986.

[31] A. Galeski, Z. Bartczak, and A.S. Argon R.E. Cohen. Morphological alterations during texture-producing plastic plane strain compression of high-density polyethylene. *Macromolecules*, 25(21):5705–5718, 1992.

[32] D.D. Huang and S. Li. Cyclic fatigue behaviors of UHMWPE and enhanced UHMWPE. In *38th Annual Meeting of the Orthopaedic Research Society*, page 403, February 1994.

[33] S. Jahanmir and N.P. Suh. Mechanics of subsurface void nucleation in delamination wear. *Wear*, 44:17–38, 1977.

[34] K.L. Johnson, editor. *Contact Mechanics*. Cambridge University Press, 1985.

[35] R.M. Jones. *Mechanics of composite materials*. McGraw-Hill Book Company, 1975.

[36] H.E. Kambic and A.T. Yokobori, editors. *Biomaterials' Mechanical Properties*. American Society for Testing and Materials, 1994.

[37] S.L. Kaplan, P.W. Rose, H.X. Nguyen, and H.W. Chang. Gas plasma treatment of spectra fiber. Technical report, 1994.

[38] S. Kawabata. Nonlinear mechanics of woven and knitted materials. *Textile Structural Composites*, 4:123, 1989.

[39] S.M. Kurtz, C.M. Rimnac, S. Li, and D.L Bartel. A bilinear material model for uhmwpe in total joint replacements. In *40th Annual Meeting of the Orthopaedic Research Society*, page 289, February 1994.

[40] M.M. Landy and P.S. Walker. Wear of ultra-high-molecular-weight polyethylene components of 90 retrieved knee prostheses. *UHMWPE Components in TKA*, pages S75–S85, 1993.

[41] S. Li. The identification of defects in ultra high molecular weight polyethylene. In *40th Annual Meeting of the Orthopaedic Research Society*, page 587, February 1994.

[42] S. Li and A.H. Burstein. Current concepts review ultra high molecular weight polyethylene. *The Journal of bone and joint surgery*, 76-A(7):1080–1089, July 1994.

[43] S. Li and E. G. Howard. Process of manufacturing ultra high molecular weight linear polyeythlene shaped articles, August 6 1991. Patent number 5,037,298.

[44] S. Li, E.V. Nagy, and B.A. Wood. In *38th Annual Meeting of the Orthopaedic Research Society*, page 41, February 1994.

[45] D.J. Ligterink. Calculation of wear (f.i. wear modulus) in the plastic cup of a hip joint prosthesis. *Wear*, 35:113–121, 1976.

[46] G. Lundberg and H. Sjovall. Stress and deformation in elastic solids. *Inst.Th. of Elasticity*, 4:66–99, 1958.

[47] K. Marcus, A. Ball, and C. Allen. On the nature of the transfer film at the interface of a water-lubricated sliding polymer-metal couple. *Journal of Applied Physics*, 25:A57–A64, 1992.

[48] MIT Radiation Protection Office. *Gammacell-220 Training Program.*

[49] J.G. Morley. *High-performance fibre composites.* Academic Press Limited, 1987.

[50] E.V. Nagy and S. Li. Analysis of retrieved knee componenets via fourier transform infrared spectroscopy. In *16th Annual Meeting of the Society for Biomaterials*, page 274, May 1990.

[51] E.V. Nagy and S. Li. A fourier transform infrared technique for the evaluation of polyethylene orthopaedic bearing materials. In *16th Annual Meeting of the Society for Biomaterials*, page 109, May 1990.

[52] H.J. Nusbaum, R.M. Rose, I.L. Paul, A.M. Crugnola, and E.L. Radin. Wear mechanisms for ultrahigh molecular weight polyethylene in the total hip prosthesis. *Journal of Applied Polymer Science*, 23:777–789, 1979.

[53] N.J. Pagano, editor. *Interlaminar response of composite materials.* Elsevier, 1989.

[54] J.P. Penning, H. van der Werff, M. Roukema, and A.J. Pennings. On the theoretical strength of gelspun/hotdrawn ultra-high molecular weight polyethylene fibres. *Polymer Bulletin*, 23:347–352, 1990.

[55] A.J. Pennings and M. Roukema. Further studies on the high-speed gel-spinning of ultra-high molecular weight polyethylene. *Polymer Bulletin*, 23:353–359, 1990.

[56] S.H. Rhee and J.H. Dumbleton. The application of the zero wear model to joint prostheses. *Wear*, 36:207–224, 1976.

[57] C. Rimnac, R. Klein, A. Burstein, T. Wright, and T. Santner. In vitro chemical and mechanical degradation of uhmpwe: one year results. In *40th Annual Meeting of the Orthopaedic Research Society*, page 175, February 1994.

[58] C.M. Rimnac, R.W. Klein, F. Betts, and T. Wright. Post-irradiation aging of ultra-high molecular weight polyethylene. *The Journal of Bone and Joint Surgery*, 76-A(7):1052–1056, July 1994.

[59] R.M. Rose, A.M. Crugnola, M. Ries W.R. Cimino, I.L. Paul, and E.L. Radin. On the origins of high in vivo wear rates in polyethylene components of total joint postheses. *Clinical orthopaedics and related research*, (145):277–286, Nov.-Dec. 1979.

[60] V. Saikko. Wear and friction properties of prosthetic joint materials evaluated on a reciprocating pin-on-flat apparatus. *Wear*, 166:169–178, 1993.

[61] J. Song and G.W. Ehrenstein. Friction and wear of self-reinforced thermoplastics. *Advances in Composite Tribology*, 8:19–61, 1993.

[62] G.W. Stachowiak and A.W. Batchelor. *Engineering Tribology.* Elsevier, 1993.

[63] R.M. Streicher. The behavior of uhmwpe when subjected to sterilization by ionizing radiation. 66-73.

[64] R.M. Streicher. Uhmw polyethylene used as a material for the articulating components of endoprostheses. *Biomed. Technik*, 38(12):303–313.

[65] R.M. Streicher. Ultra-high-molecular polyethylene as material for hip-joint cups. In *8th Munich Symposium for Experimental Orthopaedics*, 1986. Alloplastic replacement of the hip socket.

[66] R.M. Streicher. Influence of ionizing irradiation in air and nitrogen for sterilization of surgical grade polyethylene for implants. *Radiation Physics Chemistry*, 31(4-6):693–698, 1988.

[67] R.M. Streicher. Investigation on sterilization and modification of high molecular weight polyethylenes by ionizing irradiation. *Beta-gamma*, (1):34–43, 1989.

[68] R.M. Streicher. Improving UHMWPE by ionizing irradiation crosslinking during sterilization. In *17 Annual meeting of the Society for Biomaterials*, May 1991.

[69] R.M. Streicher, R. Schoen, and M.F. Semlitsch. Tribology and possibilities for optimizing the wear properties of metal-on-polyethylene combinations for artificial joints. Technical report, Sulzermedica, 1994.

[70] R.M. Streicher and R. Schon. Examinations of explanted hip joint cups made from uhmwpe. Technical report, Sulzermedica, 1994. 196-201.

[71] R.M. Streicher, M. Semlitsch, and R. Schon. Ceramic surfaces as wear partners for polyethylene. *Bioceramics*, 4, 1991. Proceedings of the 4th international symposium on ceramics in medicine.

[72] N. Stubbs. Elastic and inelastic response of coated fabrics to arbitrary loading paths. *Textile Structural Composites*, 4:263, 1989.

[73] N.P. Suh. An overview of the delamination theory of wear. *Wear*, 44:1–16, 1977.

[74] N.P. Suh. *Tribophysics.* Prentice-Hall Inc., 1986.

[75] N.P. Suh and P.E. Alei. Ultra tough plastic material, 1983. U.S. patent 4600631.

[76] N. Sung and N.P. Suh. Effect of fiber orientation on friction and wear of fiber reinforced polymeric composites. *Wear*, 53:129–141, 1979.

[77] T.Y. Tam, M.B. Boone, and G.C. Weedon. New horizons in advanced oriented fiber. *Polymer Engineering and Science*, 28(13):871–874, JULY 1988.

[78] S.P. Timoshenko and J.N. Goodier. *Theory of elasticity.* McGraw-Hill Book Company, 1987.

[79] P.S. Trent and P.S. Walker. Wear and conformity in total knee replacement. *Wear*, 36:175–187, 1976.

[80] P.S. Trent and P.S. Walker. The wear behavior of ultrahigh molecular weight polyethylene. *Wear*, 37:279–289, 1976.

[81] T. Tsukizoe and N. Ohmae. Friction and wear performance of unidirectionally oriented glass, carbon, aramid and stainless steel fiber-reinforced plastics. *Friction and Wear of Polymer Composites*, 1:157, 1986.

[82] X. Wang, S. Li, and R. Salovey. Processing of ultrahigh molecular weight. *Journal of Applied Polymer Science*, 35:2165–2171, 1988.

[83] T.M. Wright and D.L. Bartel. The problem of surface damage in polyethylene total knee components. *Clinical Orthopaedics and Related Research*, (205):67–74, April 1986.

[84] M. Yasuniwa and C. Nakafuku. High pressure crystallization of ultra-high molecular weight polyethylene. *Polymer Journal*, 19(7):805–813, 1987.

[85] M. Yasuniwa, M. Yamaguchi, A. Nakamura, and S. Tsubakihara. Melting and crystallization of solution crystallized ultra-high molecular weight polyethylene under high pressure. *Polymer Journal*, 22(5):411–415, 1990.

Appendix A

Measurement of Surface Topography

The American National Standards Institute clearly defines many surface features in a Standard called Surface Texture (Surface Roughness, Waviness, and Lay) [6]. This standard [6] sets out some basic definitions:

- *Surface:* The surface of an object is the boundary that separates that object from another object, substance, or space.
- *Surface Texture:* is the repetitive or random deviation from the nominal surface that forms the three-dimensional topography of the surface.
- *Roughness:* Roughness consists of the finer irregularities of the surface texture, usually including those irregularities that result from the inherent actions of the production process.
- *Waviness:* Waviness is the more widely spaced component of surface texture. Waviness includes all irregularities whose spacing is greater than the roughness sampling length and less than the waviness sampling length.

A.1 Surface Parameters

According to the Standard [6], the average surface roughness R_a is:

$$R_a = \frac{1}{L}\int_{x=0}^{x=L} \mid y \mid dx \tag{A.1}$$

where:

R_a = arithmetic average deviation from center line

L = sampling length

y = ordinate of the curve of the profile

This integration can be approximated in the following manner:

$$R_a \approx \frac{y_1 + y_2 + y_3 + \cdots + y_N}{N} \tag{A.2}$$

The Standard [6] also defines the root-mean-square surface roughness R_q as:

$$R_q = \sqrt{\frac{1}{L}\int_{x=0}^{x=L} y^2 dx} \tag{A.3}$$

R_q = root-mean-square deviation from the centerline

Similar to the R_a, the above integration can be approximated with the following relation:

$$R_q \approx \sqrt{\frac{y_1^2 + y_2^2 + y_3^2 + \cdots + y_N^2}{N}} \tag{A.4}$$

See Figure A-1 for a typical surface profile trace used to calculate the above expressions.

A.2 Effect of Cutoff Wavelength

With all surface profiling and measuring systems signal cutoff-filter frequencies must be selected and used to obtain meaningful roughness measurements. The ANSI standard [6] defines the cutoff as the electrical response characteristic of the roughness measuring instrument which is selected to limit the spacing of the surface irregularities to be included in the assessment of roughness average. Related to this is the Roughness Sampling Length [6] which is the sampling length within which the roughness average is determined and helps to distinguish roughness profile irregularities from waviness profile irregularities. The ANSI standard recommends that the roughness sampling length or cutoff should be about 5-40 times the maximum irregularity spacing. Depending on the spacing of roughness irregularities, choosing a low cutoff can yield a low calculation of the R_a value. For this reason care must be taken in specification of the cutoff wavelength. The manufacturer of the Dektak 8000 recommends that a cutoff wavelength be selected on the basis of the following range:

$$(8x ScanResolution) \leq Cutoff\ Wavelength \leq \frac{ScanLength}{5} \tag{A.5}$$

With the Dektak 8000, two types of filters may be enabled. A short (high) pass filter filters out low frequency waviness signals, allowing high frequency roughness data to be analyzed. The second filter, a long (low) pass filter filters out high frequency roughness signals, thus permitting low frequency waviness data to be processed. Since in this work waviness data was not considered, only the short pass filter was activated. The short pass filter of 0.25 mm (traversing length 5-15 mm) and 0.8 mm (for traversing lengths of 15-50 mm) were selected in accordance with the ANSI/ASME B46.1-1985 standard [6].

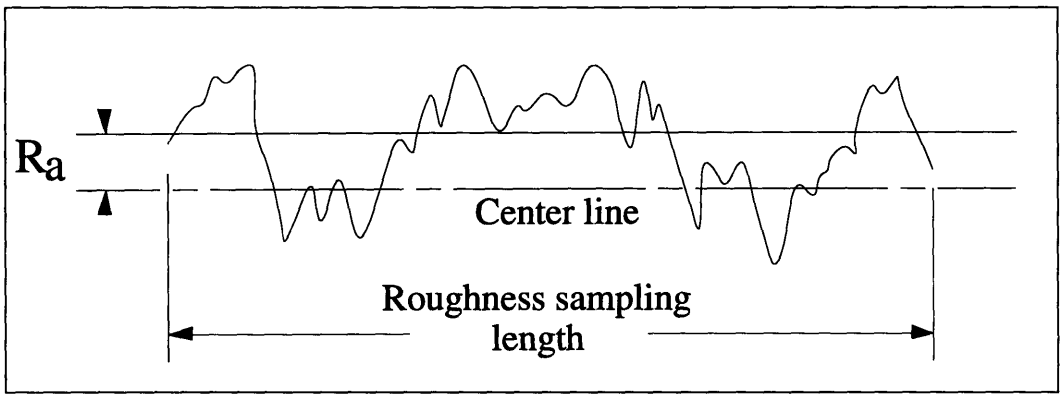

Figure A-1: A surface profile for calculation of the roughness values R_a and R_q [6]

Appendix B

Gamma Irradiation

B.1 Irradiation Source

Wear test samples were exposed to gamma irradiation using the M.I.T. Gammacell-220 [48] which uses $^{60}Cobalt$ as a source. $^{60}Cobalt$ has a half-life of 5.271 years with a decay process shown in Figure B-1. The process involves $^{60}Cobalt$ emitting gamma rays and decaying to stable $^{60}Nickel$. Two gamma rays are emitted releasing energies of 1.1732 MeV and 1.3325 MeV which yields a total of 2.5057 MeV.

B.2 Dosage Rates

The dosage rate at any specific moment in time may be calculated using the following exponential decay formula:

$$D_{(t)} = D_{(o)}(e^{-\lambda t}) \tag{B.1}$$

where:

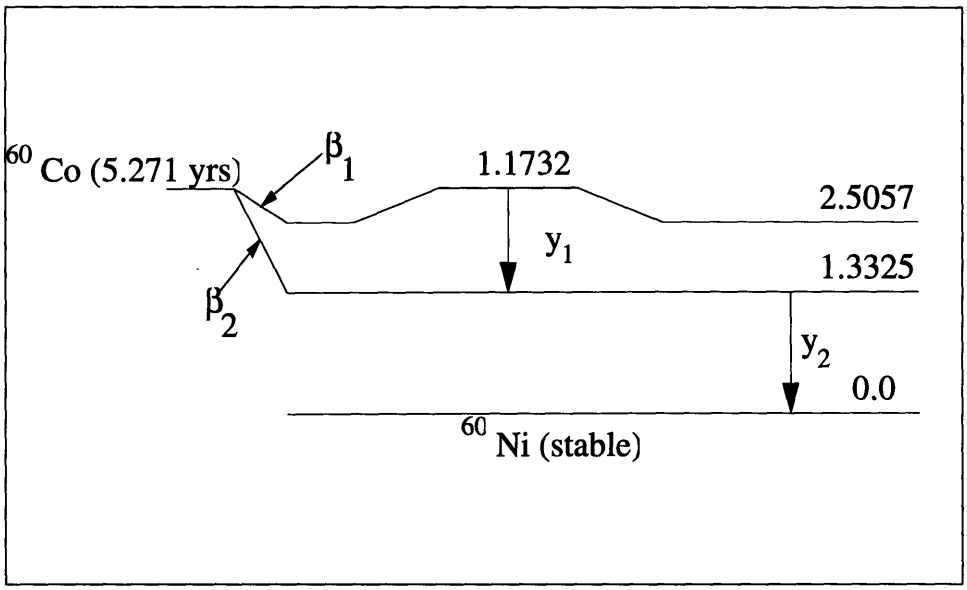

Figure B-1: Decay of $^{60}Cobalt$ [48]

$D_{(t)}$ = *Dose rate at desired time t*

$D_{(o)}$ = *Initial dose rate*

λ = *Decay constant* = $0.1315\,yr^{-1}$

t = *time interval (in years)*

The dose rate in the chamber on 2/1/93 was 640 Rads/min.

B.3 Shielding

Some irradiation was done in vacuum using a stainless steel chamber. For this reason it was necessary to correct the equations used to calculate the dosage levels for the shielding effects of the stainless steel chamber. The formula used to calculate the shielding effectiveness of any material is:

$$D_{(s)} = D_{(\mu)}(e^{-\mu X})B \tag{B.2}$$

where:

$D_{(s)}$ = *Shielded dose rate at desired point*

$D_{(\mu)}$ = *Initial dose rate*

μ = *Linear attenuation coefficient for* 2.5 MeV *gamma ray in stainless steel* 304

X = *Shield thickness* = 0.033 cm

B = *Buildup factor, accounts for secondary scattered radiation produced in the shield* = 10.5

Appendix C

Loadcell Calibration

This appendix contains the data used to calibrate the wear tester loadcells. In Section 4.2.2 and in Figure 4-4 the principle of the operation of the loadcell was discussed. In this section the coupling of the friction and normal loads was addressed. This appendix contains the specific calibration data which determines the extent of coupling which occurs. Calibration was performed on each of the two loadcells. The data presented here is for loadcell #1; however, the results for loadcell #2 are very similar. Two calibration tests were performed. One test consisted of determining the voltage-force relationship for the normal load strain guages. The second test performed determined the voltage-force relationship for the friction force strain guages. To test the sensitivity of both channels to variations in the other applied force, various loads were applied. Increasing normal loads of 10 to 230 lbs. and tangential loads of 10, 20, and 30 lbs. were applied to the loadcell in the manner depicted in Figure C-1.

Figure C-2 is of the calibration of the normal load strain guages. This figure shows output voltage as a function of increasing normal load while simultaneous friction loads of 0, 10, 20, and 30 lbs. are applied. The calibration of the friction force strain guage is shown in Figure C-3. It shows the output voltage as a function of increasing tangential load from 0 to 115 lbs. while simultaneous

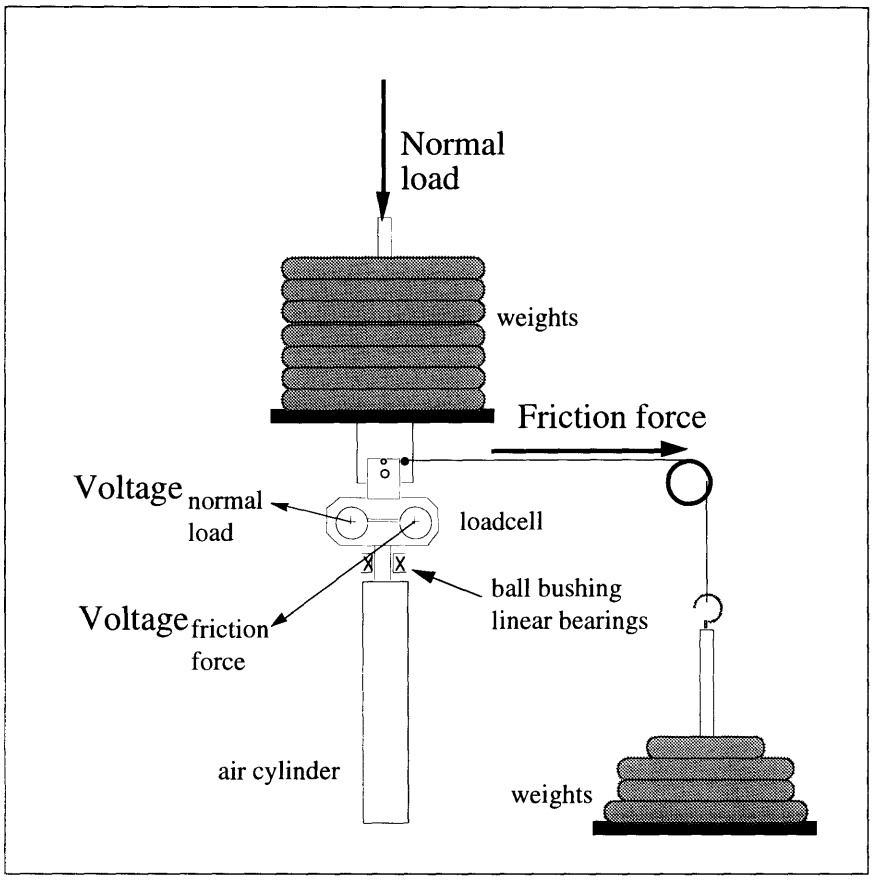

Figure C-1: Use of weights to calibrate loadcell strain guages by simultaneously applying a normal and frictional force.

normal loads of 175, 180, 185, and 190 lbs are applied.

In both Figure C-2 and Figure C-3 the relation between voltage and applied load is essentially linear; therefore, a linear fit of the data was performed. Table C.2 and Table C.1 show the linearized slopes of the voltage-force relationships (and the corresponding standard deviations) which were programmed into the data acquistion system used to collect the coefficient of friction.

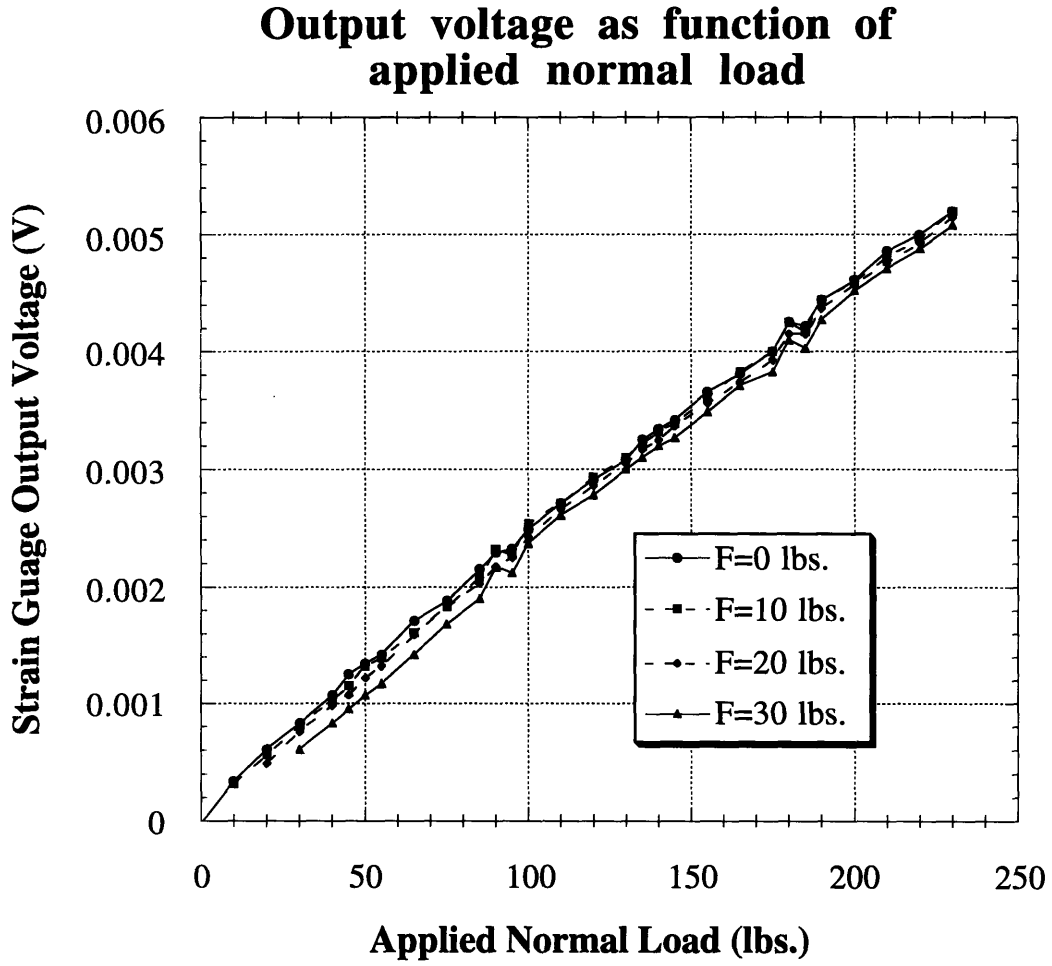

Figure C-2: Output voltage plotted as a function of applied normal load with a simultaneously applied frictional load.

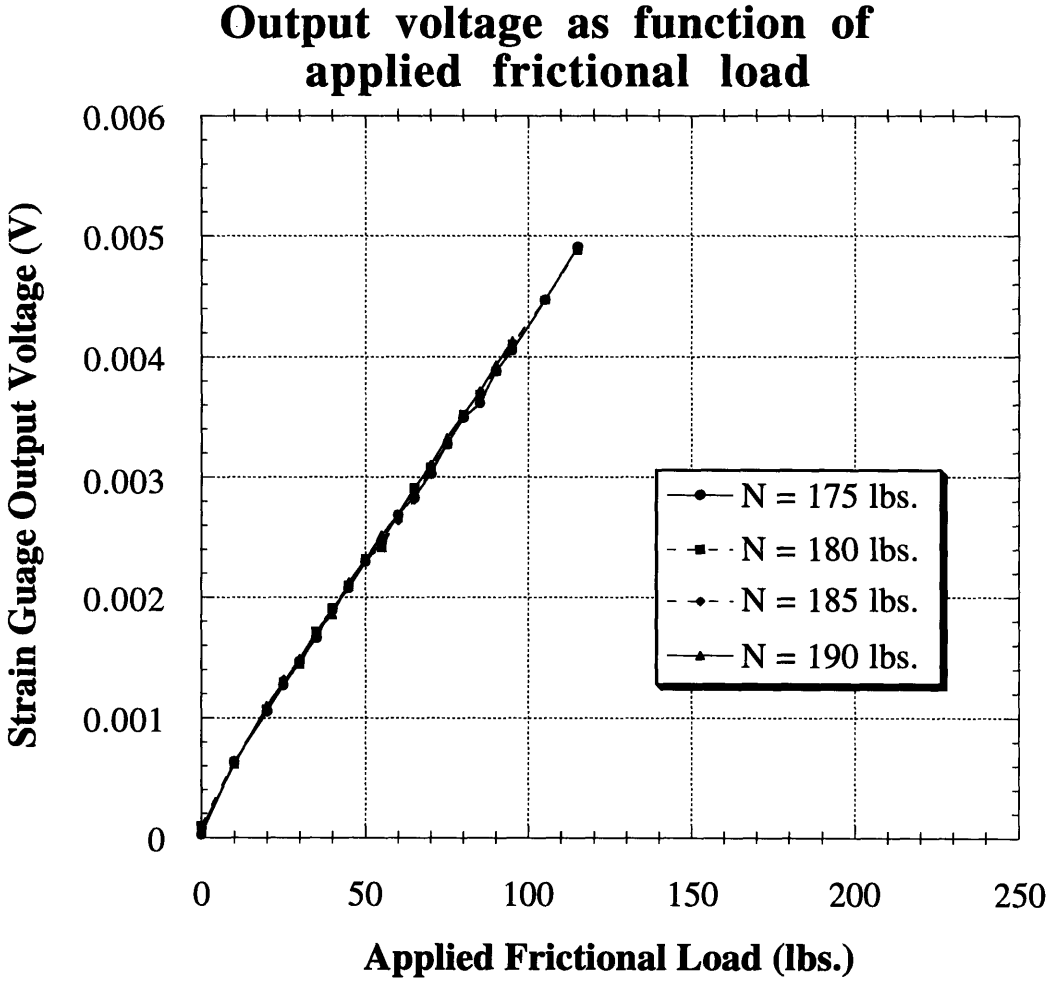

Figure C-3: Output voltage plotted as a function of applied frictional load with a simultaneously applied normal load.

Normal Load	Slope	Intercept
175 lbs.	$4.08x10^{-5}$	0.000207
180 lbs.	$4.10x10^{-5}$	0.000222
185 lbs.	$4.08x10^{-5}$	0.000217
190 lbs.	$4.15x10^{-5}$	0.000212
Average	$4.10x10^{-5}$	0.000215
Standard Deviation	$3.15x10^{-7}$	$6.40x10^{-6}$

Table C.1: Linearization of voltage as a function of applied normal load

Frictional load	Slope	Intercept
0 lbs.	$2.22x10^{-5}$	0.000197
10 lbs.	$2.21x10^{-5}$	0.000191
20 lbs.	$2.21x10^{-5}$	0.000138
30 lbs.	$2.24x10^{-5}$	0.000005
Average	$2.22x10^{-5}$	0.000133
Standard Deviation	$1.67x10^{-7}$	$8.93x10^{-5}$

Table C.2: Linearization of voltage as a function of applied frictional force